Inaugural dissertation

for

obtaining the doctoral degree

of the

Combined Faculty of Mathematics, Engineering and Natural Sciences

of the

Ruprecht - Karls - University

Heidelberg

Presented by

M.Sc. Đorđe Salai

born in: Belgrade, Serbia

Oral examination: 05.12.2024

Super-resolution microscopy of HIV-1 Gag assembly-induced lipid domains

Referees: Prof. Dr. Hans-Georg Kräusslich

Prof. Dr. Britta Brügger

Table of Contents

I. Abbreviations

AIDS	Acquired immunodeficiency syndrome
ALIX	AGL 2-interacting protein
AP-2	Clathrin adaptor protein 2 complex
APOBEC3G	Apolipoprotein B mRNA editing enzyme, subunit 3G
ART	Antiretroviral therapy
CA	Capsid domain of Gag
CCR5	C-C Chemokine receptor type 5
CD4	Cluster of differentiation 4
cDNA	Complementary DNA
Cer	Ceramide
CPSF6	Cleavage and polyadenylation specificity factor subunit 6
CT	Cytoplasmic tail of gp41
CTxB	Cholera toxin subunit B
CXCR4	C-X-C Chemokine receptor type 4
D4	Domain 4 of perfringolysin O
DENV	Dengue virus
DMEM	Dulbecco's modified eagle medium
DNA	Deoxyribonucleic acid
DRM	Detergent resistant membrane
dsDNA	Double-stranded DNA
EBOV	Ebola virus
EM	Electron microscopy
EqtII	Equinatoxin II
ER	Endoplasmic reticulum
ERC	Endosomal recycling compartment
ESCRT	Endosomal sorting complex required for transport
ET	Electron tomography
FIP1C	Rab 11 family-interacting protein 1 C
GalCer	Galactosylceramide
GlcCer	Glucosylceramide
GM1	Monosialotetrahexosylganglioside
GPI	Glycosylphosphatidylinositol
GPMV	Giant plasma membrane derived vesicle
GSL	Glycosphingolipid
GUV	Giant unilamellar vesicle
HA	Hemagglutinin A
HAART	Highly active antiretroviral therapy
HBR	Highly basic region of MA
HCV	Hepatitis C virus
hDlg1	Human discs large protein 1
HexCer	Hexosylceramide
HIV-1	Human immunodeficiency virus type 1

HSV-1	Herpes simplex virus 1
HTLV-III	Human T-lymphotropic virus type 3
IAV	Influenza A virus
ICTV	International committee for taxonomy of viruses
IF	Immunofluorescence
IN	Integrase
INSTIs	IN strand transfer inhibitors
IP3	Inositol-1,4,5-triphosphate
IP6	Inositol hexakisphosphate
KSHV	Kaposi sarcoma associated herpes virus
LAV	Lymphadenopathy associated virus
Ld	Liquid disordered phase
Lo	Liquid ordered phase
LTR	Long terminal repeat
Lys	Lysenin
MA	Matrix domain of Gag
MDM	Monocyte derived macrophage
mEGFP	Monomeric enhanced green fluorescent protein
MHC	Major histocompatibility complex
mRNA	Messenger RNA
MS	Mass spectroscopy
MSI	Mass-spectrometry imaging
MβCD	Methyl-β-cyclodextrin
NC	Nucleocapsid domain of Gag
NFkB	Nuclear factor kappa B
NNRTIs	Non-nucleoside RT inhibitors
NPC	Nuclear pore complex
NRTIs	Nucleoside RT inhibitors
NT-Lys	Nontoxic Lysenin truncation
Pac-Cholesterol	Photo-activated Cholesterol
PALM	Photoactivated localization microscopy
PBS	Phosphate buffered saline
PC	Phosphatidyl choline
PE	Phosphatidyl ethanolamine
PFA	Paraformaldehyde
PFO	Perfringolysin O
PG	Phosphatidylglycerol
PI	Phosphatidylinositol
PIC	Preintegration complex
PIP2	Phosphatidylinositol-(4.5)-bisphosphate
PIs	PR inhibitors
PLL	Poly-L-lysine
pl-PE	Plasmalogen phosphatidylethanolamine
PM	Plasma membrane
PR	Protease

PS	Phosphatidylserine
PtidIn	Phosphoinositides
RNA	Ribonucleic acid
RT	Reverse transcriptase
SANS	Small-angle neutron scattering
SARS-CoV	Severe acute respiratory syndrome coronavirus
SERINC5	Serine incorporator 5
SFV	Semliki forest virus
SIV	Simian immunodeficiency virus
SM	Sphingomyelin
SMase	Sphingomyelinase
SNARE	SNAP receptors
SP	Spacer region sequence in Gag
SRM	Super-resolution microscopy
STARD4	StAR related lipid transfer protein 4
STED	Stimulated emission depletion
STORM	Stochastic optical reconstruction microscopy
SU	Surface glycoprotein subunit gp120
SV40	Simian virus 40
TEM	Transmission electron microscopy
TIP47	Tail interacting protein of 47 kDa
TM	Transmembrane glycoprotein subunit gp41
tRNA	Transport RNA
TSG101	Tumor susceptibility gene 101
UUKV	Uukuniemi virus
VLP	Virus-like particle
VPS4	Vacuolar protein sorting-associated protein 4
VS	Virological synapse

II. List of figures

III. List of tables

IV. Summary

Assembly of Gag, the main structural polyprotein of HIV-1, drives virion biogenesis by recruiting and assembling the necessary factors at the plasma membrane (PM) of infected cells. Lipid rafts, microdomains rich in Cholesterol and Sphingomyelin (SM), are believed to serve as platforms for HIV-1 assembly and release. However, the localization, arrangement, composition, interactions, and diversity of these lipid domains remain poorly understood. In this work, I combined labeling of native Cholesterol and SM using recombinant fluorescence probes with stimulated emission depletion (STED) microscopy, to investigate lipid distribution at individual HIV-1 assembly sites within the plasma membrane of cells.

Gag assembly sites highly colocalized with Cholesterol- and SM-rich domains. Notably, one third of Gag domains were associated with a distinct ring-shaped lipid domain localized at the border of Gag assembly sites – coinciding with the extended ring-shaped envelope glycoprotein (Env) domain. Gag oligomerization at the PM in absence of all other viral proteins, including Env, was sufficient to induce formation of this lipid ring. Semi-automated image analyses and classification of Gag assembly sites based on their fluorescence intensity indicated a progressive recruitment of lipid microdomains. Punctate lipid domains more often associated with low-intensity Gag sites while half-ring and full-ring domains associated with respectively higher intensity and larger Gag domains. The Env ring domain largely overlapped with the lipid ring, but quantitative image analyses revealed the lipid ring to be on average ~15 nm closer towards the center of assembly. Punctate Cholesterol signal was also detected in released virus-like particles (VLPs), indicating that a portion of the lipid ring domain gets incorporated during budding. Gag^{CA3}, a mutant that is unable to generate PM curvature, lacked recruitment of Cholesterol-rich domains while Env recruitment was retained. However, only punctate Env domains were observed in Gag^{CA3}, which may result from altered interaction with the Gag^{CA3} lattice compared to Gag wild type.

Together these data indicate that the induction of negative curvature of the PM during Gag immature lattice formation and assembly is essential for the recruitment of punctate lipid microdomains, which transition into a distinct ring-shaped domain surrounding Gag. In conclusion, this study deepened our mechanistic understanding of HIV-1 assembly and provided a basis for further investigations of lipid-protein interactions in viral assembly and in a broader context, vesicle-mediated release events.

V. Zusammenfassung

Das Hauptstrukturpolyprotein von HIV-1, Gag, koordiniert die Biogenese von Virionen durch die Rekrutierung und Montage aller nötigen Faktoren an der Plasmamembran (PM) von infizierten Zellen. Es wird angenommen, dass dieser Prozess in Cholesterin und Sphingomyelin (SM)-reichen Mikrodomänen, sogenannten „Lipid Rafts“, stattfindet, welche als Plattform zur HIV-1 Montage und Freisetzung dienen. Jedoch sind Lokalisierung, Anordnung, Zusammensetzung, Interaktionen und Diversität dieser Lipid-Domänen noch nicht vollständig verstanden. In dieser Arbeit kombinierte ich die Markierung von nativem Cholesterin und SM mittels rekombinanten fluoreszenten Proteinsonden mit „stimulated emission depletion“ (STED) Mikroskopie um die Lipidverteilung in individuellen HIV-1 Montagestätten in der PM von Zellen zu untersuchen.

Ein großer Anteil der Gag Montagestätten kolokalisierte mit Cholesterin und SM-reichen Domänen. Erstaunlicherweise assoziierte ungefähr ein Drittel aller Gag-Domänen mit einer deutlichen ringförmigen Lipid-Domäne. Diese Lipidringe überschnitten sich mit der erweiterten Ringstruktur des HIV-1 Oberflächen Glykoproteins (Env) an der Grenze zum Gag Assemblierungsort. Die Oligomerisierung von Gag war in Abwesenheiten aller anderer viraler Faktoren, inklusive Env, ausreichend, um diese Lipidringstrukturen zu induzieren. Halbautomatische Bildanalyse und Klassifikation von Gag Montagestätten basierend auf der jeweiligen Fluoreszenzintensität deutete auf eine fortlaufende Rekrutierung der Lipid-Domänen hin. Punktartige Lipid-Domänen assoziierten öfter mit Gag-Domänen niedriger Intensitäten, während Halbringe und ganze Ringstrukturen jeweils mit größeren Gag-Domänen höherer Intensitäten assoziierten. Die Env-Ringstrukturen überlappten zum großen Teil mit den Lipid-Ringstrukturen, jedoch zeigte die quantitative Bildanalyse, dass sich die Lipidringe im Mittel um ~15nm näher am Zentrum der Montagestätte befanden. Punktartige Cholesterinsignale konnten auch in bereits freigesetzten virusartigen Partikeln nachgewiesen werden, was darauf hindeutet, dass ein Teil der Lipidring-Domäne während der Freisetzung in das Virion inkorporiert wird.

Gag^{CA3}, eine Mutante, die keine Krümmung in der PM induzieren kann, zeigte keinerlei Rekrutierung von cholesterinreichen Domänen. Diese Mutante rekrutiert zwar Env, aber nur als punktartige Struktur, was an einer veränderten Interaktion mit dem Gag^{CA3} Gitter im Vergleich zum Wildtyp liegen könnte.

Zusammen deuten diese Daten darauf hin, dass die negative Wölbung der PM während der Montage des unreifen Gag Gitters essenziell für die Rekrutierung von punktartigen Lipidmikrodomänen ist, welche sich anschließend zu deutlichen ringartigen Domänen um Gag herum entwickeln. Diese Arbeit vertieft unser mechanistisches Verständnis der HIV-1 Montage und bietet eine Basis für weiterführende Arbeiten zur Untersuchung von Lipid-Protein Interaktionen während der Montage von Viren und, in einem breiteren Zusammenhang, Vesikel-vermittelten Freisetzungsereignissen.

1. Introduction

1.1. Viruses

Viruses are the most abundant and diverse group of submicroscopic entities that infect organisms from every known kingdom. They greatly vary in size, the smallest viruses measuring only 20 nm in diameter (Stevenson et al. 1999; Meyvisch et al. 1974) while the largest, such as the giant *Mimivirus,* can measure up to 500 nm in diameter. They are usually spherical but can also be filamentous, such as members of the *Filoviridae* family and certain strains of Influenza, polyhedral such as Adenoviruses or complex in structure, such as various bacteriophages. All viruses, however, are genetically encoded by DNA or RNA which is protected inside a proteinaceous capsid shell, composed of ordered or semi-ordered lattice arrangements of viral protein monomers (Louten 2016). In addition to the capsid shell, many but not all viruses acquire a lipidic membrane envelope from their host cell, which aids in the infectious cycle. Despite employing diverse replication strategies, all viruses are obligate intracellular parasites, necessitating host cell machinery for their propagation and evolution. Out of tens of thousands of so far discovered virus species that infect mammals (Carlson et al. 2022), only 219 are currently known to infect and cause disease in humans (Woolhouse et al. 2012), while many more inhabit the human gut and skin microbiomes with no pathogenic effect (Liang and Bushman 2021). The vast majority of such viruses can infect other mammals as well, and often originated in other species before they spilled over into the human population.

1.2. Human immunodeficiency virus (HIV)

1.2.1. History and importance

Perhaps one of the most persistent global pandemics to date with a high disease burden and death toll, is the HIV pandemic that was identified in the early 1980s (Hymes et al. 1981; Kaposi's sarcoma and Pneumocystis pneumonia among homosexual men--New York City and California 1981) and is still ongoing in 2024 with an estimated death toll of approximately 40 million since its discovery (UNAIDS 2024).

Shortly after the first documented cases, the disease that is now termed Acquired Immune Deficiency Syndrome (AIDS) had started to emerge globally. Lymphadenopathy associated virus (LAV) was first identified as the causative agent of AIDS at the Pasteur Institute in France (Barré-Sinoussi et al. 1983) followed by the co-discovery in other labs (Marx 1984; Popovic et al. 1984; Broder and Gallo 1984). The names LAV and human T-lymphotropic virus type III (HTLV-III) were used in the early years post-discovery until the agent was renamed to HIV. The culprit of the ongoing pandemic is the HIV type 1 (HIV-1) virus lineage, while the less infectious HIV type 2 (HIV-2) accounts for only around 3% infections worldwide (Williams et al. 2023) and is characterized by a slower onset and progression of the disease. Serologically and phylogenetically HIV-2 is more similar to the simian immunodeficiency virus (SIV), which infects sooty mangabeys (SIVsmm), than to HIV-1 (Sharp and Hahn 2011).

Phylogenetic analysis of HIV and lentiviruses infecting primates revealed that the most likely origin of HIV-1 stems from multiple transmission events of the chimpanzee SIV (SIVcpz) to bush meat hunters in sub-Saharan Africa, which yielded the three phylogenetically distinct groups of HIV-1: main (M), outlier (O) and non-outlier (N) . Most recently, the rarest, pending (P) group was identified to originate from a gorilla SIV (SIVgor). Of those, group M of HIV-1 accounts for more than 90% of the contracted HIV-1 infections worldwide, being the most prevalent (Hemelaar et al. 2019).

1.2.2. HIV transmission and disease progression

HIV spreads via certain bodily fluids such as blood, semen, vaginal and rectal fluids as well as breast milk. Vertical transfer between a fetus and a mother can also occur since HIV can pass through the placenta while infections during labor were also documented. Saliva, sweat, urine and tears do not facilitate transmission however, due to the instability of the virus. HIV can also be transmitted via contaminated blood, either through needle sharing or blood transfusion, however most countries screen donated blood for the presence of HIV.

The progression of HIV infection can be subdivided into three stages: an acute phase, chronic HIV-1 infection and finally progression to AIDS. Upon infection, an incubation period of 1-6 weeks follows after which a rapid rise in the viral load heralds the acute phase of HIV infection. The risk of transmission is the greatest in this phase. The acute phase is frequently associated with symptoms such as fever, rashes, fatigue and headaches. At this stage the immune system mounts a largely

effective response greatly reducing the virus load, but not clearing the entirety of the virus. The chronic phase of clinical latency usually follows, where the viral load drops significantly and the replication remains low, usually presenting as mostly asymptomatic. With the constant depletion of CD4+ T cells, untreated individuals usually progress towards manifestation of AIDS symptoms anywhere from 2–10 years after infection. Development of opportunistic infections such as Herpes simplex-1 virus (HSV-1) infection, *Pneumocystis jirovecii* pneumonia (PJP), candidiasis, as well as emergence of Kaposi's sarcoma in individuals previously infected with Kaposi sarcoma associated herpes virus (KSHV) are common, and eventually lead to death.

Upon AIDS diagnosis, many patients lived only for up to 1-2 years before antiviral therapy was developed. With the discovery and advances in antiretroviral therapy (ART) and continued worldwide education campaigns, life expectancy of HIV patients has increased to multiple decades after diagnosis and reaches life expectancy of uninfected persons. The current highly active ART (HAART) consists of at least three drugs targeting viral replication and is the most commonly used treatment approach, however it cannot fully eliminate the virus. Due to the lack of an efficient vaccine or prevention strategies, still ~1.3 million people contract HIV yearly. According to current estimates as of 2022, 33-46 million people were living with HIV and 600,000 die yearly from HIV-related causes, making HIV an ongoing epidemic of high impact (van Schalkwyk et al. 2024). Due to poor education, poverty and inequality in access to medicine, low- and middle-income countries are experiencing the highest prevalence, morbidity and mortality rates.

1.2.3. HIV-1 structure, genome organization and life-cycle

There are two major classification systems for viruses, and according to the system of the international committee for taxonomy of viruses (ICTV) HIV-1 is classified in the genus of *Lentiviruses* of the family *Retroviridae* owing to the slow progression of the disease (Lenti - slow *lt.*) and its strategy of replication that utilizes the reverse transcriptase (RT) to convert its genome from RNA into DNA (Lefkowitz et al. 2018). The Baltimore scheme assigned classes depending on the replication strategy and HIV-1 belongs to the group VI (Baltimore 1971).

HIV-1 particles are spherical, enveloped and 120-140 nm in diameter. Its genome consists of two 9.7 kb positive sense, single stranded RNAs, which can be identical but may also carry different mutations. This RNA genome has three major open reading frames (ORF): *gag* – encoding the precursor of the main structural

viral polyprotein Gag*, pol* – encoding the Pol polyprotein precursor of Reverse Transcriptase (RT), Protease (PR) and Integrase (IN) enzymes and *env* – encoding the viral gp160 envelope (Env) glycoprotein, the precursor of the gp120 and gp41 subunits of the surface glycoprotein trimer (**Figure 1 A**). Additionally, smaller overlapping ORFs encode accessory and regulatory proteins Vif, Vpr, Vpu, Nef, Tat and Rev. The RNA coding regions are flanked on both ends by terminal repeat sequences (U3 and U5) which upon cell infection and RNA to DNA transcription by the RT enzyme get duplicated to form long terminal repeats (3'-LTR and 5'-LTR). Following cell entry, viral RNA is transcribed into the complementary DNA (cDNA) that is integrated into the cell host genome for which these LTRs are instrumental.

1.2.3.1. Gag

Gag is the 55 kDa structural polyprotein of HIV-1, accounting for roughly 50% of the virion mass. It is translated from unspliced genomic RNA (gRNA) on cytoplasmic polysomes. Gag mediates plasma membrane (PM) targeting and anchoring, viral RNA genome packaging and drives the assembly and release of the immature viral particle from the cell membrane. An interesting property of Gag is its ability to self-assemble into virus-like particles (VLPs) that bud off from the Gag-expressing cell in the absence of other HIV-1 genes*. In vitro* assembly of Gag was also performed successfully, where spherical and tubular particles were observed. The Gag polyprotein is composed of four domains: starting N-terminally with matrix (MA), capsid (CA), nucleocapsid (NC) and p6, all connected via flexible linker regions with spacer regions (SP) 1 and 2, inserted between CA and NC as well as NC and p6 respectively (**Figure 1 A and B**). In an immature viral particle, the Gag lattice is closely associated with the inner leaflet of the lipidic membrane via its MA domain while the C-terminal p6 domain faces inwards to the center of the particle (**Figure 1 C**). Five distinct PR cleavage sites are present in Gag, between each domain, including the spacer regions. Proteolytic activity of PR results in a time-coordinated separation of Gag domains into single subunits during the process of viral maturation. This process remodels the particle into a fully mature and infectious virus, where CA domains assemble into a conical capsid, ~100 nm long and 60 nm in diameter at the wide end, that carries the HIV-1 genome while the MA domains remain at the membrane in a lattice formation and NC condenses the RNA (**Figure 1 D**). The details of the maturation process and function of all Gag domains are described in detail in section **1.2.4.5** (page 19). All of the domains serve a variety of functions in the viral lifecycle, and most have multiple functions in different phases (Sundquist and Kräusslich 2012; Lerner et al. 2022; Sumner and Ono 2024).

Post-translational modification of Gag results in N-terminal MA myristoylation which in concert with the MA highly basic region (HBR) serves as a PM targeting and anchoring signal. Additionally, MA plays a role in Env incorporation (Tedbury et al. 2016; Tedbury et al. 2019; Dorfman et al. 1994; Freed and Martin 1996; Yu et al. 1992). The CA domain is responsible for Gag oligomerization and assembly progression as well as for construction of the capsid shell which harbors the genome of mature viral particles. The recruitment of the genomic RNA to Gag and its condensation is mediated by NC while the p6 domain mediates the release of immature particles from the PM by recruiting the components of the cellular ESCRT machinery (Sundquist and Kräusslich 2012; Lerner et al. 2022; Sumner and Ono 2024).

1.2.3.2. Pol

Via a regulated ribosomal -1 frameshift event of the unspliced genomic RNA at the 3' end of the *gag* gene, which overlaps with the *pol* 5' end, a GagPol polyprotein is translated at a ratio of Gag to GagPol of ~20:1 (Jacks et al. 1988). This strategy allows for a more compact genome due to the partial overlap of two sequences and the precise control of the ratio of Gag to enzymes which are targeted to the site of assembly via the MA domain of GagPol. Due to a low level of autocatalytic activity of the PR encoded in the Pol protein which results in initial PR release from GagPol, a start of the cascading cleavage events is possible wherein the newly cleaved PR monomers dimerize and initiate the cleavage of GagPol resulting in the liberation of RT, PR and IN enzyme monomers. One of the most successful therapy targets to date is RT, with two major classes of drugs developed to counter its activity: nucleoside RT inhibitors (NRTIs) and non-nucleoside RT inhibitors (NNRTIs). In combination with drugs targeting IN strand transfer (INSTIs) and PR (PIs), they make up the most important component of most HAART approaches.

1.2.3.3. Env

Env glycoprotein precursor, gp160, is composed of gp120 and gp41 subunits. Concomitant with translation of the singly spliced *Env/Vpu* biscistronic mRNA on the rough endoplasmic reticulum (ER), gp160 is O- and N- glycosylated with oligosaccharide side chains. On the membrane of the ER, gp160 oligomerizes into homotrimers with the transmembrane gp41 domains' cytoplasmic tail (CT) facing towards the cytoplasm while the gp120 domain is facing the ER lumen. On its way towards the PM through the secretory pathway, oligosaccharide chains are modified

and upon arrival to the Golgi, gp160 is proteolytically cleaved by host cell furin into mature surface glycoprotein (SU) gp120 and transmembrane (TM) glycoprotein gp41. The two glycoprotein subunits remain connected via noncovalent interactions and form trimers of gp120/gp41 heterodimer spike glycoproteins (Env) which are trafficked to the PM to be incorporated into viral particles. Interestingly, only a comparatively small number of 7-14 Env trimers is incorporated into released particles (Chertova et al. 2002; Zhu et al. 2006) - much less than was observed in its predecessor SIV (Zhu et al. 2006). However, this evolutionary change necessitated additional compensatory mechanisms for productive infection. Namely, Env trimers are somewhat randomly dispersed on the surface of the lipidic envelope of HIV-1, with the C-terminal cytoplasmic tail of gp41 protruding into the virion and interacting with the MA lattice (**Figure 1 C**). The maturation of Gag by proteolytic cleavage with the PR results in the clustering of Env trimers (**Figure 1 D**) which is a key step that enables Env-mediated fusion to occur. The gp120 domain is composed of five variable regions (V1-V5) which are interspersed with largely conserved amino acid sequences (C1-C5) while the transmembrane gp41 domain is composed of many functional domains which are extensively refolded upon receptor binding to induce fusion while its core six-helix bundle and the cytoplasmic tail baseplate keep it anchored to the viral membrane prior to fusion (Elalouf et al. 2024).

1.2.3.4. Regulatory proteins

Besides the *gag, pol* and *env* genes, HIV-1 RNA encodes for six additional auxiliary genes: *vif, vpr, vpu, tat, rev* and *nef* which are all translated from spliced mRNA products. These genes encode regulatory viral proteins which are essential in aiding in immune escape and enhancing the spread of the infection *in vivo* but are often not needed for cell culture infection to occur and persist.

The complete splicing of genomic mRNA results in a 1.8 kb transcript from which Nef, Rev and Tat are translated. Nef downregulates surface expression of CD4, SERINC5 and major histocompatibility class-1 (MHC-I) molecules (Buffalo et al. 2019; Pereira and daSilva 2016), enhances viral DNA integration and modulates many cellular pathways significantly speeding up the progression of the disease. It is crucial for development and progression of the disease, as patients infected with Nef-defective HIV-1 variants progress towards AIDS extremely slowly or do not develop it at all (Deacon et al. 1995; Gorry et al. 2007; Kirchhoff et al. 1995). Rev regulates the export of genomic and incompletely spliced viral mRNA from the nucleus and is essential for productive infection. The role of ‘Trans-activator of

transcription' or Tat is primarily to drastically increase the efficiency of viral transcription by multiple mechanisms.

Singly spliced mRNAs resulting in many of the 4 kb species produce Vif, Vpr and Vpu proteins besides the previously mentioned Env precursor. The canonical function of Vif is targeting APOBEC3G and 3F for degradation thereby preventing deleterious hypermutation of newly synthesized viral cDNA; however, recently it was also discovered to induce cell cycle arrest. In contrast to the rest of the regulatory proteins which have a prominent 'main' function, Vpr influences HIV infection in a multifaceted way: it induces G2 cell cycle arrest, aids in the nuclear import of the preintegration complex (PIC), sequesters Lysil tRNA ($tRNA^{Lys}$) into the viral particles, thereby enhancing the initiation of viral reverse transcription upon entry, and recruits cellular repair mechanisms to maintain viral genome fidelity and reduce mutation potential. Vpu is expressed in later stages of the viral lifecycle and it counteracts the restriction factor tetherin, mediates the degradation of primary viral CD4 receptors, and inhibits the activation of the transcription factor nuclear factor kappa B (NFkB).

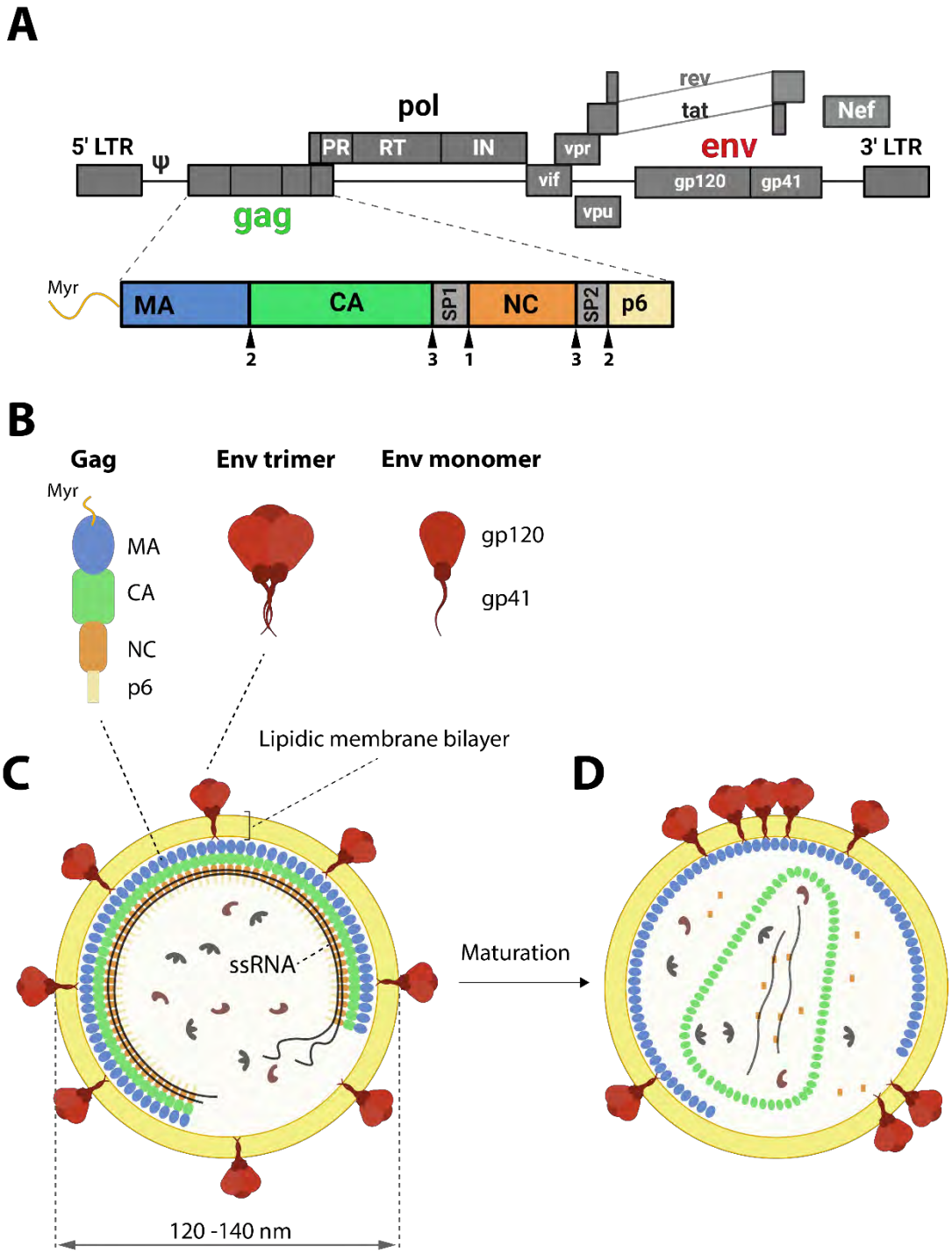

Figure 1. Genome organization and structure of HIV-1 particles. (A) A schematic map of the 9.7 kb long HIV-1 genome with the enlarged Gag segment outlining each domain in a separate color. **(B)** Cartoon representation of the Gag monomer with MA (blue), CA (green), NC (orange) and p6 (yellow) domains and the functional Env glycoprotein trimer structure built from the corresponding gp120 and gp41 heterodimer. **(C)** Structure of an immature HIV-1 particle and the positioning of respective Gag and Env proteins within. **(D)** Structure of the mature, infectious HIV-1 particle where the viral gRNA is condensed within a capsid shell while the Env trimers are clustered and can induce fusion. Figure was generated using Adobe Illustrator.

1.2.4. Lifecycle of HIV-1

1.2.4.1. Mode of virus spread

While cell free viral infections readily occur, the cell-to-cell transfer via a so called virological synapse (VS) is believed to be more relevant for *in vivo* viral spread and much more efficient. A virological synapse is generated by polarized particle release into the extracellular interface between two closely interacting cells. It was firstly observed in electron microscopy (EM) (Phillips and Bourinbaiar 1992) and later confirmed to facilitate a transfer of viral particles towards the acceptor cell (Jolly and Sattentau 2004; Piguet and Sattentau 2004; Haller and Fackler 2008). The cells are brought into contact via the interaction of polarized clusters of Env trimers displayed by the infected cell and non-infected T-cell expressed CD4 receptors as well as CXCR4/CCR5 coreceptors (Jolly et al. 2007; Vasiliver-Shamis et al. 2008). This initial binding induces further Env and Gag polarized recruitment in the infected cell and CD4, CXCR4/CCR5 and talin recruitment in the uninfected cell (Jolly et al. 2004) which facilitates a more stable junction between the cells. Transfers between infected and uninfected CD4+ T-cells, macrophages and CD4+ T-cells, infected dendritic cells and CD4+ T-cells have all been observed. An important factor preceding the formation of the VS is the polarized assembly of both HIV-1 Env and Gag at the PM of the infected cells accompanied by some of the tetraspanins and the microtubule organizing center (Haller and Fackler 2008). This polarized assembly of Env and Gag is dependent on the cytoplasmic tail of gp41 (Emerson et al. 2010) and Gag NC domain which targets Gag to the T-cell uropods (Llewellyn et al. 2010). Interestingly, the VS was found to be enriched in lipid-raft markers, while the depletion of Cholesterol abrogated VS formation (Jolly and Sattentau 2005), indicating that lipid order and organization may play a role in this process.

Despite the difference in efficiency of viral spread between cell-to-cell and cell-free infection, the underlying mechanisms of assembly, budding and entry do not seem to differ between the two. Assembling viral particles were observed to bud into the VS without any change in morphology albeit their local concentration is much larger then in cell-free infection.

1.2.4.2. Attachment and fusion

Regardless of the mode of viral particle transmission, HIV-1 infection starts by virus attachment to the cell surface after which Env spike glycoprotein trimer is eventually brought into contact with its primary receptor – CD4 (**Figure 2, step 1**). This interaction directs cell tropism primarily towards CD4+ T lymphocytes and

macrophage/monocyte lineages. One Env trimer can bind up to three CD4 receptors in a sequential manner, inducing sequential conformational changes in the trimer (Li et al. 2023b). For productive viral fusion and entry, Env interaction with CD4 is not sufficient and additionally requires the interaction with chemokine receptors CXCR4 (X4 tropic viruses) or CCR5 (R5 tropic viruses) which is initiated after conformational changes prime Env for co-receptor binding. As a function of the co-receptor used, different virus strains have been identified: 1) R5-T-cell tropic, 2) X4 T-cell tropic, 3) R5 macrophage-tropic (R5 M- tropic) and 4) dual tropic X4/R5 (Joseph and Swanstrom 2018). This tropism is defined by the V3 loop region of the *env* gene, and even single point mutations can result in a switch in tropism (Hartley et al. 2005).

After binding, a series of conformational changes in Env results in the insertion of the fusion peptide of gp41 into the PM thereby coupling the viral and cellular membranes and inducing a stepwise fusion process. Refolding of gp41 into a hairpin-like conformation in the six-helix bundle structure brings the two membranes into contact and results in membrane fusion (Lin and Da 2020; Murakami and Ono 2021). Thereafter, the contents of the virus are released into the cell cytoplasm, among which is the conical capsid core containing two copies of the viral RNA genome condensed by NC into a ribonucleoprotein complex (vRNP), as well as viral enzymes RT and IN among other factors (**Figure 2, step 2**).

1.2.4.3. Trafficking, integration and replication

Upon entry, reverse transcription of RNA into cDNA is initiated by the action of RT while the capsid core is transported via the microtubules towards the nucleus (**Figure 2, step 3 and 4**). Once the core with the partially translated genome, termed the preintegration complex (PIC), reaches the nuclear envelope, it docks at one of the many nuclear pore complexes (NPC) embedded within the nuclear envelope. Due to the width of the capsid (60 nm at the wide end) and nuclear pore size (~40 nm) (Appen et al. 2015), it was previously considered that an intact capsid cannot pass through into the nucleus and needs to be either partially or completely disassembled at or prior to nuclear entry. However, in the recent cryo-CLEM study, Zila et al. discovered intact capsid structures within the nucleoplasm, illustrating that capsid can remain largely intact during entry due to the wider diameter of the NPC (~64 nm) than was previously observed (Zila et al. 2021). Additionally, they found cracked capsid shell structures that lacked electron density (RNA) which advocated against the gradual disassembly of the lattice as the mechanism of cDNA release and towards mechanical breakage of larger capsid portions. A study by Müller et al. also found that the viral cDNA remains encased in a largely intact capsid structure

until after nuclear entry (Müller et al. 2021). They also observed empty capsid remnants and in one case a partially broken capsid with the nucleic acid density protruding out of the structure. Such polynucleotide loops protruding from the capsid while still associated with it, have been found in *in vitro* assembled capsids as well, where the loss of capsid integrity coincided with the completion of reverse transcription (Christensen et al. 2020). Since capsid uncoating was also observed *in vitro*, nuclear entry does not seem to be necessary for it, however the separation of viral cDNA from the initial PIC observed by Müller et al, which was not observed *in vitro*, suggests that the nuclear environment might play a role in uncoating, perhaps by mechanical cDNA extraction.

Before the capsid has even fully cleared the nuclear pore, it is rapidly decorated by the CPSF6 nuclear protein (**Figure 2, step 5**). This CA-CPSF6 interaction is responsible for the preference of HIV integration into highly transcriptionally active genes by way of translocation to nuclear speckle associated genomic domains (Francis et al. 2020) (**Figure 2, step 6**). The mechanism and driving force of capsid uncoating that is necessary to release the genome and initiate the integration is still incompletely understood, however recent models and AFM studies argue towards a possible mechanical trigger due to the increasing pressure inside the capsid from reverse transcription and the growing size of the cDNA. Integration into the host genome is catalyzed by tetramers of IN coupled with the ends of the viral cDNA which form the HIV-1 intasome (**Figure 2, step 7**).

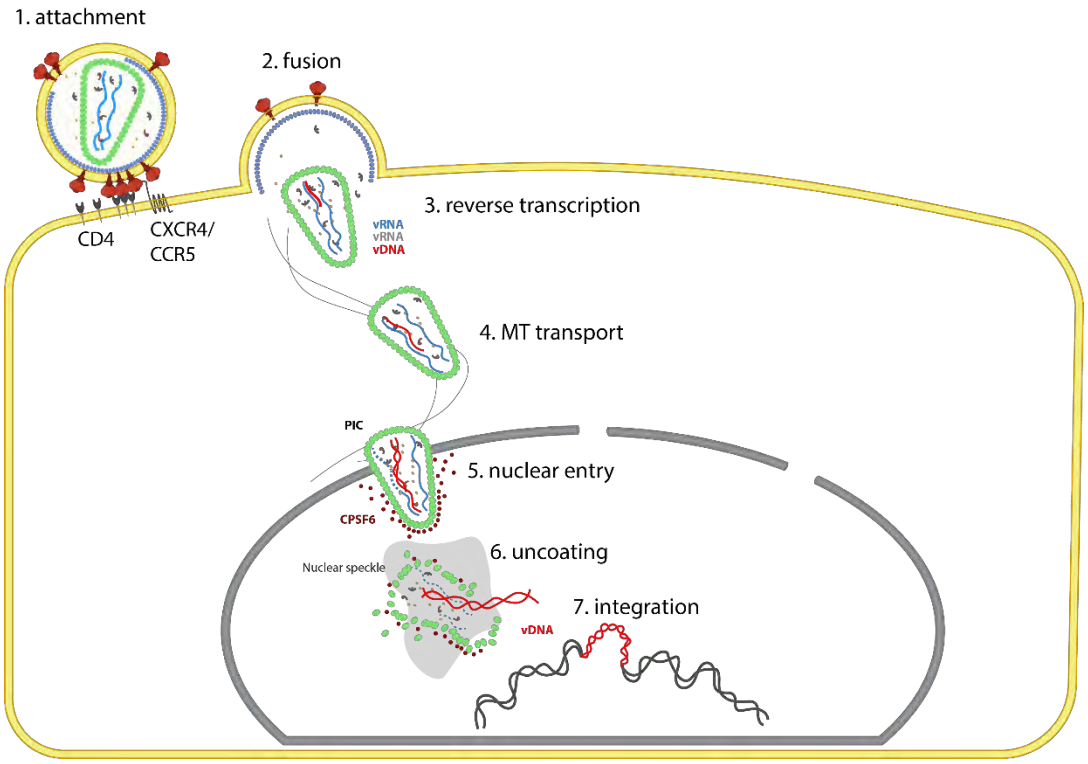

Figure 2. Early replication events in the HIV-1 lifecycle. After **(1)** Env mediated attachment to CD4 and coreceptors, the virion **(2)** fuses with the cell membrane, releasing the capsid containing the viral genome into the cytoplasm. **(3)** Reverse transcription of vRNA to viral dsDNA is initiated and **(4)** capsids are transported towards the nuclear pores via the microtubule network. **(5)** Nuclear entry of largely intact HIV-1 capsids is followed by association with the CPSF6 protein, **(6)** uncoating via an incompletely understood route in nuclear speckle regions, and **(7)** integration of the HIV-1 genome into the host's highly transcriptionally active genes. Figure was generated using Adobe Illustrator.

1.2.4.4. Assembly and budding

After successful integration, usually into highly transcriptionally active host genes, viral mRNA transcripts are generated. Unspliced full-length viral gRNA also serves as mRNA for Gag and GagPol, while incompletely spliced mRNA transcripts encode Env, Vif, Vpr and Vpu. Unspliced and incompletely spliced transcripts require Rev dependent nuclear export. In contrast, fully spliced mRNA transcripts that encode Nef, Tat and Rev are exported freely using the cellular nuclear export machinery (**Figure 3, steps 1 and 2**).

Upon Gag translation on cytoplasmic polysomes as the precursor $Pr55^{Gag}$, and its N-terminal myristoylation of the MA domain, Gag polyprotein is targeted towards the PM via an incompletely understood route (**Figure 3, steps 3 and 4**). Gag in the cytoplasm exists predominantly in a monomeric form and does not form higher-order oligomers until it reaches the PM (Kutluay and Bieniasz 2010; Hendrix et al. 2015). Once at the PM, Gag anchors to the inner leaflet via a specific interaction of the MA

domain with phosphatidylinositol-(4,5)-bisphosphate (PIP2) molecules (**Figure 3, step 5**). The myristoylation signal on the N-terminal glycine of MA is essential for PM targeting and anchoring and if deleted or mutated results in Gag mislocalization to the cytoplasm and internal membranes leading to severe assembly defects (Göttlinger et al. 1989; Bryant and Ratner 1990; Zhou and Resh 1996; Freed et al. 1994; Ono et al. 1997). While PIP2 is also present in organelle membranes, it is most abundant in the inner leaflet of the PM, which designates the PM as the primary site of HIV-1 assembly (Ono et al. 2004; Jouvenet et al. 2006; Chukkapalli et al. 2008; Jouvenet et al. 2008). A stretch of highly conserved basic amino acids termed the highly basic region (HBR) of MA additionally contributes to the anchoring via electrostatic interactions with the acidic headgroups of the leaflet phospholipids (Zhou et al. 1994). In order for Gag anchoring to happen, the extrusion of the partially sequestered myristoyl moiety from the MA hydrophobic pocket ("myristoyl switch") and insertion into the inner leaflet of the PM is necessary. Trimerization of MA is linked to myristate exposure, while monomeric forms sequester myristate (Tang et al. 2004). Additionally, in the full Gag construct, the equilibrium is greatly shifted towards the exposed myristate configuration as opposed to the MA domain alone (Tang et al. 2004). Saad et al. initially proposed a mechanism where binding of MA to PIP2 leads to myristate exposure and PM insertion, resulting in stable Gag anchoring and direction towards liquid ordered (Lo) domains (Saad et al. 2006). The authors identified a hydrophobic cleft in MA which could accommodate fatty acid residues of PIP2, which they argued could be a part of the mechanism inducing the switch. This proposition has been somewhat challenged by further structural and modeling studies however. Course-grained molecular dynamics models have indicated that MA only interacts with the sugar head of PIP2 without sequestering the acyl chain (Charlier et al. 2014). These models have also shown that MA could confine PIP2 all around its molecular surface indicating towards a potential mechanism of inducing its own lipid environment in the inner leaflet. Nuclear magnetic resonance (NMR) experiments confirmed that the acyl chain of PIP2 does not insert into MA and that the dynamic electrostatic interactions of MA with multiple PIP2 molecules likely predominantly govern anchoring (Mercredi et al. 2016). MA domain also interacts with tRNA in the cytoplasm, which is an important determinant preventing higher order Gag-Gag oligomerization in the cytoplasm and indiscriminate and non-specific organelle membrane binding by Gag (Chukkapalli et al. 2010; Alfadhli et al. 2011; Gaines et al. 2018; Bou-Nader et al. 2021). 2018. Taken together, the current anchoring model proposes that MA trimers with exposed Myr

moieties interact with the PM where the specific interaction between the MA-HBR and PIP2 outcompetes tRNA binding and further promotes Myr exposure whose hydrophobic interactions contribute to the stable anchoring (Alfadhli et al. 2009; Gaines et al. 2018; Alfadhli et al. 2011; Chukkapalli et al. 2010) that is sensitive to PIP2 depletion (Mücksch et al. 2017).

Gag monomers are recruited from the cytoplasm to the site of initial anchoring, rather than by lateral association of already anchored Gag domains (Ivanchenko et al. 2009). Shortly after anchoring, the oligomerization of Gag monomers into a continuous ordered lattice (Carlson et al. 2010) counting between 2000-3000 monomers is mediated by lateral interactions of the CA-SP1 regions and NC-RNA binding (**Figure 3**, **step 6**). These interactions also govern the incorporation of GagPol into the lattice and therefore the virion, ensuring the packaging of the necessary PR, RT and IN enzyme subunits. In the immature lattice, Gag is oriented with its MA domain attached to the inner leaflet while its C-terminal p6 domain points towards the center of the spherical particle. This lattice is a layered construct where MA and CA domains build differently ordered lattice conformations while still connected via a flexible unstructured region. Starting from the lipid membrane bilayer and going inwards, an irregular hexagonal lattice of MA trimers is juxtaposed on top of a CA hexagonal lattice built by C-terminal and N-terminal subdomains of CA (CA_{CTD} and CA_{NTD}) (Qu et al. 2021; Wright et al. 2007; Briggs et al. 2009). Due to the unstructured flexible link between the MA and CA domains, the two lattices are not fully fixed in their respective positions. An important factor for the assembly of the lattice is inositol hexakisphosphate (IP6) which gets incorporated into the central channel of the CA hexamer and helps to stabilize the repulsive forces between CA residues (Dick et al. 2018). As the Gag lattice grows, it curves outward from the cell cytoplasm building a dome and deforming the cellular lipid membrane in the process. The lattice remains incomplete towards the cytoplasm leaving a large gap approximately one third of the surface area of the virus. Concurrently with the growth of the lattice, the viral genome is recruited to the site via the interaction of its ψ element with the NC domain of Gag where it binds to the lattice and forms a ribonucleoprotein complex (D'Souza and Summers 2005). The two Zinc finger motifs of NC are essential for specific recognition and packaging of viral genomic RNA (Levin et al. 2005; Grigorov et al. 2007). The lattice grows until it forms a semi-spherical structure which is only possible by introducing defects and holes into the lattice to accommodate the shape as a purely uninterrupted hexameric lattice could not form a sphere (Briggs et al. 2009).

As mentioned before in section **1.2.3.3.** (page 5), the Env precursor gp160 synthesized at the ER is trafficked towards the PM where it arrives as a trimer of gp120/gp41 heterodimers independently of Gag trafficking (**Figure 3, step 4**). Once at the PM, the transmembrane gp41 subunit is embedded into the membrane with its C-terminal tail protruding into the cytoplasm while the gp120 ectodomain faces extracellularly. Env is rapidly recycled via the endosomal recycling compartment (ERC) from the PM which was shown to be essential for incorporation into budding particles due to the necessary FIP1C/Rab14-guided transport towards the assembly sites of Gag (Kirschman et al. 2018). Several non-exclusive models have been proposed for Env recruitment to assembly sites and incorporation into viral particles (Checkley et al. 2011). The direct Gag-Env interaction model proposes an interaction of the cytoplasmic tail (CT) of gp41 with MA as the mechanism and is supported by disruption of Env incorporation in MA mutants and rescue of those mutants by CT truncation (Freed and Martin 1995; Dorfman et al. 1994; Yu et al. 1992) as well as by evidence of direct binding between MA and CT (Alfadhli et al. 2019; Wyma et al. 2000). Additionally, virion maturation is required for the fusogenicity of Env for which Env clustering is needed, however CT truncation eliminates the need for maturation (Jiang and Aiken 2007; Murakami et al. 2004) suggesting that a potential MA-Env interaction might prevent early Env clustering. The trimerization of MA has also been shown to be important for Env incorporation, such that mutations that rescue MA trimerization also rescue Env incorporation (Tedbury et al. 2016; Tedbury et al. 2019). This is in line with and further supported by studies that found that MA trimerization results in a large central channel in the hexameric lattice, hypothesized to accommodate the long CT (Qu et al. 2021; Alfadhli et al. 2019).

A model of passive Env incorporation suggests, that Env randomly gets incorporated into the virion without any specific interactions with Gag. It originates from the fact that retroviruses readily incorporate foreign glycoproteins (pseudopyping) and various cellular proteins that they have no specific mechanism of incorporation for (Lusso et al. 1990; Arthur et al. 1992). Additionally, truncation of Env CT, even in its entirety still results in stochastic incorporation sufficient for infective virions to be generated in certain cell types (Wilk et al. 1992; Murakami and Freed 2000).

The co-targeting model proposes that Gag and Env are directed towards the same domains or domains that closely interact in the PM such as the lipid rafts. This model is supported by virion enrichment in raft lipids and high lipid order of the viral membrane (Aloia et al. 1988; Aloia et al. 1993; Brügger et al. 2006; Lorizate et al.

2009; Lorizate et al. 2013), Gag and Env co-patching with raft markers (Ono and Freed 2005; Pickl et al. 2001; Holm et al. 2003) as well as Gag-dependent direction of Env to rafts (Bhattacharya et al. 2006). Additionally, Ebola virus glycoprotein (EboG) and Env do not get copackaged within same virions when expressed together with Gag within the same cell, indicating directed assembly of these proteins at different microdomains (Leung et al. 2008)

Finally, the indirect Gag-Env interaction proposes that a cell host factor serves as a link between Gag and Env which brings them together. Clathrin adaptor protein 2 complex (AP-2) interaction with Env CT is well documented and necessary for clathrin-mediated endocytosis(Ohno et al. 1997; Berlioz-Torrent et al. 1999; Boge et al. 1998) and AP-2 was also shown to bind Gag (Camus et al. 2007; Batonick et al. 2005). Other proteins such as tail-interacting protein of 47 kDa (TIP47)(Blot et al. 2003; Lopez-Vergès et al. 2006), human discs large protein (hDlg1) (Blot et al. 2004), calmodulin, luman and prohibitin 1/2 dimer have all been implicated in this role, however a definitive function for these proteins has not yet been shown in the context of bridging Gag and Env interactions.

In contrast to other enveloped viruses which incorporate a large number of surface glycoproteins per particle (Einav et al. 2020; Beniac and Booth 2017), HIV-1 incorporates only around 7-14 trimers, indicating that this is a tightly regulated process (Zhu et al. 2003; Zhu et al. 2006; Chertova et al. 2002). The understanding of the mechanism behind it and the advantages it may confer remain unclear, however it is postulated that it contributes to immune evasion. Trimerization of MA was also found to be essential for Env incorporation (Tedbury et al. 2016), albeit the exclusion of Env in mutants that disrupt the MA trimer interface may be due to steric clash rather than abrogation of specific interaction. Current understanding proposes a model where the rigid Gag lattice would be largely exclusive towards the long gp41 CT tail and would accommodate it only at certain locations where complementarity between the lattice and the CT allows it (Buttler et al. 2018). Recent evidence revealed that the baseplate formed by the residues in CT align on top of the MA lattice offset from the central channel at the interface between two monomers (Mangala Prasad et al. 2022), in line with the study from Buttler et al. and further fortifying the importance of direct MA-Gag / Env interaction and supporting the model of lattice complementarity. Lattice curvature was not found to be important for Env retention and incorporation (Pezeshkian et al. 2019). In favor of the exclusion by the lattice complementarity is also the finding of the highly Env-enriched region encircling many Gag assemblies on the PM of producer cells, while only weak

fluorescence can be detected overlapping with the Gag signal directly (Muranyi et al. 2013; Mücksch et al. 2017; Muecksch et al. 2024). This clustering is dependent on the CT tail of Env and is lost in Env-CT truncations (Muranyi et al. 2013).

In the last steps of assembly the cellular endosomal sorting complex required for transport (ESCRT) machinery is hijacked by Gag and used to finalize the budding process by releasing the viral particle by scission of the bud neck (**Figure 3, step 7**). Specifically, the PTAP sequence of the p6 domain of Gag interacts with the tumor susceptibility gene 101 (TSG101) while the second YPXL sequence (where X varies in length and composition) recruits ALIX. Together, the complex of TSG101/ESCRT-I or ALIX recruits ESCRT-III components and VPS4 complexes which facilitate membrane fission and result in the release of an immature viral particle. Mutational perturbation of Gag interactions with TSG101 or ALIX resulted in significant reductions in particle release compared to Gag wild type (Gag^{WT}) and subsequent decrease in particle infectivity. The reason for the latter is the premature activation of PR before the full release of the particle, which results in digestion of GagPol and ultimately a release of viral particles largely devoid of RT, IN and PR enzymes (Bendjennat and Saffarian 2016; Huang et al. 1995). Mutations outside the conserved PTAP sequence are relatively well tolerated by the virus (Demirov et al. 2002; Huang et al. 1995). However, even subtle mutations within this conserved sequence result in severe budding defects where fully formed particles remain attached via a membranous stalk to the cell, unable to fully bud (Göttlinger et al. 1991). An important interferon-induced cellular response is the inhibition of budding completion by the protein tetherin, which is counteracted by HIV-1 accessory protein Vpu (Neil et al. 2008; van Damme et al. 2008; Hammonds et al. 2012). Particles that have already undergone ESCRT-mediated scission remain anchored to the surface of the cell via the tetherin protein bridge (Venkatesh and Bieniasz 2013; Hammonds et al. 2012; Hammonds et al. 2010). Vpu reduces tetherin expression at HIV-1 assembly sites by direct interaction and induces tetherin degradation and is therefore essential for particle release (McNatt et al. 2013; Hauser et al. 2010). The evolution from SIVcpz, whose Vpu cannot counteract the human tetherin and has relied on Nef to counteract the chimpanzee tetherin, towards the HIV-1 Vpu which counteracts human tetherin, has been implicated as one of the major reasons why group M HIV-1 is responsible for the majority of HIV-1 infections worldwide, while groups O, P and N which evolved partly functional Vpu remain less fit (Sauter et al. 2009).

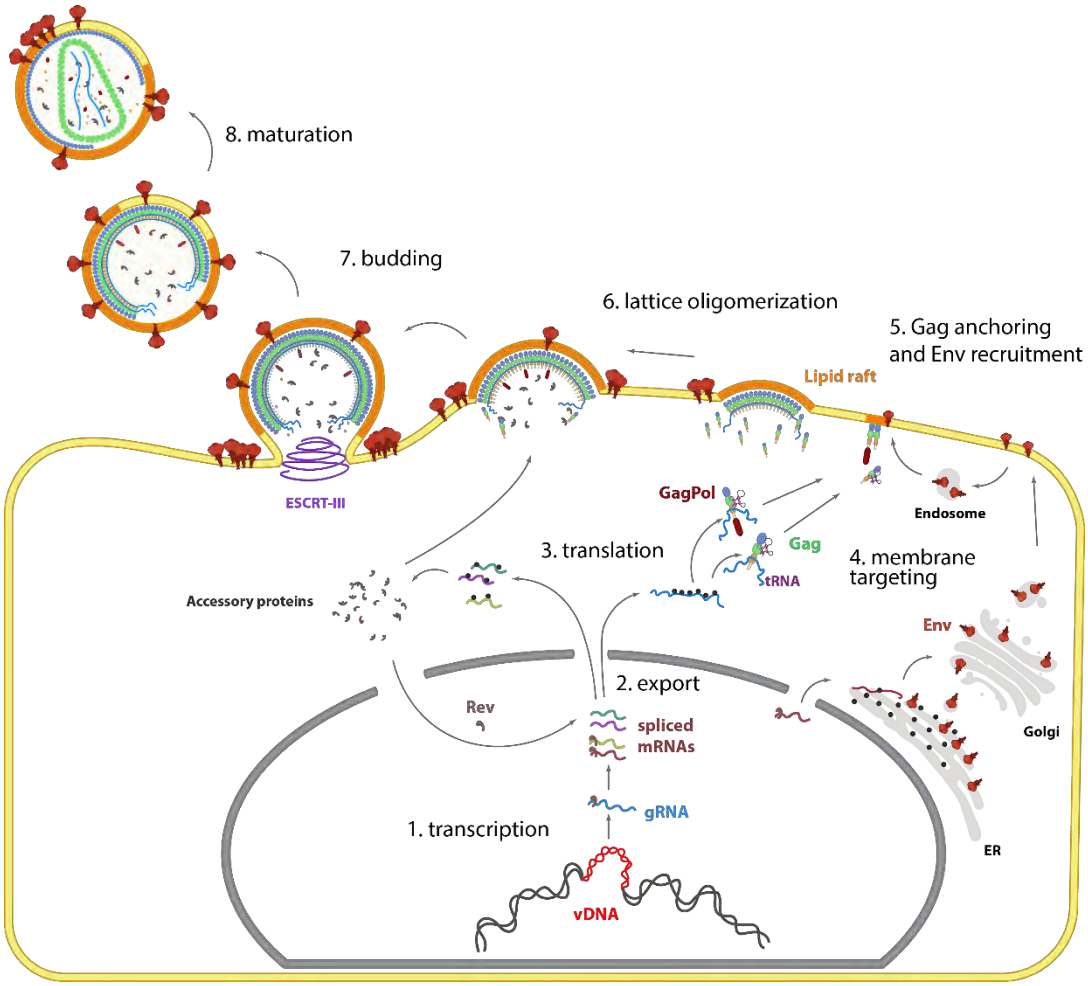

Figure 3. Late replication events in the HIV-1 lifecycle. (1) Viral DNA is transcribed into genomic RNA which is also spliced into mRNAs encoding Env and accessory proteins. **(2)** These are exported out of the nucleus where **(3)** gRNA is translated into Gag and GagPol on cytoplasmic ribosomes, the same as spliced mRNAs encoding viral accessory proteins while Env is translated at the rough ER. **(4)** Gag is targeted to the PM by an incompletely understood route and Env through the secretory pathway passing through the Golgi compartment where it is cleaved and assembled into trimers of gp120 and gp41 heterodimers which are rapidly recycled into the early endosome. **(5)** Gag is anchored to the inner PM leaflet via its MA domain while Env associates with newly generated Gag domains by lateral segregation. **(6)** Gag oligomerizes into a dome shaped lattice which deforms the cell membrane and recruits the gRNA. **(7)** At the late stages of budding the p6 domain of Gag induces recruitment of the ESCRT machinery by the p6 domain and budding is completed. Upon **(8)** proteolytic maturation of Gag and GagPol, the liberated CA domains construct a conical capsid shell which contains the NC-condensed gRNA dimer as well the viral enzymes while Env coalesces into larger clusters, thereby forming a fully infectious viral particle. The MA lattice remains associated to the viral membrane. Figure generated using Adobe Illustrator.

1.2.4.5. Maturation

In the newly released particle, Gag and GagPol undergo a cascade of sequential, time-coordinated cleavage reactions by the action of PR in the process called maturation, which is necessary for the viral particle to become infectious (**Figure 3, step 8**). Maturation ultimately results in the release of individual Gag domains and consequently the remodeling of the particle organization as these elements assume new roles. PR becomes fully catalytically active upon dimerization and its digestion sites are divided into slow (NC/SP2, CA/SP1), intermediate (SP2/p6, MA/CA) and fast (SP1/NC) (Pettit et al. 1994) (**Figure 4**).

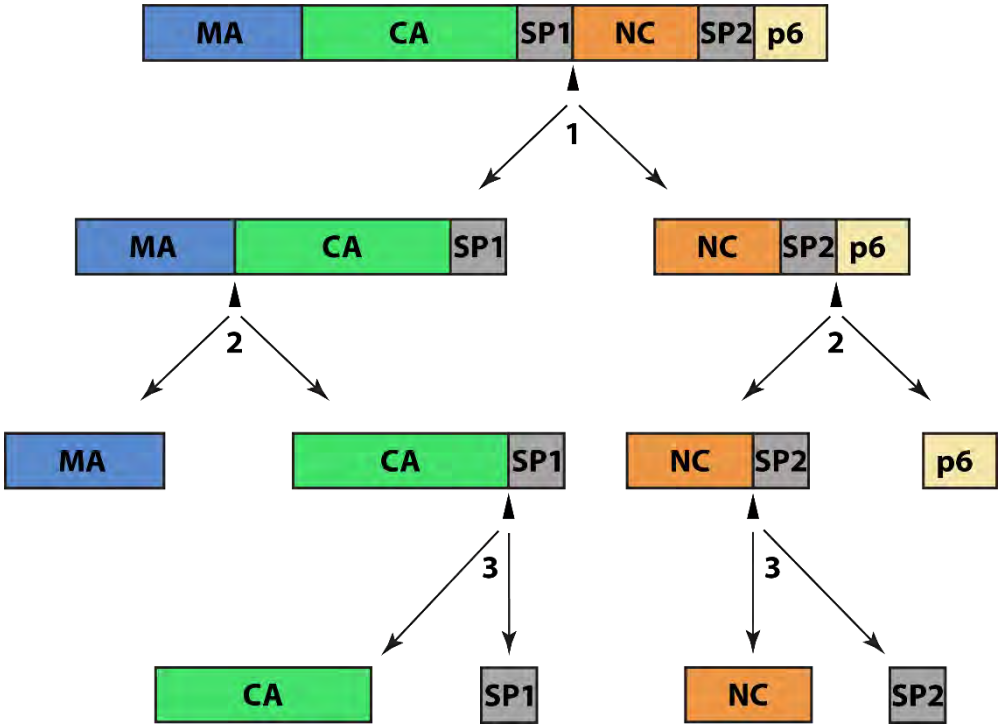

Figure 4. Processing activity of the PR enzyme towards specific sites in Gag. The processivity of PR is highest towards the SP1/NC site **(1)**, then towards the MA/CA and SP2/p6 sites **(2)** and the slowest towards CA/SP1 and NC/SP2 sites **(3)** which defines the time coordination of events in maturation.

This preference towards certain digestion sites over others is what defines the time control of the release of certain products, coordinating events to happen somewhat sequentially. The full digestion of Gag results in the liberation of MA, CA, NC and p6 domains as well as SP1 and SP2 spacer peptides. MA remains associated to the inner leaflet of the viral lipid envelope and interestingly a rearrangement in the lattice structure occurs (Qu et al. 2021) so that the lattice becomes more ordered while the central hexamer channel is constructed of

interacting HBR regions. The function of such a lattice transformation is so far not understood and it is speculated to have post-entry roles in signaling as well as in modulating the viral envelope properties. Approximately 1000-1500 CA monomers arrange into a conical capsid core with fullerene geometry, which envelops the NC bound RNA copies, $tRNA^{Lys}$, all viral enzymes and some cellular factors. The capsid core is ~100 nm long and 60 nm wide at its wide end. In order to accommodate the shape of a conical capsid, the hexameric CA lattice is interspersed with CA pentamers – exactly five at the narrow end and seven at the wide end. While this is the most abundant structure of capsids, “spherical” and “tubular” capsids occur when pentamer insertion into the hexameric lattice is symmetrical across the whole lattice or at both ends of the tube respectively. The function of such a structure is to protect the viral genome from cell restriction factors, mediate trafficking to the nucleus and ultimately to the site of integration. PR processing at the SP1/NC site activates the Env fusogenic potential and induces the condensation of the RNP complex (Marco et al. 2010), while the processing at the SP2 junction enables NC to stabilize the RNA dimer (Kafaie et al. 2008; Ohishi et al. 2011). By the processing of GagPol polyprotein, the release of RT, IN and PR is achieved. RT and IN interact with the genomic RNA and get packaged into the core where they will serve to initiate DNA genome synthesis via reverse transcription and subsequently integration into the cell genome.

Most HIV-1 strains require 2-3 trimers to interact with receptors for successful fusion (Brandenberg et al. 2015), which is unlikely to happen in an immature virus due to low Env number and random dispersion across the surface of the virion. A transformation instrumental for the infectivity of the particle that is achieved through the activity of the PR is the clustering of the majority of Env trimers into a large functional domain essential for fusion. This reorganization is governed by the processing at the SP1/NC site and release of NC (Wyma et al. 2004). In the process of maturation, the mobility of Env in the lipid bilayer increases (Chojnacki et al. 2017), contributing to clustering, while the presence of Cholesterol in the membrane seems essential (Nieto-Garai et al. 2021). Additionally, the dissolution of the Gag lattice shell, which likely restrains the movement of Env trimers through a direct interaction of MA and the CT of Env (Mangala Prasad et al. 2022), allows for increased mobility and repositioning of the trimers (Chojnacki et al. 2012).

1.3. Lipids and plasma membrane organization

Lipids, and the structures they build, are essential for all known forms of life. They form the cellular membranes that are essential for bacteria, archaea and eukaryotes alike. They serve as signaling molecules and hormone precursors, store energy and are crucial for nutrient absorption in eukaryotes. Consequently, their production is tightly regulated and differs according to the specific needs and functions of the cell at any given moment. Lipids are not genetically encoded so their homeostasis depends on the enzymatic regulation of *de novo* lipid synthesis, metabolism and dietary intake. Eukaryotic cells can synthesize lipids from carbohydrates and proteins via lipogenesis, Cholesterol synthesis, phospholipid synthesis and ketogenesis. Through these processes, a vast number of lipid species is produced, all serving a specific function.

The plasma membrane of eukaryotic cells is a complex lipid bilayer built from three major classes of lipids: 1) glycerophospholipids, 2) sphingolipids and 3) sterols (Fahy et al. 2011). Glycerophospholipids comprise the bulk of the membrane, with their hydrophilic headgroups exposed on one side to the extracellular environment and on the other to the cytoplasm while their hydrophobic tails are interposed in between (van Meer et al. 2008). Major glycerophospholipid classes in the PM include phosphatidyl choline (PC), phosphatidyl ethanolamine (PE), phosphatidyl serine (PS) and phosphatidyl inositol (PI) depending on the head group attached to phosphate residue. Cholesterol, as the most abundant sterol in the PM can comprise up to 50% of total lipids of the eukaryotic membrane and is an important regulator of membrane tension, fluidity and permeability. Interestingly, only a few bacteria have been found whose membranes contain cholesterol (Smith 1971; Lin and Rikihisa 2003; Haque et al. 1995), while plants use phytosterols instead. Sphingolipids are highly active signaling molecules often serving as secondary messengers and cell growth and differentiation factors abundant in the outer leaflet of the PM (Lingwood 2011; Varki 2017). Major sphingolipid classes include ceramide (Cer), sphingomyelin (SM) and glycosphingolipids (GSLs) (Harayama and Riezman 2018). Phosphoinositides make up only a small fraction of the PM phospholipids, however they were uncovered as important signaling and membrane targeting factors for a large number of proteins (Balla 2013). As mentioned above, the phosphoinositide PIP2 is recognized as an instrumental signal for Gag membrane targeting and stable anchoring.

Despite the ever-changing environment and external stimuli such as temperature, pressure or solvents, the PM retains a relatively constant composition. This is owing to the rapid adaptability of homeostatic mechanisms that maintain it. Synthesis of lipids and their transport occurs from the ER and Golgi networks while removal and recycling are done via retrograde transport (Watson 2015; Glatz et al. 2010). Lipids can also be transferred within the PM by lateral diffusion as well as between the leaflets (flip-flop) owing to the action of ATP-driven flipases, flopases and scramblases which are enzymes that mediate phospholipid rearrangement. These enzymes generate and maintain a prominent asymmetry in composition between the leaflets such that the outer leaflet is more enriched in PC and SM while the inner leaflet contains more of PS and PE (van Meer and Kroon 2011).

While phospholipids require enzymatic activity for rearrangement between the leaflets, Cholesterol and other sterols do not. This is owing to their comparatively small polar –OH group which requires less energy for flipping through the hydrophobic core. This allows for a rapid Cholesterol flipping between the leaflets (Steck and Lange 2018) that is likely influenced by the difference in membrane tension, curvature of the bilayer and abundance of other lipid species between the leaflets. Nevertheless, the specifics of Cholesterol asymmetry remain controversial. Cytoplasmic leaflet enrichment was observed experimentally (Giang and Schick 2014; Marquardt et al. 2015; Wood et al. 2011), and interaction of Cholesterol with SM was also shown (Nicolson 2014) which could potentially recruit Cholesterol to the outer leaflet. Such outer leaflet enrichment is favored by *in silico* modelling studies as well (Yesylevskyy and Demchenko 2012; Choubey et al. 2013; Marquardt et al. 2016). A recent study by Liu et al. quantitatively imaged Cholesterol domains on the inner and outer leaflet simultaneously, arguing for a 10-fold enrichment of the outer over the cytoplasmic leaflet via an active transport mechanism (Liu et al. 2017). In contrast, reports from other studies that utilized the same Cholesterol probes reported much higher inner leaflet concentrations then suggested by Liu and colleagues (Maekawa and Fairn 2015; Abe et al. 2012; Johnson et al. 2012). Taken together, it is predicted that most eukaryotic cells should have the same Cholesterol interleaflet distribution while active transport seems unlikely but not entirely discounted. The importance and presence of Cholesterol asymmetry therefore remains somewhat inconclusive. A large number of studies estimate average Cholesterol levels in PM at ~40% mol/mol of other lipid species, however phase separation of the leaflet lipids may induce much higher local concentrations within certain microdomain boundaries.

1.3.1. Lipid rafts

It has been postulated that Cholesterol aggregates with sphingolipids and phase separates into highly organized but highly dynamic lipid microdomains called “lipid rafts” (Simons and Ikonen 1997), the existence of which was a debated concept until recently owing to the difficulties of direct domain observation in living cells. The discovery of the phase separation of lipids in membranes to liquid ordered (Lo) and liquid disordered (Ld) phases supported the existence of lateral compartmentalization (Ipsen et al. 1987; Brown and London 1997; Ahmed et al. 1997). Additionally, such domains have been observed and extensively studied on giant unilamellar vesicles (GUVs) (Veatch and Keller 2003, 2005; Sezgin et al. 2012; Montes et al. 2010) and giant-plasma membrane derived vesicles (GPMVs) (Sezgin et al. 2012; Heberle et al. 2020; Cornell et al. 2020; Baumgart et al. 2007) via fluorescence and electron microscopy. In 2006, a definition of lipid rafts has been established based on current knowledge at the time: “lipid rafts are heterogeneous and dynamic Cholesterol and SM rich lipid domains averaging between 10 – 200 nm in size, with the capacity to self-assemble creating submicroscopic domains induced by lipid-lipid and protein-lipid interactions” (Pike 2006). That definition has since been supported by a plethora of various approaches. The most recent promising study reported on live-cell Cholesterol domain visualization via a stimulated emission depletion (STED) microscopy approach utilizing a Cholesterol probe with an azide group and copper-free click chemistry (Lorizate et al. 2021). They observed that the majority of PM Cholesterol exists within Lo, highly dynamic microdomains predominantly <50 nm in size, which transiently trap Cholesterol within its boundaries. Differing levels of domain order were discovered based on their Cholesterol content and mobility, indicating a more complex system than the proposed duality of Lo/Ld separation (Lorizate et al. 2021). The proposed function of lipid microdomains is facilitating the interaction between proteins with the propensity to segregate into Cholesterol/SM-rich domains.

1.4. Role of lipids in the lifecycle of viruses

Besides serving essential roles in eukaryotic and prokaryotic cells, lipids have been increasingly uncovered as important factors in the lifecycle of viruses. For example, lipids can facilitate virus entry, as was shown for the Simian virus 40 (SV40) where gangliosides in the PM aid virus binding (Anderson et al. 1996; Tsai et al. 2003). Another example is hemagglutinin A (HA) of the Influenza A virus (IAV)

for which entry was shown to be mediated via attachment to lipid microdomains (Takeda et al. 2003; Verma et al. 2018; Hu et al. 2019; Anderson et al. 1996). During Ebola virus (EBOV) entry, interactions of glycoproteins with Cholesterol were suggested to induce fusion (Lee et al. 2021). PS incorporated into viral envelope of several viruses was shown to be utilized as a binding factor (Moller-Tank and Maury 2014). A recent study has shown that glucosylceramide (GlcCer) incorporation into particles of the Uukuniemi virus (UUKV) as well as Toscana virus (TOSV) is important for binding to target cells (Uckeley et al. 2024). The importance of lipid rafts was also highlighted in studies of SARS-CoV-1 and 2 entry (Sanders et al. 2021; Fecchi et al. 2020; Glende et al. 2008; Li et al. 2021).

Other viruses rely on various lipids or lipid reorganization for genome replication. The formation of replication organelles by remodeling of the PM was documented for various +stranded RNA viruses, such as Hepatitis C virus (HCV), Dengue virus (DENV), poliovirus, SARS-CoV-1, coxsackievirus B3, Semliki forest virus (SFV) (Spuul et al. 2010; Limpens et al. 2011; Knoops et al. 2008; Belov et al. 2012; Welsch et al. 2009; Gosert et al. 2003). As viral membranes of enveloped viruses derive from cellular membranes, cellular lipid bilayers also play important roles during assembly and egress of enveloped viruses. Using electron tomography (ET), vaccinia virus assembly was shown to utilize open membrane sheets generated by membrane ruptures (Chlanda et al. 2009). Furthermore, cytosolic lipid droplets were suggested to play an important role for HCV assembly (Awadh 2023; Bartenschlager et al. 2011). Often, the lipid composition of the organelle that the respective virus buds through dictates the composition of the viral envelope (Kalvodova et al. 2009; Simons and Warren 1984). Interestingly, other viruses are able to locally or globally alter the lipid composition in their host cell leading to enrichment or reduction of certain lipids in the viral envelope (Uckeley et al. 2024; Mücksch et al. 2019; Ichihashi and Oie 1983; Gerl et al. 2012; Liu et al. 2011).

1.4.1. Role of lipids and microdomains in HIV-1 assembly

As many other enveloped viruses, HIV-1 acquires its lipid membrane from the PM of the producing cell. In contrast to many viruses however, the composition of the viral HIV-1 envelope and that of the PM were found to be different. The first lipid composition studies by Aloia et al. found enrichment of PE, PS, SM and Cholesterol whereas the membrane fluidity was reduced (Aloia et al. 1988; Aloia et al. 1993). Advances in molecular techniques and mass spectroscopy (MS) have allowed for more precise isolation of subcellular compartments and a much more detailed

analysis of the lipid composition of both the viral envelope and the PM of producing cells. An enrichment of Cholesterol and SM, as well as plasmalogen-PE (pl-PE), PS and an increase in saturated fatty acids compared to the producer cell membrane was discovered (Brügger et al. 2006). Chan et al. largely confirmed these findings and found an additional enrichment of PIP2 compared to PM of monocyte derived macrophages (MDMs), in line with the discovered MA-Gag interaction (Chan et al. 2008). More recently, a cell-type comparative study, with a particular focus on improved PM isolation protocol, found a less prominent enrichment of certain lipids while the majority of previous findings were confirmed (Lorizate et al. 2013). Notably, Cholesterol enrichment was not observed to be so drastic, however viruses specifically produced from MT-4 but not HeLa cell line were grossly enriched in hexosylceramide (HexCer) and phosphatidylglycerol (PG) (Lorizate et al. 2013). More recently, a detailed quantitative lipidomics study of HIV-1 particles focused on phosphoinositides revealed a high enrichment of PIP2 but also PIP3 in viral envelope, estimating a 3:1 ratio of PIP2:Gag (Mücksch et al. 2019). Taken together, the majority of studies agree that due to particle enrichment in CHOL, SM, pl-PE and saturated lipids, HIV-1 assembly likely occurs at specialized lipid microdomains similar to lipid rafts, and different in composition from the majority of the PM. One of the standing questions in this matter is whether Gag is recruited to preexisting domains or (more likely) induces the generation of a special lipid environment during assembly and how this environment might be generated.

While lipidomic studies are somewhat polarized on the enrichment of Cholesterol in viral particles, the importance of Cholesterol for viral egress and infectivity has been previously demonstrated. Cholesterol depletion from producer cells resulted in a drastic decrease in virion release, while treatment of viral particles with raft-disrupting agents impaired infectivity (Ono and Freed 2001; Ono et al. 2007). In addition, Gag was found to be enriched in isolated detergent-resistant membranes (DRM) (Nguyen and Hildreth 2000), a portion of membranes which contains high Cholesterol/SM content but was since disproven to exist as such *in vivo*. Raft-favoring GPI-linked proteins such as CD59 and Thy-1 as well as ganglioside GM1 are incorporated into viral particles while CD45 - a transmembrane protein which is excluded from lipid raft domains (Arni et al. 1996; Rodgers and Rose 1996) is not incorporated (Nguyen and Hildreth 2000). Co-localization of GM1 and Gag and induced antibody clustering of Gag via GM1 was shown in confocal studies, indicating association with rafts (Holm et al. 2003). Recent advances in discovery of new lipid probes and super resolution microscopy (SRM) have shed more light onto

this matter. Yandrapalli et al. demonstrated that self-assembly of Gag on model membranes induces the co-clustering of Gag with PIP2 and Cholesterol analogs but not that of SM-analog domains (Yandrapalli et al. 2016). The same team has later reported on utilizing stimulated emission depletion fluorescence correlation spectroscopy (STED-FCS) in living cells infected with NL4-3 strain of HIV-1 viruses to show that Gag assemblies transiently trapped PIP2 and Cholesterol while SM analogs appeared to be unaffected (Favard et al. 2019). Sengupta et al. also reported on colocalization between SM and Cholesterol analogs with Gag, arguing that this lipid coalescence at the assembly may facilitate the incorporation of certain proteins into HIV-1 particles (Sengupta et al. 2019). More recently, Tomishige et al. used a photoactivated localization microscopy (PALM) with stochastic optical reconstruction microscopy (dSTORM) in combination with recombinant lipid-binding probes to show colocalization of native Cholesterol and SM domains with Gag, arguing that clustering of such domains happens in a Gag dependent and curvature dependent manner (Tomishige et al. 2023). Taken together, the evidence for Cholesterol/SM-rich lipid domain association with Gag during HIV-1 assembly is convincing and supported by a number of studies over the years. Gag seems to mediate the recruitment of these domains and curvature of the membrane has recently been implicated in the process.

Several important factors need to be carefully considered when interpreting the mechanism by which Gag might recruit and induce the clustering of lipid raft domains. Firstly, our understanding of lipid rafts as a general principle has improved over the last years but still remains incomplete with only a single study visualizing such domains in live cells (Lorizate et al. 2021). The more saturated outer leaflet of the PM was shown to have a higher degree of order and lipid packing in comparison to the cytoplasmic leaflet which is more abundant in unsaturated lipids (Lorent et al. 2020). This may be due to the higher abundance of SM in the outer leaflet which together with saturated acyl chains packs more tightly and interacts with Cholesterol via hydrogen bonding to construct Lo domains. However, evidence from supported (Wan et al. 2008; Visco et al. 2014) and unsupported asymmetric bilayers (Collins and Keller 2008) as well as live cells (Yang et al. 2023) indicates that a change in outer leaflet order influences inner leaflet order, likely through interleaflet coupling via acyl chain interdigitation. In the study on asymmetric GUVs, Lin and colleagues found that outer and inner raft domains were in register, i.e. they were occupying the same relative xy coordinates on the membrane plane (Lin and London 2015). Such phenomenon depended on the type of SM used in their experiments, such that the

milk-derived SM, carrying longer acyl chains on average 22-24 carbons long, showed interdigitation interactions, while the shorter chain ,egg-derived SM did not. Additionally, they found that the registered ordered phases do not necessarily need to have the same level of packing, meaning that they can be compositionally different. These observations have also been confirmed in a more recent study on GUVs (Enoki and Heberle 2023), where in the absence of Cholesterol, phase separation was observed between saturated and unsaturated lipids and outer leaflet domains without corresponding in-register inner leaflet domains were also observed.

Current microscopy techniques investigating Gag influence on lipid raft recruitment and coalescence have relied on Cholesterol or SM analogs supplemented to living cells. Due to the large fluorophore molecules such as boron-dipyrromethene (BODIPY) or ATTO647N covalently bound to SM or Cholesterol, these lipids can only distribute within the outer leaflet and therefore all observations of Gag lipid trapping (Yandrapalli et al. 2016; Favard et al. 2019) refer to outer leaflet lipids only. This is also true for the study that used Cholesterol and SM sensitive lipid probes which stain native outer leaflet lipids (Tomishige et al. 2023).

Considering that Gag is not a transmembrane protein its influence over the outer leaflet and specifically in modulating Cholesterol/SM rich domains, could be achieved through multiple different modes: 1) direct interaction with cytoplasmic leaflet domains (such as PIP2 domains) that couple to the outer leaflet domain or induce its formation, 2) induced flip-flop of Cholesterol from inner to the outer leaflet at the sites of Gag assembly resulting in outer layer enrichment, 3) indirect interaction via an unknown protein or lipid factor inducing clustering and recruitment of outer leaflet Lo domain either in register or out of register with corresponding inner leaflet domain. Direct interaction of Env gp41 with Cholesterol has been recently reported (Nieto-Garai et al. 2021) while the recruitment of Env to the assembly domains likely occurs via a direct interaction with Gag. If Env recruitment happens through a direct interaction with Gag, an indirect recruitment of Lo domains to Gag assembly domains with Env acting as a sort of lipid chaperone presents as an interesting potential concept.

1.4.2. Role of PIP2 in HIV-1 assembly

The lipid that is most unambiguously essential for HIV-1 assembly is PIP2. Phosphoinositides (PtidIns) are a class of phosphorylated phosphatidylinositols (PIs) that are once, twice or thrice phosphorylated at positions 3,4 and/or 5 of the inositol headgroup. They are key determinants of cellular membrane identity as

different compartments have dominant populations of one PtidIn over others (Balla 2013; Bilanges et al. 2019; Di Paolo and Camilli 2006). They are therefore instrumental in spatial direction of membrane processes. PI(4,5)P2 is predominantly located in the inner cytoplasmic leaflet of the PM where it serves as an important mediator of cell signaling via its metabolism to diacylglycerol (DAG) and inositol-1,4,5-triphosphate (IP3).

Its importance in HIV-1 assembly was discovered by Ono and colleagues when they observed Gag relocalization from the PM to the cytoplasm upon membrane PIP2 depletion, which consequently resulted in reduced particle release (Ono et al. 2004). Mutating residues in the HBR of MA resulted in similar Gag mislocalization to the intracellular compartments (Ono et al. 2004), indicating that the HBR interaction with PIP2 may be key for PM targeting. Indeed, Saad et al. have shown a direct interaction between MA HBR and PIP2 by performing nuclear magnetic resonance (NMR) on solubilized PIP2 analogs (Saad et al. 2006).

Residues 29-31 of MA were discovered to be crucial for this interaction (Chukkapalli et al. 2008; Shkriabai et al. 2006), and multiple studies confirmed Gag targeting to the PM depended on these residues (Ono et al. 2000; Ono and Freed 2004; Gousset et al. 2008). As described in section **1.2.4.4** (page 12), current knowledge suggests that electrostatic interactions between MA and PIP2 without sn-2 acyl chain insertion into MA governs the anchoring to the cytoplasmic leaflet. (Chukkapalli et al. 2010; Alfadhli et al. 2011; Kutluay et al. 2014). (Chukkapalli et al. 2013; Todd et al. 2017; Sumner et al. 2022).

1.5. Lipid labeling and microscopy

Owing to their small size, rapid dynamics and complex metabolism, studying lipids by microscopy has only been possible since relatively recently due to the advances in labeling tools and microscopy techniques. The first direct observations of membranes were done by EM (Sjostrand et al. 1958; Robertson 1959, 1960), allowing for the confirmation of the hypothesis of the bi-layered structure of the PM (Gorter and Grendel 1925). However, such early attempts could not discern individual lipid species nor study the dynamics of lipids due to cell fixation being the prerequisite for EM. Current approaches to visualizing lipids can be separated into label-free and labeled lipid approaches. Label-free approaches such as transmission electron microscopy (TEM) and cryogenic EM (cryo-EM) can provide very high

spatial detail, achieving even sub-angstrom resolution of membrane bilayers (Heberle et al. 2020), but lack the ability to study individual lipids without labeling and are a fixed-cell approach. In contrast, high temporal dynamic observations of lipid domains can be achieved with small-angle neutron scattering (SANS) without labeling as demonstrated by de Wit and colleagues (Wit et al. 2015). Another upcoming approach that combines mass spectrometry with imaging (MSI) can provide high resolution in species identification but is still a somewhat underdeveloped technique that suffers from low spatial resolution and needs to be performed in fixed cells (Li et al. 2023a).

If one is interested in cellular or sub-compartment distribution of specific lipids however, direct labeling is necessary. As this work focuses heavily on membrane imaging of two lipids in particular: Cholesterol and SM – the techniques pertaining to those specifically will be further described.

1.5.1. Filipin

Filipin is an inherently fluorescent, sterol-binding polyene macrolide antibiotic isolated from *Streptomyces filipinensis*, a soil bacterium originally discovered in the Philippines, which is how it got its name (Whitfield et al. 1955). It is a mixture of multiple compounds with the highest relative percentage in the extract being Filipin III. Filipin binds to unesterified Cholesterol (Kruth and Fry 1984; Schroeder et al. 1972) however the exact mechanism of recognition is not fully understood. Additionally, it was discovered that Filipin can bind other lipids besides Cholesterol, such as ergosterol and ganglioside GM1 (Arthur et al. 2011). Since it perturbs membranes, it cannot be used to stain lipids in live cells. Finally, its excitation maximum of 360 nm results in poor signal intensity when used with the common 405 nm lasers, while its photostability is extremely poor. Taken together, such a probe is not suitable for high spatial resolution imaging while temporal imaging is not possible at all. Nevertheless, this probe is still used in diagnosis of the Niemann-Pick disease type C (NPC) (Blanchette-Mackie et al. 1988; Alpy et al. 2001; Vanier and Latour 2015), and it was important for advancing the understanding of this illness (Pentchev et al. 1985; Carstea et al. 1997; Blanchette-Mackie et al. 1988), as well as uncovering possible future treatment strategies (Rujoi et al. 2010; Pipalia et al. 2006).

1.5.2. Pore-forming toxins as lipid probes

1.5.2.1. Cholesterol-dependent cytolysins

Bacteria from the genera Listeria, Clostridium, Streptococcus, Bacillus and Arcanobacteria have been shown to secrete Cholesterol dependent cytolysins (CDCs) into the extracellular environment, which contribute to a large number of pathogenic mechanisms. These are single-chain proteins that necessitate the presence of Cholesterol in membranes for attachment, which results in the oligomerization of monomers into pore-forming units that ultimately lyse the cell. One of the most well-known and extensively characterized toxins from this family is perfringolysin O (PFO), isolated from *Clostridium perfringens.* PFO is a 53 kDa protein which consists of 4 distinct domains designated D1 - D4. The native PFO toxin has been shown to bind to the PM of eukaryotic cells at a threshold of membrane Cholesterol concentration of 35-40 mol% (Ohno-Iwashita et al. 2004; Das et al. 2013). This threshold binding mechanics and fractionation into detergent-insoluble, low-density membrane fractions where raft markers, such as Cholesterol, flotillin and Src family kinases are enriched indicates that PFO binds only a specific subpopulation of Cholesterol-rich domains such as lipid rafts (Ohno-Iwashita et al. 2004). The binding is highly specific to unesterified Cholesterol and is dependent on two amino acid residues in the D4 domain (Farrand et al. 2010), while the other domains coordinate the oligomerization and stabilize the pore. However, this binding was shown to be highly dependent on the membrane phospholipid composition and the resulting interactions Cholesterol has within the membrane leaflets. Paradoxically, the binding threshold of only ~5 mol% Cholesterol was shown for PFO in isolated ER membranes (Sokolov and Radhakrishnan 2010), which was attributed to a likely lower level of phospholipid:Cholesterol complexes in the ER membranes compared to the PM.

While native PFO can be used as a Cholesterol probe in immuno-fluorescence (IF) approaches, its use in living cells is limited due to its lytic activity. Shimada et al. have uncovered the minimal non-lytic Cholesterol-binding truncation o PFO to be the isolated C-terminal domain 4 (D4) (Shimada et al. 2002). This 13 kDa fragment exhibits similar binding dynamics (~40 mol% Cholesterol threshold) as the native PFO but it is unable to oligomerize and induce cell lysis. A recombinant fluorescently tagged D4 was used in super-resolution microscopy approaches to visualize Cholesterol-rich domains on the PM (Mizuno et al. 2011), as well as to stain intracellular membranes (Mitroi et al. 2019) and the cytosolic PM leaflet (Abe et al. 2012) via transfection.

Efforts to decrease the Cholesterol binding threshold have resulted in multiple useful mutants that can detect Cholesterol over a wide range of concentrations: ~20-30 mol% for D4H, ~10 mol% D434A/A463W, and less than 1% for both D4-YDA and D4-QYDA (Liu et al. 2017). Liu and colleagues reported on using a panel of such probes to simultaneously stain the inner and outer leaflets of the PM by microinjection into the cell cytoplasm (Liu et al. 2017), and reported a large enrichment of the outer leaflet in comparison to the cytoplasmic leaflet. However, those claims were contested and it is currently unclear whether D4 probes coupled to solvatochromic dyes such as acrylodan can be used to accurately compare relative Cholesterol content of the leaflets (Courtney et al. 2018). An important consideration when using lipid probes such as D4 in live cells is the potentially disruptive effect of binding and therefore sequestering a large pool of cellular cholesterol, making it chemically unavailable and altering its mobility. Such effects are not fully understood, and have a high potential to alter cellular functions on multiple levels. Nevertheless, these well-characterized probes remain a valuable asset for native Cholesterol domain visualization at high spatial resolution when used for outer PM leaflet labeling.

1.5.2.2. Sphingomyelin-binding toxins

Besides bacteria, various other organisms evolved their own versions of pore-forming toxins. One such example is *Eisinia foetida*, which secretes a 33 kDa single-chain peptide toxin called Lysenin (Lys) into its coelomic fluid which is believed to confer resistance to parasites. Lys belongs to the aerolysin superfamily of proteins, due to its structural similarity and mechanism of action with the aerolysin toxin of the *Aeromonas* species. It is structured into two domains, the lipid recognition domain at the C-terminus that specifically recognizes SM (Yamaji et al. 1998), and the pore-forming module at its N-terminus responsible for oligomerization and pore formation (Colibus et al. 2012). From isothermal titration calorimetry (ITC) experiments it was estimated that Lys binds up to 5 molecules of SM in solution which can be altered to up to 9 molecules in the presence of glycolipids (Ishitsuka et al. 2004). Ishitsuka and colleagues discovered that Lys binding is somewhat inhibited when high proportion of glycolipids such as galactosyl ceramide (GalCer) or short chain PC species were present in SM containing lipid monolayers (Ishitsuka et al. 2004) while the addition of Cholesterol did not significantly change its binding affinity. Additionally, they observed that Lys preferentially binds to SM-rich ordered phases. Colibus and colleagues determined that Lys recognizes the phosphocholine head-group of SM

but also sequesters one of the acyl-chains in the long groove of the pore forming module (PFM), which might aid in the pore formation process (Colibus et al. 2012).

In order to reduce the toxicity of the probe, Kiyokawa et al. generated a N-terminally truncated Lys derivative containing amino acids 161-297 of the native Lys. This non-toxic Lys (NT-Lys) demonstrated the same SM specificity but was unable to oligomerize and induce pore formation, therefore making it suitable for live-cell applications (Kiyokawa et al. 2005). Equinatoxin II (EqtII) was also shown to bind to SM specifically but not to the same SM pool as Lys and its binding was not inhibited by glycolipids (Makino et al. 2015). Atomic force microscopy revealed that EqtII preferentially binds to more disordered domains where SM is dispersed while Lys binds to clustered SM (Makino et al. 2015). Simultaneous labeling by EqtII and NT-Lys revealed that SM segregates into at least three different pools: those stained only by EqtII, only stained by Lys and those that were stained by both (Yachi et al. 2012). Finally, by the use of ostreolysin A, a toxin that specifically binds Cholesterol-sequestered SM, it was shown that such domains remain distinct of those bound by Lys (clustered SM), EqtII (dispersed SM) and D4 (Cholesterol) suggesting a vast heterogeneity in SM enriched domains (Skočaj et al. 2014).

1.5.3. Synthetic lipid analogs

1.5.3.1. Fluorophore-conjugated lipids

An alternative method to observe native cellular lipids is to feed synthetic lipid analogues which are either already labeled or can be labeled after cellular incorporation and distribute to regions of their native counterpart. One of the widely used sterol analogs is BODIPY coupled to Cholesterol (BODIPY-Cholesterol) (**Figure 5 A**). The high brightness and photostability of this probe made it useful for many microscopy applications. BODIPY-Cholesterol incorporates into model membranes (Shaw et al. 2006; Solanko et al. 2013) and has similar properties as Cholesterol in living cells (Hölttä-Vuori et al. 2008). It is taken up by the cells and transported into the endocytic vesicles (Wüstner et al. 2011) however its intracellular pathways differ from native Cholesterol in several ways. It is less prone to esterification (Hölttä-Vuori et al. 2008) and it does not readily segregate into lysosomes in an NPC disease model – an illness known for lysosomal Cholesterol accumulation (Sezgin et al. 2016). Additionally, some sterol transporters such as STARD4 cannot bind to BODIPY-Cholesterol (Wüstner and Solanko 2015). In addition, this probe has performed poorly in STED experiments, where high laser powers needed to be used and only low resolution images could be achieved

(Sezgin et al. 2016; Solanko et al. 2013). Many of these effects are attributable to the properties of the large fluorescent BODIPY moiety and have resulted in efforts towards inventing a better, more physiological analogue versions by reducing the size of the label or the point at which the fluorescent molecule is coupled to Cholesterol.

1.5.3.2. Functionalized lipid analogues

Click chemistry has allowed for the generation of minimally modified Cholesterol analogues by introducing only a single alkyne group into the side chain of Cholesterol which can then be functionalized after cellular incorporation or at any downstream step. These modified alkyne cholesterols are readily taken up and metabolized by cells and their distribution could be determined at a subcellular level (Hofmann et al. 2014; Jao et al. 2015). In order to study protein-lipid interactions an additional diazirine functional group was added, which enables photo-crosslinking of these analogues to nearby proteins for interaction studies and more efficient fixation of lipids (**Figure 5 B,C and D**). This photo-activatable Cholesterol (Pac-Cholesterol) was used to identify interaction partners *in vivo* (Charrin et al. 2003; Ohgami et al. 2004; Suchanek et al. 2007). In a proteome-wide study Hulce and colleagues were able to create a Cholesterol interactome map (Hulce et al. 2013), and Hu et al. showed an interaction of the Influenza virus HA and Cholesterol in the PM of cells (Hu et al. 2019). The application of such probes in SRM has not been established however and it poses an interesting new approach to study nanodomain organization on the PM.

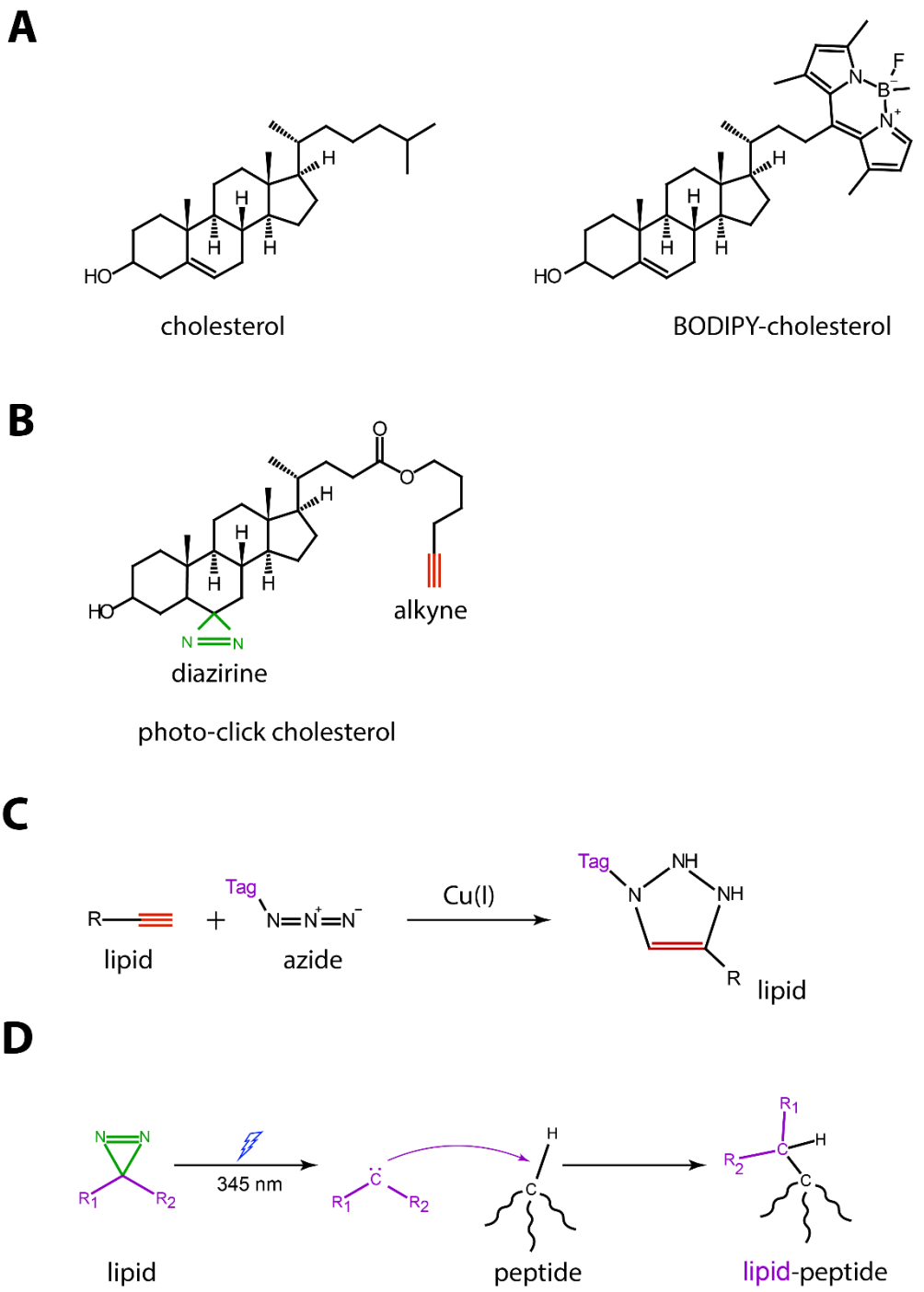

Figure 5. Structure of Cholesterol and its synthetic analogues. (A) Comparison of structures of Cholesterol and BODIPY-Cholesterol. **(B)** Structure of Pac-Cholesterol with diazirine and alkyne groups highlighted. **(C)** Reaction schematic of copper-catalyzed click chemistry reaction between an alkyne lipid and an azide-coupled tagging molecule. **(D)** Reaction schematic of diazirine activation via UV-light and the mode of hydrogen abstraction by the produced radical species resulting in covalent linkage to a nearby peptide.

2. Aim

The aim of this thesis was to visualize native plasma membrane lipids in conjunction with HIV-1 proteins Gag and Env at individual assembly sites in order to gain a better understanding of the distribution of different lipid species at different stages of HIV-1 assembly and budding. The need for this stems from the incompletely understood mechanism of Cholesterol and SM enrichment in the viral membrane obtained from the lipidomic studies and the lack of understanding of protein-lipid interactions during this process. HIV-1 assembly domains span 10-200 nm large structures, while the putative lipid rafts are proposed to be even smaller, which is why this project employed different labelling approaches coupled with STED super-resolution microscopy to resolve the interactions and localization of viral proteins with Cholesterol and SM domains.

Two main approaches were explored in this work. The viability of synthetic Cholesterol analogues for STED imaging of the PM, and the use of recombinant lipid-binding toxin domains for visualization of native cellular Cholesterol and SM. Through the established use of D4 and NT-Lys domains, lipid distribution was characterized in depth at individual HIV-1 assembly sites.

3. Results

3.1. 2-D STED microscopy for visualization of HIV-1 assembly domains

A typical HIV-1 assembly domain can range in size from a few nanometers in the initial stages of budding, comprised of a small number of Gag monomers, up to 120-140 nm in diameter in the late stages, which consists of 2000-3000 Gag monomers (Briggs and Kräusslich 2011; Saha and Saffarian 2020) assembled into an ordered Gag lattice. Therefore, only microscopy techniques that overcome the diffraction limit allow for detection and resolution of assembly sites and associated domains in sufficient detail. In this thesis STED microscopy was used to discern the localization of the HIV-1 structural protein Gag and the surface glycoprotein Env with respect to the PM lipids in the immediate proximity to the assembly site. In such a system, direct comparison of confocal and STED signals can be readily performed, imaging artifacts are easily observed and corrected while sample preparation and staining require simple techniques. One of the downsides of the STED microscopy approach however, is the low z-resolution of approximately 400-500 nm, while the xy resolution reaches 40-70 nm, which was achieved in the system used in this study.

3.2. Assessment of synthetic Cholesterol analogs for STED imaging of PM Cholesterol domains

In order to evaluate whether bifunctional lipid probes could be used to study lipid distribution in the PM on a super-resolution scale and if they sufficiently mimic their natural counterparts, I compared the localization and extractability by methyl-β-cyclodextrin (MβCD) of a commercially available photo-activated Cholesterol (Pac-Cholesterol, Sigma) (**Figure 5 A**) and native cellular Cholesterol stained by Filipin III complex. Cells cultured in media with delipidated serum were fed a 6 µM solution of Pac-Cholesterol for 30 min after which they were either left untreated or further treated with 10 mM MβCD for another 30 min. Subsequently, Pac-Cholesterol was crosslinked by UV illumination for 10 min and cells were fixed using 4% PFA. After washing, Pac-Cholesterol was labeled using a commercial copper-catalyzed click reaction kit after which native cellular Cholesterol was labeled with Filipin III complex. In the sample where Cholesterol extraction was not performed, native cellular Cholesterol staining was present throughout the cytoplasm with enrichments typically at the periphery of the nucleus and in the PM

(**Figure 6 A i and ii**). Pac-Cholesterol staining, on the other hand, looked more homogeneous and intracellular with observable perinuclear enrichments which co-localized to a small degree with the Filipin-stained Cholesterol (**Figure 6 A i**) while the PM staining was almost completely lacking (**Figure 6 A i and iii**). In MβCD-treated cells, native Cholesterol extraction was confirmed by general reduction in Filipin fluorescence signal and loss of PM staining (**Figure 6 B i and ii**). Quantification revealed a reduction of the overall fluorescence signal (Integrated Density) of Filipin by approximately 40% (**Figure 6 C**). The distribution of Pac-Cholesterol did not differ substantially between treated and untreated cells, however, with only a slight decrease of ~15% in total cell fluorescence and no apparent change in the PM signal (**Figure 6 D**).

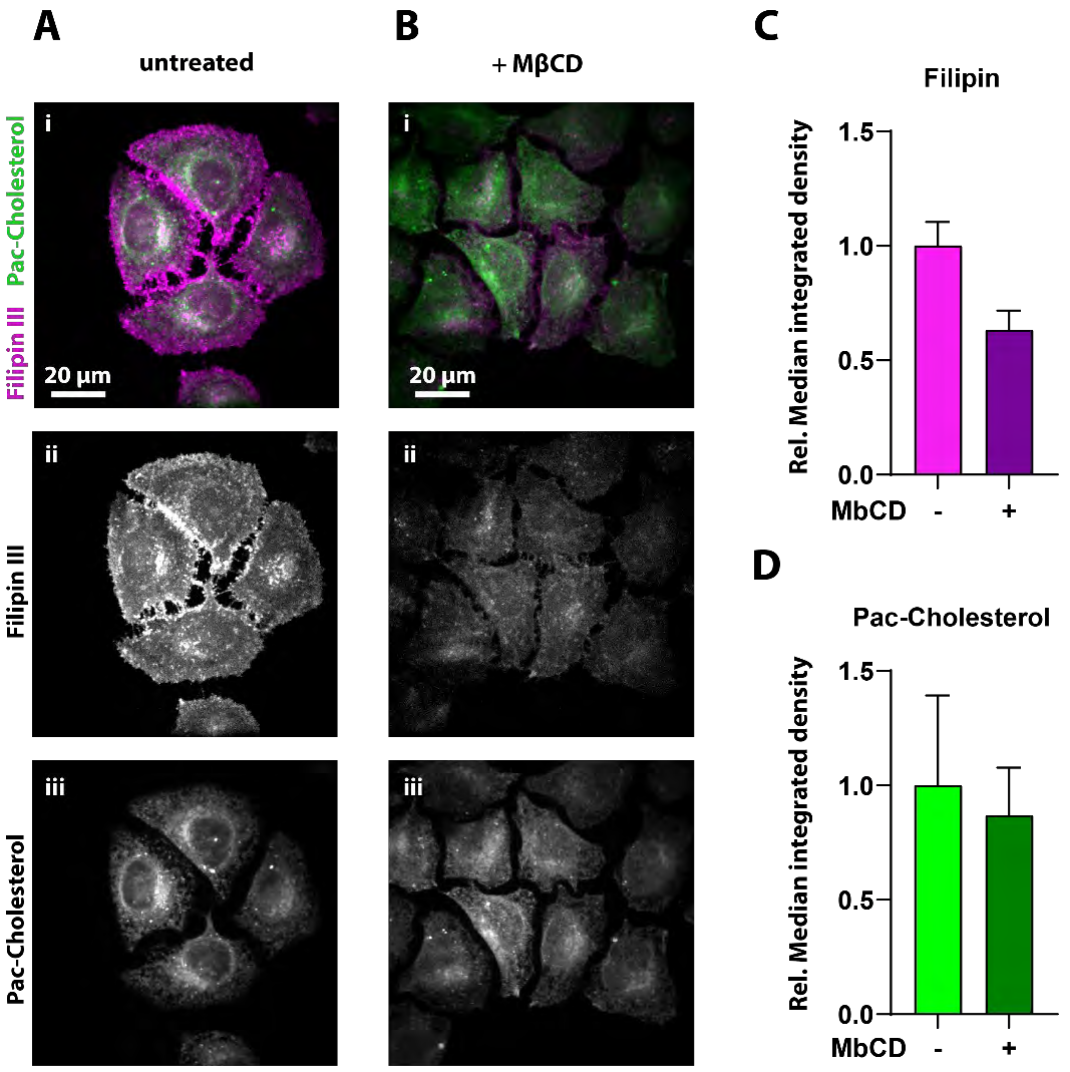

Figure 6. Spatial distribution and propensity to extraction by MβCD of Pac-Cholesterol and native Cholesterol. HeLa cells were incubated with a 6 µM mixture of Pac-Cholesterol in DMEM with delipidated serum for 30 min at 37°C. After washing, cells were either **(A)** left untreated or **(B)** treated with 10 mM MβCD for 30 min at 37°C. Cell were UV-irradiated in PBS for 10 min and fixed with 4% PFA for 15 min at room temperature. Subsequently, Pac-Cholesterol labeling was performed via click reaction with ATTO647N-azide. After washing, native Cholesterol was stained with 0.05 mg/mL Filipin III complex at room temperature and imaged in confocal mode. Maximum intensity projections of the total cell volume are shown for **(A)** untreated and **(B)** MβCD-treated cells. **(C and D)** Shown are relative median integrated densities of total cell volume from 10 individual cells for each condition across 2 individual experiments. Error bars represent 95% confidence intervals of the median.

These results indicated that introducing alkyne and diazirine functional groups into Cholesterol resulted in a change of localization and extraction by MβCD treatment compared to native cellular Cholesterol. Additionally, the very low PM levels of stained Pac-Cholesterol and the intense staining of internal membrane structures resulted in a low signal-to-noise ratio, making high resolution imaging of

the PM in whole cells using STED microscopy a truly difficult task. Attempts to image Pac-Cholesterol by STED microscopy at the PM resulted only in minor improvement in resolution (**Figure 7 A**).

To minimize the effect of the intracellular background signal, Pac-Cholesterol imaging was also attempted in membrane sheets generated by “cell unroofing”, a technique that was successfully applied to study SNARE proteins on the PM (Lang 2003). In short, live cells attached to poly-L-lysine (PLL) coated dishes were subjected to short sonication bursts using a sonicator microtip probe, which resulted in the breakage of the cell while the bottom PM remained attached to the dish. Cells fed with Pac-Cholesterol were unroofed and STED microscopy was performed on the resulting membrane sheets. The sheets were much dimmer than whole cells but could be observed in confocal mode and were bright enough for STED microscopy in some cases. Significant improvement in resolution was achieved in comparison to whole cells and domains as small as 50-100 nm could be observed in line with proposed microdomain size from the literature (**Figure 7 B**).

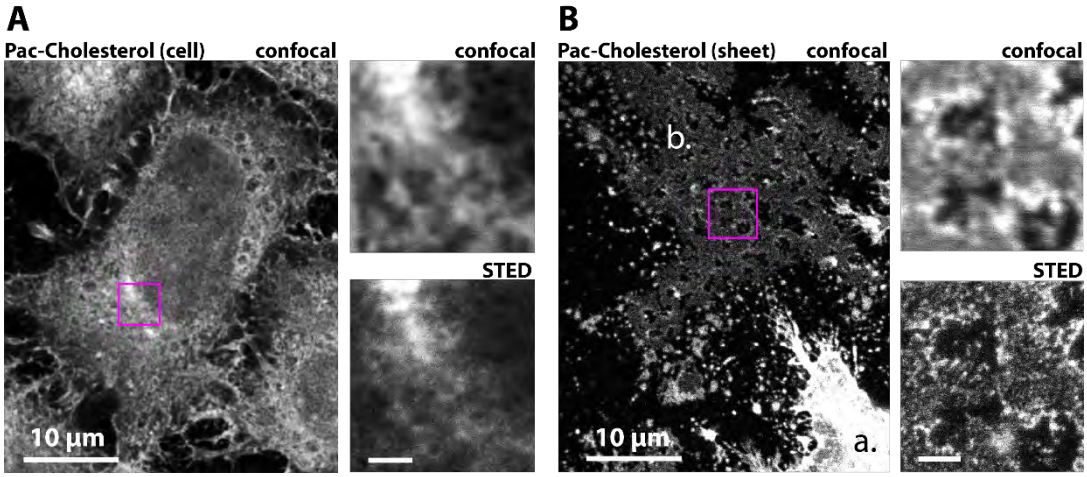

Figure 7. STED microscopy of Pac-Cholesterol in whole cells and membrane sheets. HeLa cells seeded on PLL coated dishes were incubated with a 6 µM mixture of Pac-Cholesterol in DMEM with delipidated serum for 30 min at 37°C. After washing, cells were UV-irradiated in PBS for 10 min and either **(A)** fixed with 4% PFA for 15 min at room temperature or **(B)** unroofed via sonication. Unroofed cells were gently washed with PBS and fixed with 4% PFA for 15 min at room temperature. Subsequently, Pac-Cholesterol labeling was performed via click reaction with ATTO647N-azide. A single slice confocal image of the bottom of a Pac-Cholesterol labeled **(A)** cell or **(B)** membrane sheet, with the purple boxed-in region enlarged in the right panels imaged in confocal and STED microscopy. Scale bar of enlargements is 1 µm. **(a.)** and **(b.)** markings in **(B)** denote a whole cell and a plasma membrane sheet respectively. All STED images were deconvolved using the Richardson-Lucy algorithm as described in Materials and Methods.

Since Pac-Cholesterol could be observed on the isolated PM in higher detail, the effect of MβCD depletion was further investigated and compared between full cells and the PM. The lack of Pac-Cholesterol depletion was recapitulated in full cells (**Figure 8 A**) and served as a control in the experiment while the reduction in Filipin III staining confirmed successful native Cholesterol depletion in whole cells (**Figure 8 B**). PM sheets were of same brightness in both MβCD-treated and untreated samples (**Figure 8 C**), while quantification revealed no difference between the groups (not shown), indicating that in these conditions Pac-Cholesterol does not get noticeably depleted from the PM. Filipin could not be detected in PM sheets in treated nor in untreated samples, due to fast bleaching and a weak fluorescence signal.

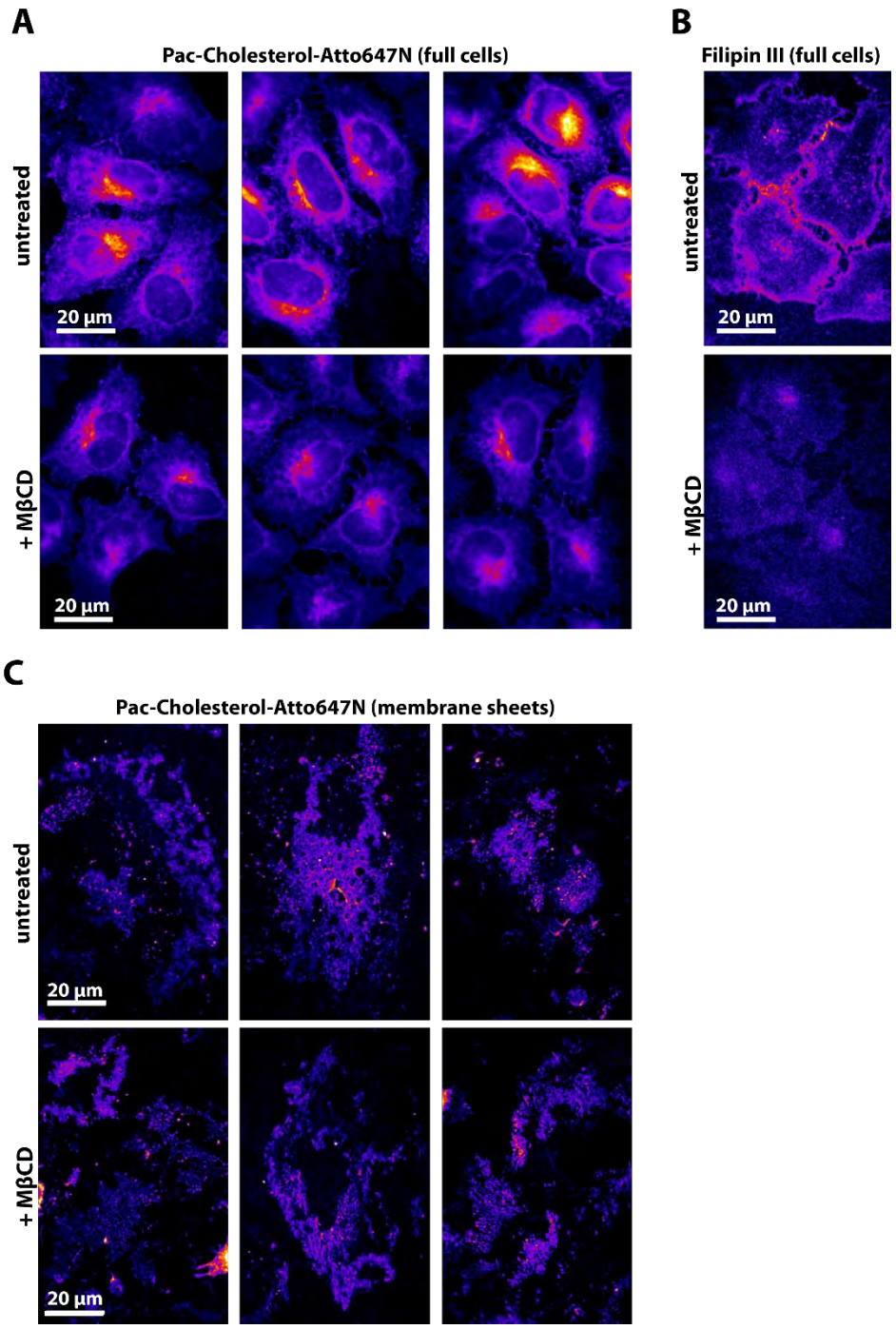

Figure 8. MβCD depletion in whole cells and membrane sheets. HeLa cells seeded on PLL coated dishes were incubated with a 6 µM mixture of Pac-Cholesterol in DMEM with delipidated serum for 30 min at 37°C. After washing, cells were either left untreated or treated with 10 mM MβCD for 30 min at 37°C. Cells were UV-irradiated in PBS for 10 min and **(A and B)** fixed with 4% PFA for 15 min at room temperature, or **(C)** unroofing via sonication was performed and after gentle washing, membrane sheets were fixed with 4% PFA for 15 min at room temperature. Subsequently, Pac-Cholesterol labeling was performed via click reaction with ATTO647N-azide. Lastly, native Cholesterol staining with 0.05 mg/mL Filipin III solution was performed for 2h at room temperature. **(A, B and C)** Confocal images of single slices falsely colored in the "mpl-inferno" lookup table scheme (LUT). Images of treated and untreated cells or membranes were normalized to the same brightness level for signal intensity comparison.

It was previously shown that cholera toxin subunit B (CTxB) binds to the highly saturated ganglioside GM1 that is a component of lipid rafts and therefore colocalizes with Cholesterol. Because of this association, lipid rafts can be clustered via CTxB antibody induced cross-linking. To test if CTxB cross-linking has an effect on Pac-Cholesterol cluster formation, this assay was performed in cells loaded with Pac-Cholesterol which were subsequently unroofed and imaged in STED microscopy. Antibody cross-linking did not seem to have any effect on Pac-Cholesterol distribution and colocalization with CTxB was not observed while no Pac-Cholesterol signal enrichment was observed at CTxB punctae (**Figure 9 A and B**). Additionally, CTxB-Ab complexes localized outside of the stained membrane regions likely adhering to the glass surface (**Figure 9 B**), indicating that the unroofing procedure may introduce artifacts and membrane disruption which may influence the interpretation of results in this system.

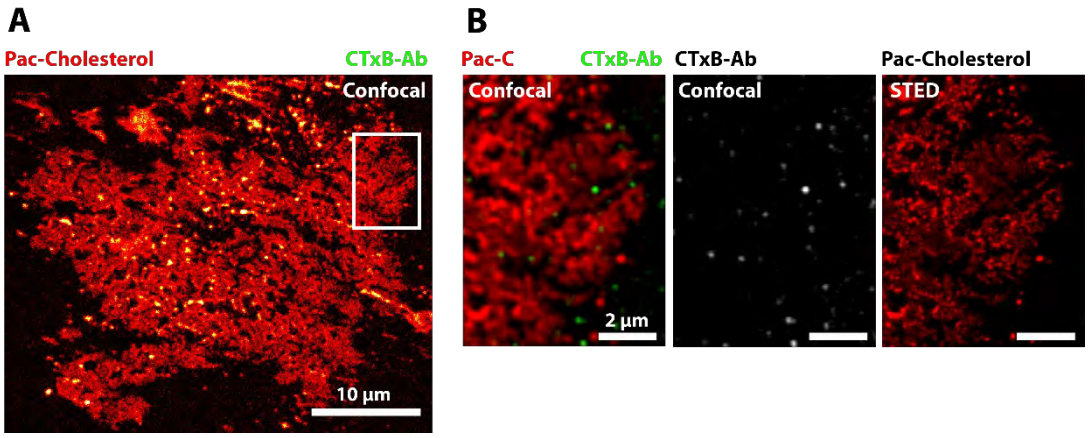

Figure 9. CTxB cross-linking does not induce local enrichments in Pac-Cholesterol staining. HeLa cells seeded on PLL coated dishes were incubated with a 6 µM mixture of Pac-Cholesterol in DMEM with delipidated serum for 30 min at 37°C. Cells were cooled down to 4°C and incubated with 1µg/mL of CTxB-Alexa488 for 10 min. After washing, cells were incubated with a 1:200 dilution of anti-CTxB antibody for 15 min to induce cross-linking, UV-irradiated for 10 min on ice, and unroofed via sonication. Subsequently, cells were fixed in 4% PFA and Pac-Cholesterol was click-labeled with ATTO647N-azide. **(A)** Single slice confocal overview of a membrane sheet with a boxed-in region enlarged in **(B)** imaged in STED mode for Pac-Cholesterol and confocal mode for CTxB-Alexa488.

Despite indications that Pac-Cholesterol does not appropriately mimic the properties of native cellular Cholesterol, its interaction with Gag may still be possible and was hence tested both in intact cells and membrane sheets.

Reliable high resolution STED imaging of HIV-1 Gag at the PM of cells was achieved by transfection of the previously described pCHIV plasmid derivative which encodes all HIV-1 NL4-3 proteins except for Nef and lacks the terminal repeat sequences, rendering it replication incompetent (Lampe et al. 2007). In order to detect Gag by STED microscopy, transfection was done with an equimolar ratio of pCHIV with a plasmid encoding for Gag with a self-labeling CLIP domain (Gag.iCLIP) (Gautier et al. 2008) inserted between the MA and CA domains (pCHIV Gag.iCLIP) (Hanne et al. 2016). Gag.iCLIP can be covalently labeled in live cells with any benzoylcytosine-conjugated (BC) dye, thus making it useful for multicolor STED microscopy. Our group had previously reported anomalous assembly and VLP morphology when Gag had been fused to additional domains (Muller 2004, Eckhardt 2011), and normal assembly and particle morphology were rescued when equimolar amounts of wild-type and tagged Gag-containing plasmids were transfected. Gag in live cells was labeled with ATTO590-BC after which Pac-Cholesterol was supplemented to the culture medium for 30 min. Cells were subsequently UV-irradiated, sonicated to generate membrane sheets, washed in PBS and fixed. Pac-Cholesterol was subsequently labeled with ATTO647N using click chemistry.

Pac-Cholesterol imaging in whole cells did not result in sufficient resolution to give insight into a potential colocalization with Gag due to the previously mentioned intense staining of internal membranes resulting in high out-of-focus background signal (**Figure 10 A and B**). Gag signal was strong and punctate assembly sites could easily be identified at the bottom membrane. Gag sites often clustered into large conglomerates but upon STED imaging, individual domains ~50-120 nm in diameter were discerned (**Figure 10 B)**. Membrane sheets again allowed for a much better resolution of Pac-Cholesterol domains which ranged in size from ~30-200 nm for punctate domains but larger irregularly shaped and elongated domains were also observed. Gag was readily detected on membrane sheets and STED imaging revealed a relatively high level of co-localization with Pac-Cholesterol (**Figure 10 C and D**). This was however not reliably reproducible, with some cells displaying a seemingly random distribution of Gag signals in relation to Pac-Cholesterol. In addition, the Pac-Cholesterol signal was often too weak for STED imaging, resulting in near-background signal.

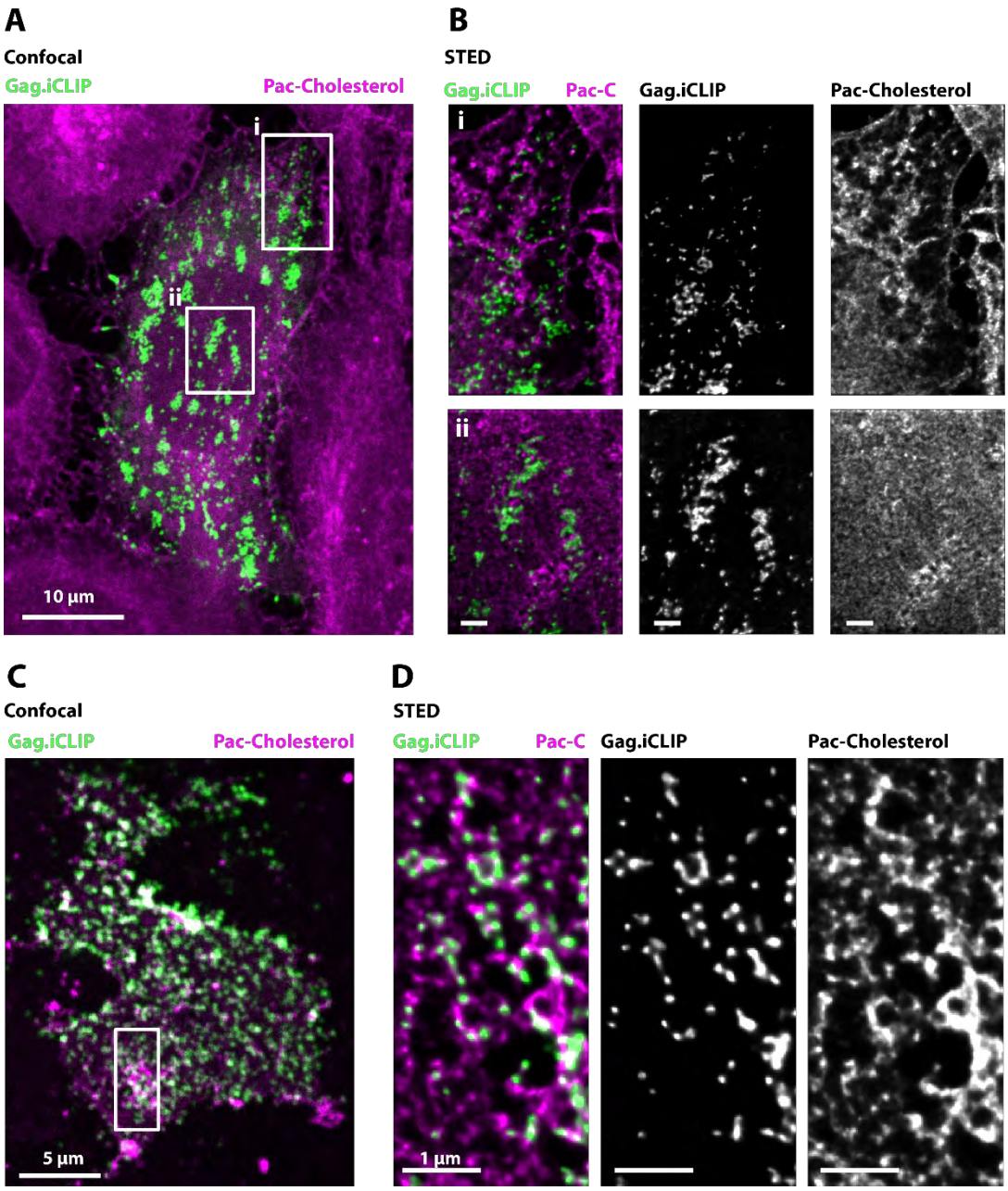

Figure 10. Distribution of Pac-Cholesterol in Gag.iCLIP expressing cells and membrane sheets. HeLa cells seeded on PLL coated dishes were transfected with an equimolar mixture of pCHIV and pCHIV Gag.iCLIP. 14h post transfection, Gag.iCLIP was labeled with 3 µM ATTO590-BC for 45 min at 37°C and washed three times for 15 min in DMEM at 37°C. Cells were incubated in a 6 µM mixture of Pac-Cholesterol in DMEM with delipidated serum for 30 min at 37°C. After washing, cells were UV-irradiated for 10 min in PBS at room temperature and **(A and B)** fixed with 4% PFA for 15 min at room temperature or **(C and D)** unroofing via sonication was performed after which membrane sheets were gently washed in PBS and fixed with 4% PFA for 15 min at room temperature. Subsequently, Pac-Cholesterol labeling was performed via click reaction with ATTO647N-azide and samples were imaged using STED microscopy. **(A)** A single slice confocal overview of the bottom of a transfected cell is shown with two regions of interest imaged in STED mode enlarged in **(B)**. Scale bar is 1 µm. **(C)** A single slice confocal overview of a membrane sheet is shown with a selected region imaged in STED and enlarged in **(D)**. All STED images were deconvolved using the Richardson-Lucy algorithm as described in Materials and Methods.

3.3. Labeling specificity of recombinant lipid probes

3.3.1. Cholesterol labeling specificity of mEGFP.D4

After demonstrating that Pac-Cholesterol does not reliably represent the properties and distribution of native cellular Cholesterol, the focus of this project was shifted towards establishing an alternative labeling technique by utilizing well described recombinant lipid probes. Here, I opted to use the recombinant domain 4 of perfringolysin O (D4), a prototypical Cholesterol-binding toxin secreted by *Clostridium perfringens*, to indirectly visualize native cellular Cholesterol clusters in the outer PM leaflet. D4 was N-terminally fused to a monomeric variant of EGFP (mEGFP) bearing the A206K mutation (Zacharias et al. 2002), to enable fluorescence microscopy and avoid artificial GFP-induced clustering while STED microscopy of D4 was indirectly achieved via a fluorophore-coupled anti-GFP nanobody (GFP Booster ATTO594 or ATTO647N).

Before establishing STED imaging using this probe, the reported mEGFP.D4 specificity towards Cholesterol binding needed to be validated (Ohno-Iwashita et al. 2004; Shimada et al. 2002). HeLa cells were left untreated or were treated with 10 mM MβCD for 30 min to extract PM Cholesterol, after which staining of native Cholesterol domains was performed by incubating cells with the purified mEGFP.D4 at room temperature for 10 min. After washing and fixation, cells were additionally stained with Filipin III, which labels unesterified Cholesterol in the whole cell, as well as with a nuclear dye for cell detection. In confocal microscopy, the PM of MβCD-untreated cells was uniformly covered with small punctate mEGFP.D4 clusters with a clear and strong PM labeling while the internal membrane structures remained unstained and no internalization of the protein was observed (**Figure 11 A**). Filipin III staining was present more uniformly on the PM as well as in the area around the nucleus as was reported before (Wilhelm et al. 2019; Harikumar et al. 2005; Ishitsuka et al. 2011). Additionally, mEGFP.D4 staining did not display cytotoxic effects or alter the cell morphology in any noticeable way.

After MβCD treatment, the PM staining with mEGFP.D4 was nearly undetectable, while Filipin showed strongly reduced PM and largely retained internal staining (**Figure 11 B**). This visual impression was confirmed by quantitation of the mEGFP.D4 (**Figure 11 C**) and Filipin (**Figure 11 D**) signals respectively. The D4 signal was almost completely lost, while overall Filipin staining was only slightly reduced, owing to the retained intracellular signal. Together these results validated that mEGFP.D4, when added from the outside of cells, recognizes Cholesterol and

specifically labels the outer PM leaflet in a Cholesterol-dependent manner. This compound thus appeared to be suitable for establishing a STED-compatible labeling protocol for detection of Cholesterol domains in the context of HIV-1 assembly.

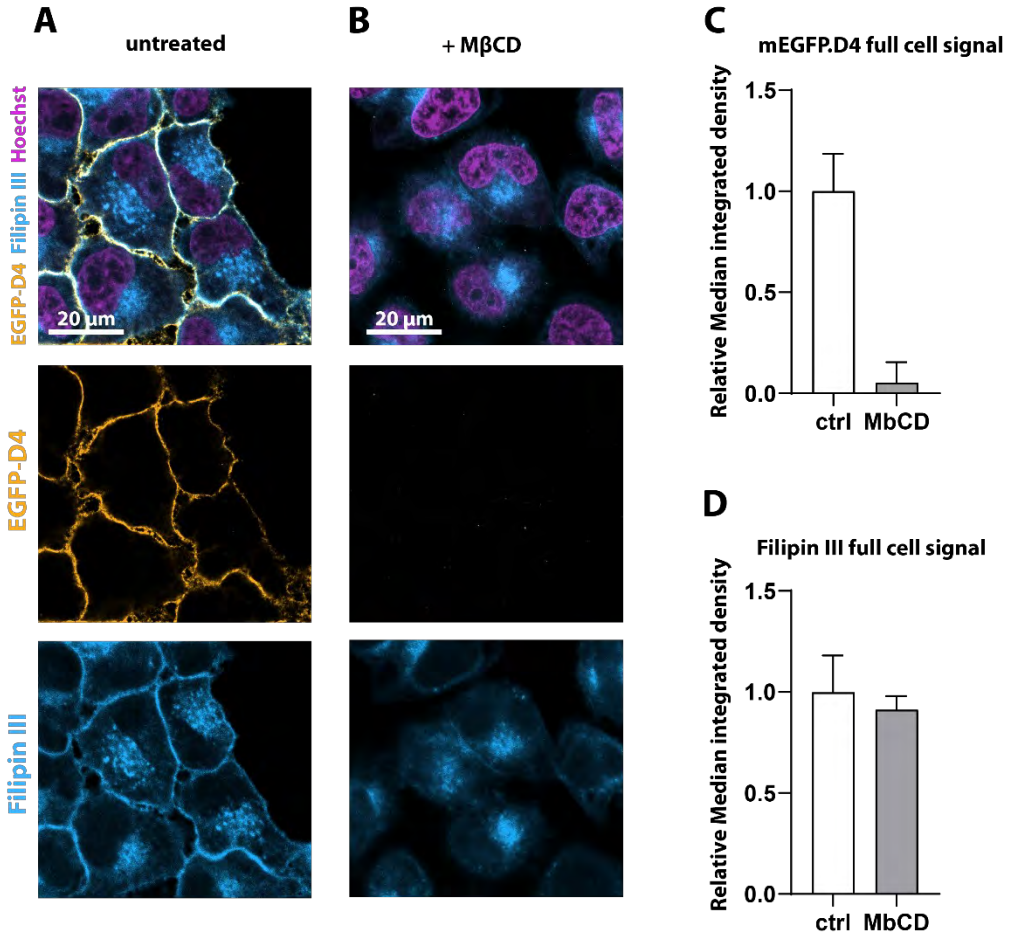

Figure 11. Cholesterol staining specificity of mEGFP-D4. HeLa cells were either left untreated **(A)** or were treated with 10 mM MβCD **(B)** for 30 min at 37°C. PM Cholesterol was stained with mEGFP-D4 for 10 min at room temperature as described in the Methods section **6.8** (page 101), washed and cells were fixed with 4% PFA. Staining of esterified Cholesterol was done with Filipin III and cells were subsequently imaged in confocal mode. Shown are single slice images of the middle section of cells. The median of total cell volume integrated density obtained from sum projections is shown for **(C)** mEGFP-D4 and for **(D)** Filipin from seven untreated and four MβCD-treated cells.

3.3.2. Sphingomyelin labeling specificity of mEGFP.NT-Lys

Another lipid that was reported to be enriched in the viral membrane of HIV-1 is SM. The non-toxic truncation of Lys C-terminally fused to mEGFP (mEGFP.NT-Lys), was chosen for staining of SM domains in this project. The specificity of the purified mEGFP.NT-Lys towards SM was assessed by confocal microscopy in cells enzymatically depleted of SM by sphingomyelinase (SMase) treatment. Purified mEGFP.NT-Lys was supplemented to the medium of live cells,

after which the cells were washed, fixed and subsequently imaged. Untreated cells had a pronounced PM staining that varied in intensity from one cell to another, but was rather uniform within a single cell (**Figure 12 A**). Punctate enrichments could be observed in certain regions of the PM and a low level of internalization was observed. Sphingomyelin depletion via the action of SMase and subsequent staining with mEGFP.NT-Lys revealed a marked decrease in the intensity of the PM staining, while some enrichments remained (**Figure 12 B**). Quantification of total cell NT-Lys fluorescence confirmed the observed depletion (**Figure 12 *C***). This confirmed that mEGFP.NT-Lys specifically binds SM in the outer PM leaflet and appears thus suitable for STED microscopy of SM at Gag assembly sites.

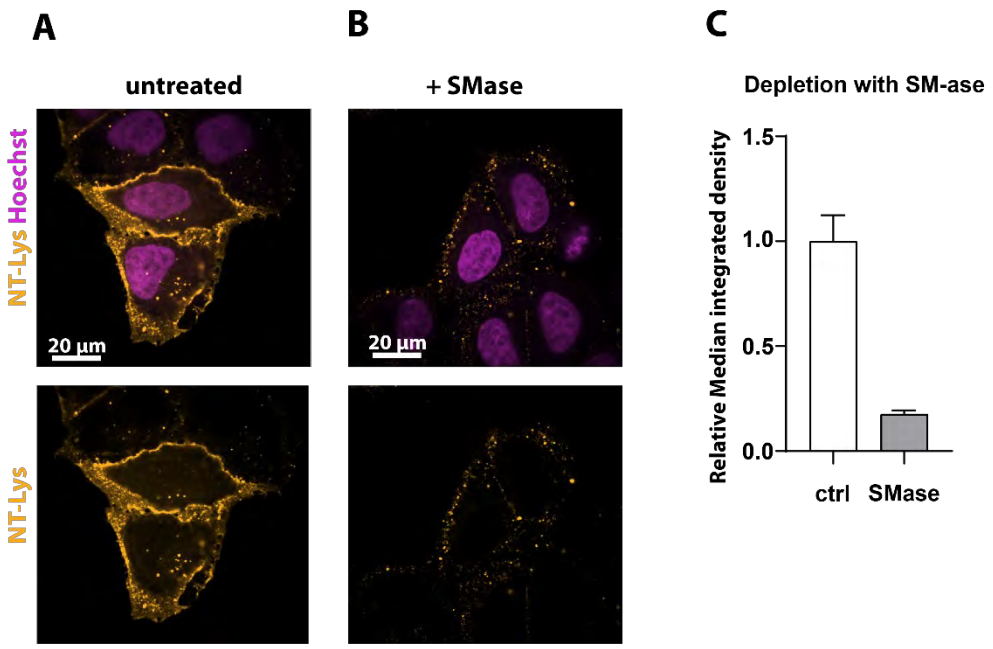

Figure 12. SM labeling specificity of mEGFP.NT-Lys. HeLa cells were either left untreated **(A)** or treated with 2 mg/mL SMase **(B)** for 1h at 37°C. Labeling of native cellular plasma membrane SM was performed with mEGFP.NT-Lys for 10 min at room temperature as described in the Methods section **6.8** (page 101), cells were washed and fixed with 4% PFA. Shown are single slice confocal images of the middle section of cells. **(C)** Median of full cell integrated density obtained from sum projections is shown for mEGFP.NT-Lys from four untreated and six treated cells.

3.4. 2D STED microscopy of HIV-1 assembly sites

Before establishing STED imaging with the tested lipid probes, a detailed study of individual HIV-1 assembly sites in respect to Gag and Env localization was performed in pCHIV transfected cells. As described above, cells were transfected with an equimolar mixture of pCHIV and pCHIV Gag.iCLIP, Gag was labeled in live cells using a cell permeable dye, ATTO590-BC and cells were fixed. Env glycoprotein was detected by indirect immunofluorescence with a human anti-Env primary IgG antibody (2G12) and a dye-conjugated (Abberior STAR RED) secondary Fab fragment (goat anti-human).

Imaging of pCHIV-transfected cells in STED mode was performed on the apical membrane to detect nascent assembly sites and avoid unintended interference of cell-released VLPs trapped between the cell membrane and the glass bottom. Using this approach, I could observe the previously described punctate Gag domains scattered throughout the PM of transfected cells (Muranyi et al. 2013; Lehmann et al. 2011; Mücksch et al. 2017; Muecksch et al. 2024). At 14h post-transfection, cell PM was dotted with a large number of individual Gag assembly domains as well as with areas where multiple Gag assemblies appeared to be grouped into larger clusters, with on average 5-20 individual Gag domains **(Figure 13 A and B)**. Env glycoprotein was detected in smaller clusters predominantly at the periphery of Gag domains, often constructing an irregular ring-like domain that encircled the entire Gag domain, while the center of the Gag domain yielded a much weaker Env signal **(Figure 13 B and C)**. Additionally, smaller punctate Env signals were observed both in association with Gag and, somewhat rarely, in areas with no detectable Gag signal. These results were in line with previous reports of our laboratory (Mücksch 2017; Mücksch et al. 2017; Muranyi et al. 2013) and consistent with our understanding of the HIV-1 assembly site (Lerner et al. 2022; Freed 2015; Sundquist and Kräusslich 2012).

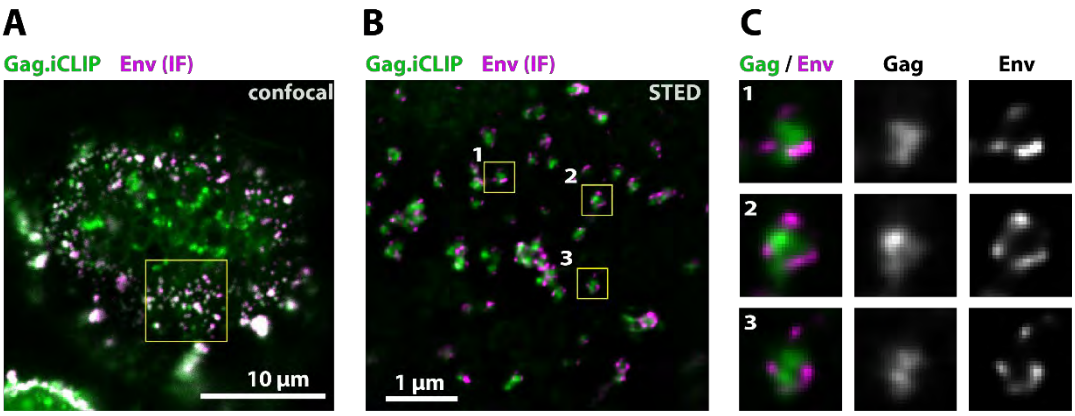

Figure 13. Localization of Gag and Env within HIV-1 assembly domains. HeLa cells were transfected with an equimolar pCHIV/pCHIV Gag.iCLIP mixture. 14h post transfection, Gag.iCLIP was labeled with 3 µM ATTO590-BC for 45 min and after three 15 min washing steps, cells were fixed in 4% PFA. Env glycoprotein was labeled by indirect immunofluorescence using human anti-gp120 (2G12) primary IgG and a STAR RED-coupled secondary goat anti-human Fab fragment. **(A)** A confocal overview of the apical membrane of a transfected cell was selected from which a region of interest was imaged in **(B)** STED mode. Individual representative HIV-1 assembly domains are shown enlarged in **(C)** highlighting the spatial distribution of punctate Gag and extended ring-shaped Env domains. Size of enlargements is 400 x 400 nm. All STED images were deconvolved using a Richardson-Lucy algorithm as described in the Methods section **6.13** (page 103).

3.4.1. Radial fluorescence intensity profile of HIV-1 assembly sites

In order to spatially characterize these assembly domains in a quantitative and unbiased manner, I adapted a Python-based script, referred to as “radial profile analysis” in further text, that determines mean fluorescence intensity of each channel, as a function of the distance from the centroid of the Gag domain (**Figure 14 A and B**), described in detail in section **6.14** (page 103). In brief, after automatic segmentation based on the Gag domain signal and manual correction to include only individual domains within the plane of focus separated from large clusters, the centroid (intersection of major and minor axes) of each Gag domain segmentation is determined. The center pixel area comprising of 2-3 pixels (distance from Gag center: 0 nm) is taken as the first area from which mean fluorescence intensity of both Gag and D4 channels is calculated. The average fluorescence from the 1-pixel-wide ring surrounding the previous area is then calculated, repeating the script until the distance of 12 pixels from the center of the Gag domain is reached (distance from Gag: 165 nm).

This method in essence results in the same output as an average of multiple line profiles, each starting at the centroid of the Gag domain and radiating outwards

to the domain periphery with the length of 165 nm in each direction, taking into account that the pixel size of 15 nm was defined during STED imaging. While this method gives a more accurate depiction of a fluorescence intensity profile of radially symmetrical structures, such as punctate Gag domains and fully formed Env ring domains, on account of being an average of all pixels equidistant from the center of the domain – it cannot be applied on asymmetrical structures to accurately determine their distribution due to signal averaging. A Gag domain with a small punctate Env domain at its periphery would therefore be misrepresented as having no Env signal due to signal averaging with the near-zero pixel values detected in the majority of the pixel ring area. Hence, only Gag domains that were fully encircled by an Env domain were manually selected for this radial profile analysis.

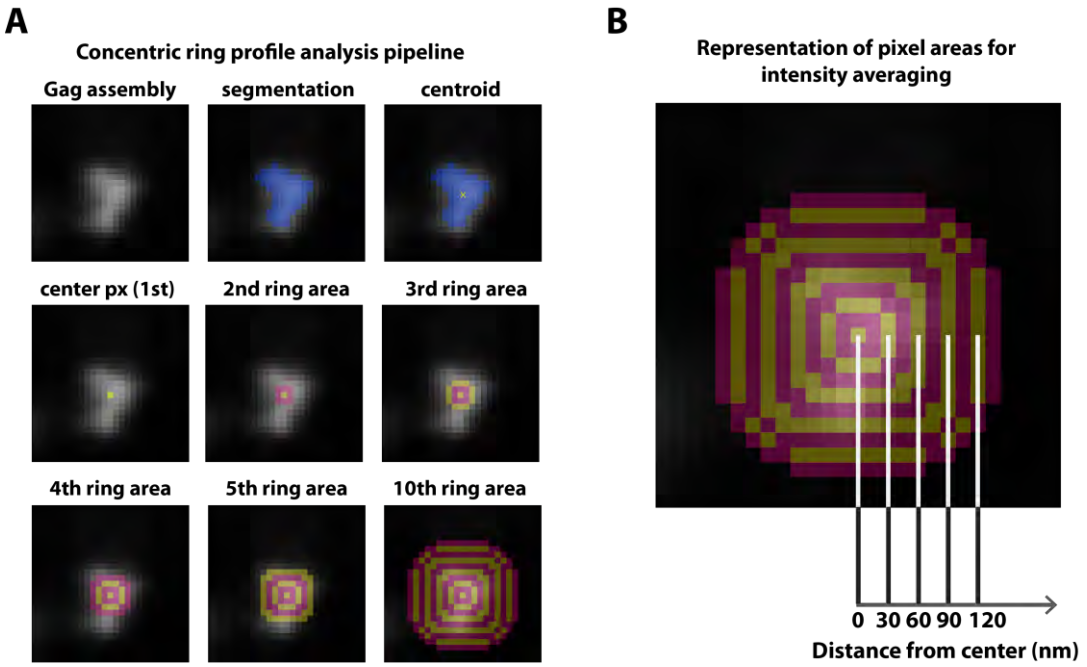

Figure 14. Radial fluorescence intensity profile - Python script pipeline. **(A)** Segmentation, centroid determination and ring areas taken for average intensity calculation at Gag assemblies. Automatic segmentation is performed according to Otsu's method. Starting with the central pixel at the Gag centroid and radiating outwards, pixels equidistant from the center are averaged (alternating yellow and red colors denote separate pixel areas from which a single average with 95% confidence interval is calculated for the given distance from the center). **(B)** Enlarged view of pixel areas that are averaged to calculate the radial profile on a single Gag domain. The center of the bud demarcated with 0 and each subsequent pixel ring increasing by 15 nm increments (pixel size) is shown. The original script was developed by Thorsten G. Müller and Svenja Nopper, which was then adapted for use in STED microscopy for this project.

Utilizing this script on the specific subset of Gag domains fully encircled by Env (**Figure 15 A**), a median radius of Gag domains was determined to be 120 nm from

the full width at half maximum (FWHM) of Gag signal measuring 60 nm, while the peak of the Env domain was positioned at 60 nm from the centroid and thus in the periphery of the Gag domain (**Figure 15 B**).

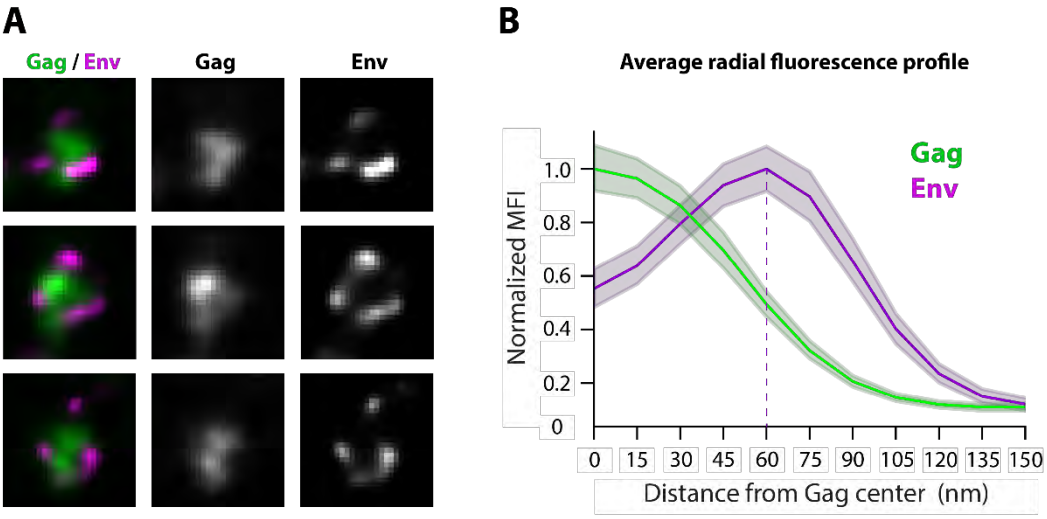

Figure 15. Radial intensity profile of Gag and Env in representative HIV-1 assembly domains. (A) STED cutouts of representative HIV-1 assembly domains featuring a Gag domain fully encircled by the Env domain selected for the analysis in the radial profile intensity averaging. **(B)** Radial intensity profile of Gag and Env from the respective assembly domains showcasing the average distance of the Env signal peak (60 nm, dotted line) from the centroid of Gag (0 nm). MFI was normalized to the maximum mean of N=167 assemblies from three cells from two independent experiments. The 95% confidence interval of the mean is shown as the shaded area of the respective color line.

3.5. STED microscopy of mEGFP.D4 in untransfected cells

To explore the distribution and appearance of Cholesterol domains in super-resolution without the influence of viral proteins, STED microscopy of untransfected cells labeled with mEGFP.D4 was performed. Cultured cells were stained with mEGFP.D4 for 10 min at room temperature. After washing and PFA fixation, the staining with anti-GFP nanobody directly coupled to ATTO647N (GFP Booster) was used to enable imaging of mEGFP.D4 in super-resolution since EGFP itself cannot be efficiently depleted by the 775 nm laser line installed in the used STED system. In confocal view, the cell PM was non-uniformly stained in a punctate manner with higher intensity staining often observed in cellular protrusions and at cell borders (**Figure 16 A**). General variability in staining intensity was present between sections of the whole cell, such that large portions of the PM had higher density of punctate domains then others. STED imaging of selected apical PM sections revealed mostly individual punctate domains between 40-250 nm in diameter (FWHM) and less

intense, diffuse larger domains (**Figure 16 B**). Clusters of multiple smaller domains were also often observed. Average distance to the nearest neighbor of punctate domains varied from 200 nm to 1.5 µm depending on the cell and selected region within the cell PM. Large conglomerates of domains were observed in cell protrusions and were in most cases inefficiently depleted by the STED laser offering only marginal improvements in resolution.

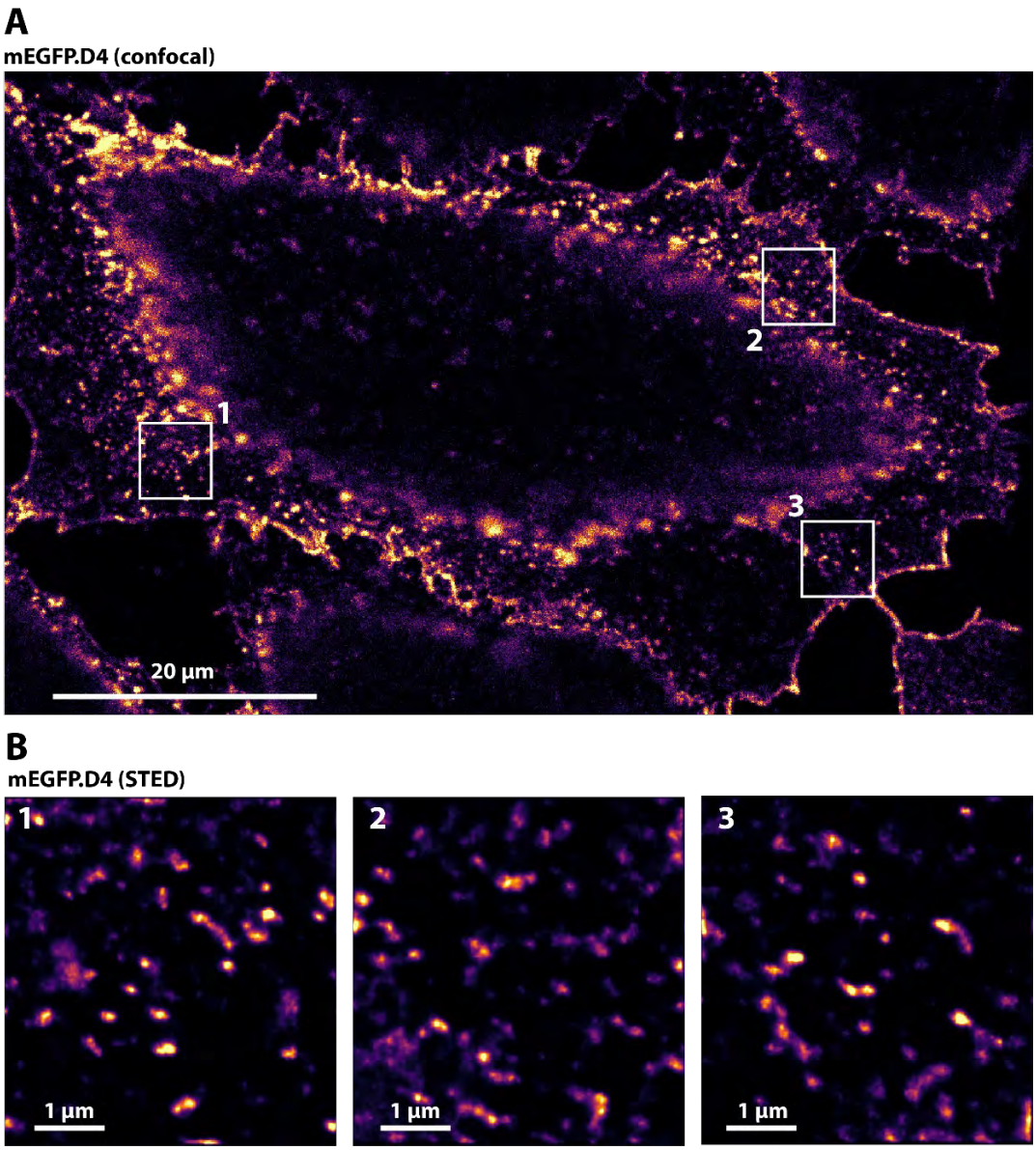

Figure 16. STED microscopy of mEGFP.D4 stained HeLa cells. HeLa cells were stained with mEGFP.D4 for 10 min at room temperature and subsequently washed and fixed with 4% PFA. To enable STED microscopy of mEGFP.D4, cells were labeled with GFP Booster ATTO647N and subsequently imaged at the apical PM. A single z-slice of a HeLa cell imaged in confocal mode is shown in **(A)**. White boxes demarcate three PM segments of similar mean intensity which were imaged in STED mode and shown enlarged in **(B)** after deconvolution with the Richardson-Lucy algorithm as described in the Methods section. The images were pseudo-colored using the “mpl-inferno” lookup table in Fiji software.

3.6. STED microscopy of lipids at HIV-1 assembly domains

After establishing STED imaging of the two relevant HIV-1 proteins, Gag and Env, and confirming the specificity of D4 and NT-Lys lipid probes and exploring the distribution and appearance of Cholesterol domains in untransfected cells, I next set out to utilize these Cholesterol- and SM-specific probes in combination with either Gag or Env in two-color 2D STED microscopy. Live transfected cells were first stained for Gag using a cell-permeable, BC-linked ATTO590 dye. After washing, cells were stained with mEGFP.D4 as described before and in Materials and Methods. Initial observation of VLP-producing cells taken in STED mode revealed a marked colocalization of D4-stained clusters with HIV-1 Gag (**Figure 17 A**). Inspection of a larger set of individual assembly domains revealed that Gag is predominantly associated with smaller Cholesterol clusters associated to its periphery, while only a small number of Gag domains had no detectable D4 signal in its proximity. Further inspection of individual Gag assemblies revealed that smaller punctate Cholesterol domains sometimes fully encircle the Gag domain to form a larger, ring-like domain at the periphery of the Gag domain, reminiscent in relative position to Gag and general appearance to the previously observed Env ring domains (**Figure 17 B**). Radial profile analysis of these Gag domains fully encircled by smaller Cholesterol domains indicated that the mEGFP.D4 signal is on average highest at around 45 nm from the Gag centroid (**Figure 17 C**), somewhat closer to the center than the peak of Env domains (60 nm, **Figure 15 B**).

A very similar observation was made when SM was imaged using mEGFP.NT-Lys in a sample prepared the same way as described above for D4. Briefly, after staining Gag using BC-ATTO590 in pCHIV/pCHIV Gag.iCLIP transfected cells, and staining with mEGFP.NT-Lys, washing and fixation were performed as well as the subsequent labeling of EGFP with GFP Booster ATTO647N nanobody. NT-Lys-stained domains colocalized closely with Gag domains (**Figure 17 D**) in a similar manner that was observed for Cholesterol. In a subset of Gag domains, smaller NT-Lys stained clusters encircled the entire Gag domain (**Figure 17 E**) as was observed for Cholesterol, with the peak of the signal located between 45 and 60 nm, determined by the radial intensity profile analysis (**Figure 17 F**). Taken together, these data indicate that lipid domains rich in Cholesterol and SM associate with HIV-1 assembly sites at the periphery of the Gag lattice where they combine into larger, ring shaped domains, which sometimes fully encircle the punctate Gag assembly sites. As lipid domains of that shape were not observed in untransfected

cells (**Figure 16**), it follows that HIV-1 budding specifically induces Cholesterol/SM-rich lipid domain reorganization and recruitment.

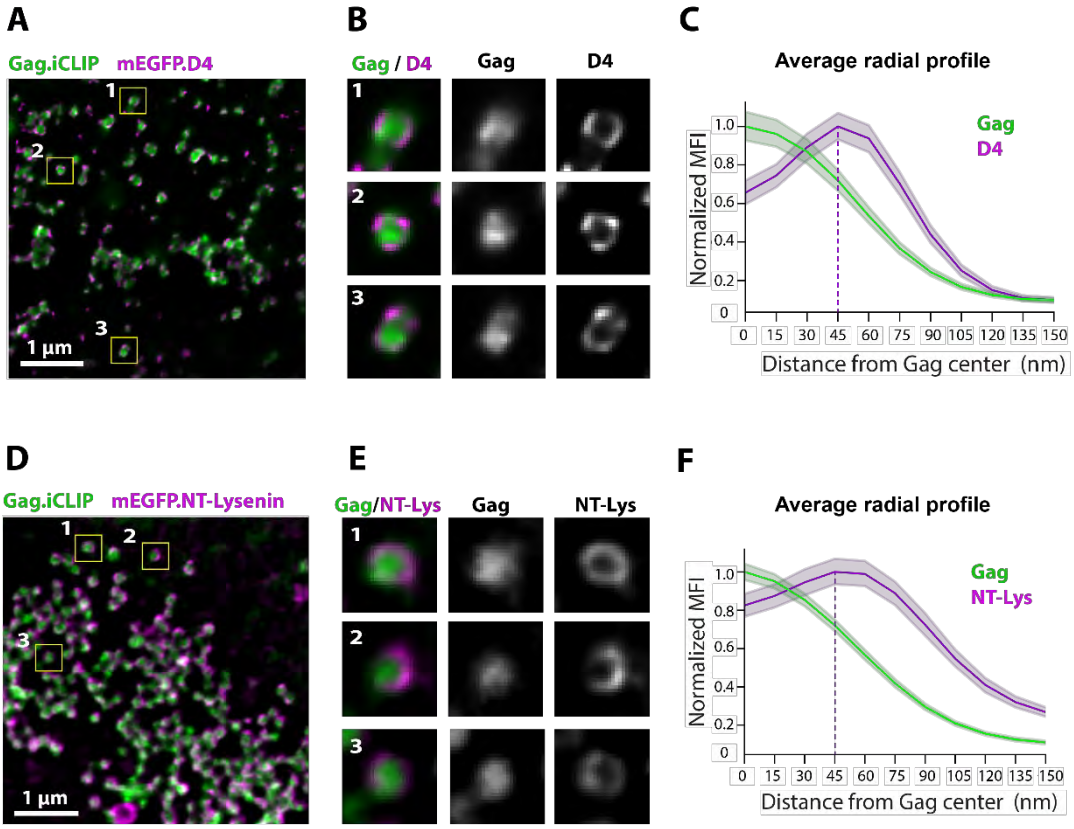

Figure 17. Cholesterol- and SM-rich domains encircle Gag during HIV-1 assembly. HeLa cells were transfected with an equimolar mixture of pCHIV and pCHIV Gag.iCLIP. At 14h post transfection, Gag was labeled with ATTO590-BC, Cholesterol with mEGFP.D4 **(A, B, C)** or SM with mEGFP.NT-Lys **(D, E, F)**. After PFA fixation, cells were labeled with ATTO647N-coupled anti-GFP nanobody to enable STED imaging of mEGFP.D4/NT-Lys. A segment of the apical membrane imaged in dual-color 2D STED mode is shown in **(A)** for D4 and **(D)** for NT-Lys. Boxed regions containing representative Gag domains fully encircled by a lipid domain are shown enlarged in **(B)** for D4 and **(E)** for NT-Lys. The respective average radial profile analysis for D4 **(C)** and NT-Lys stained **(F)**, fully encircled Gag domains was obtained from N=176 and N=205 assemblies across three cells and two individual experiments performed as described in the Methods section. MFI was normalized to the maximum mean of all the assemblies in a set. Shaded areas depict the 95% confidence interval of the mean.

In addition to observing D4-stained Cholesterol domains colocalizing with Gag at assembly domains in the PM of transfected cells, detached particles near the cell border positive for Gag could also be stained with D4 (**Figure 18 A - C**). The Gag and D4 signals were largely overlapping in this case, with the D4 signal being somewhat less defined and exhibiting a slightly larger diameter but no ring-like appearance (**Figure 18 C**).

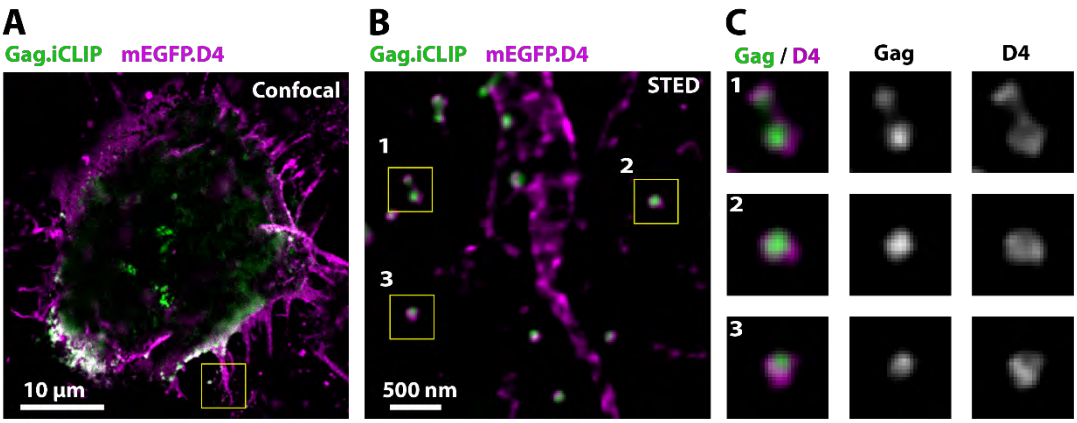

Figure 18. Detached VLPs can be stained with mEGFP.D4. HeLa cells were transfected with an equimolar mixture of pCHIV and pCHIV Gag.iCLIP. At 14h post transfection, Gag.iCLIP was labeled with ATTO590-BC and Cholesterol domains with mEGFP-D4 after which cells were washed and fixed in 4% PFA at room temperature. **(A)** Confocal overview of a transfected cell with the yellow boxed-in region outlining the space around a cell filopodia where detached particles were observed. **(B)** Enlarged boxed-in region from panel **(A)** imaged in STED mode with three representative VLP particles enlarged in **(C)**. Enlargement dimensions are 400 x 400 nm.

3.7. Gag oligomerization is sufficient for recruitment and coalescence of Cholesterol and SM domains

Gag is the main orchestrator of the HIV-1 assembly and therefore could be sufficient to induce the recruitment of the lipids to the assembly site on its own while Env may interact with the lipid domains independently of Gag. By transfecting Gag or Env in isolation, without other HIV-1 proteins, the next experiments aimed to determine their individual effect on Cholesterol and SM domain distribution.

To this end a CMV-driven, codon-optimized, SNAP-tagged synthetic Gag^{WT} (synGag.iSNAP) was used in an equimolar transfection with an untagged synGag plasmid to avoid budding artifacts and VLP morphology defects previously observed in tagged-only transfection systems. Double transfection with these plasmids results in the expression of tagged and untagged Gag without other HIV-1 proteins, allowing for an isolated experiment of Gag's influence on lipid behavior. At 14h post-transfection, Gag.iSNAP was stained with ATTO590-BG while mEGFP.D4/NT-Lys staining and preparation for STED microscopy was done as previously described and detailed in the Methods section.

Using STED nanoscopy, individual punctate synGag sites that sometimes clustered into larger groups were detected across the apical membrane of transfected cells **(Figure 19 A and B)**. synGag signals were similar in size, shape

and signal intensity compared to the Gag^{WT} sites observed in the pCHIV transfection. These sites were very often associated with both mEGFP.D4 and mEGFP.NT-Lys signals which frequently formed the previously described ring-shaped domain at the borders of synGag sites (**Figure 19 C and D** respectively), however punctate domains as well as synGag-free D4 and NT-Lys signals were readily observed.

The average radius of the synGag signals associated with full lipid rings was between 50-70 nm (FWHM) while the peak of the lipid probe signal measured at these domains was on average between 45 and 60 nm for Cholesterol (**Figure 19 E**) and 60 nm for SM (**Figure 19 F**) – comparable to the values observed for the full, pCHIV transfection system. Together, this revealed that Gag alone is sufficient to induce Cholesterol- and SM-rich lipid ring-like structures in the periphery of Gag assembly sites and that this phenotype was indistinguishable from pCHIV-transfected cells expressing all HIV-1 proteins except Nef.

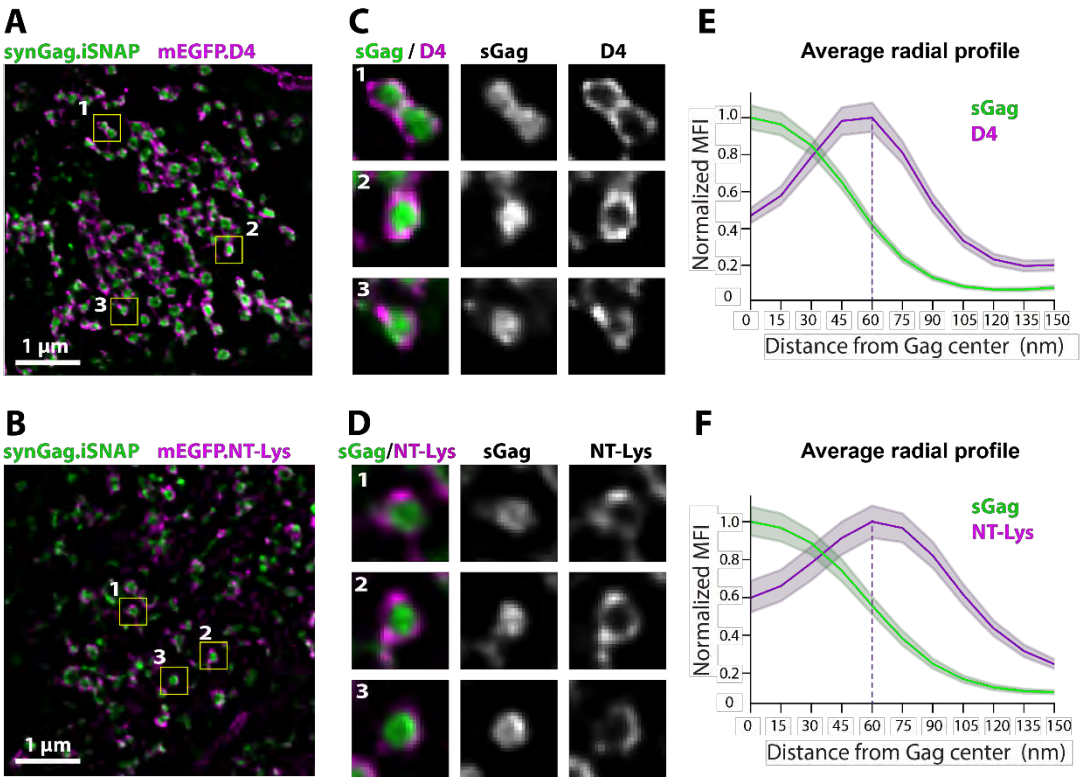

Figure 19. Gag oligomerization is sufficient to induce lipid recruitment and ring formation. HeLa cells were transfected with an equimolar mixture of synGag:synGag.iSNAP carrying plasmids. At 14h post-transfection, synGag.iSNAP was labeled with ATTO590-BG and Cholesterol with mEGFP.D4 **(A, C, E)** or SM with mEGFP.NT-Lys **(B, D, F)**. After PFA fixation, cells were labeled with ATTO647N-coupled anti-GFP nanobody to enable STED microscopy of mEGFP.D4/NT-Lys. A segment of the apical membrane imaged in dual-color 2D STED mode is shown in **(A)** for D4 and **(B)** for NT-Lys. Boxed regions containing representative synGag domains fully encircled by a lipid domain are shown enlarged in **(C)** for D4 and **(D)** for NT-Lys. The respective average radial profile analysis for D4 **(E)** and NT-Lys stained **(F),** fully encircled synGag domains was obtained from N=142 and N=220 assemblies across three cells and two individual experiments respectively, performed as described in the Methods section. MFI was normalized to the maximum mean of all the assemblies in the set. Shaded areas depict the 95% confidence interval of the mean. Plasmids containing synGag and synGag.iSNAP were generated by Moritz Hacke who also performed transfections and participated in imaging of these domains.

3.8. Env localizes to the periphery of Cholesterol- and SM-rich domains.

In order to explore the potential effects of Env expression and PM incorporation on Cholesterol domain distribution without the influence of other viral proteins, I employed mEGFP.D4 labeling in cells transfected with a pCGGAS plasmid encoding the full NL4-3 Env^{WT} under a chicken β-actin promoter and CMV enhancer (Bozek et al. 2012). After transfection, cells were labeled with mEGFP.D4 as described before and subsequently fixed in PFA. Env was labeled using a primary

anti-gp120 IgG (2G12) and a secondary anti-human Fab conjugated to Abberior STAR RED.

STED microscopy of apical membrane segments revealed predominantly individual punctate Env domains 70-150 nm in diameter of a mostly random and uniform PM distribution, however elongated clusters composed of multiple smaller domains were also observed (**Figure 20**). Cholesterol domains were somewhat larger then Env, ranging from 50-400 nm, often in clusters however diffuse irregular shapes of lesser intensity were also observed. The signal overlap between Env and mEGFP.D4 was low, rather Env signals seemed to be excluded from mEGFP.D4 stained domains. Interestingly however, Env domains were often situated on the borders of Cholesterol domains (**Figure 20**; see yellow arrows in enlargements **A** and **B**) and were rarely observed in isolation, without an associated mEGFP.D4 signal. No observable change in Cholesterol domain shape, size, intensity or overall membrane distribution was revealed in cells expressing only Env in comparison to untransfected cells (**Figure 16**).

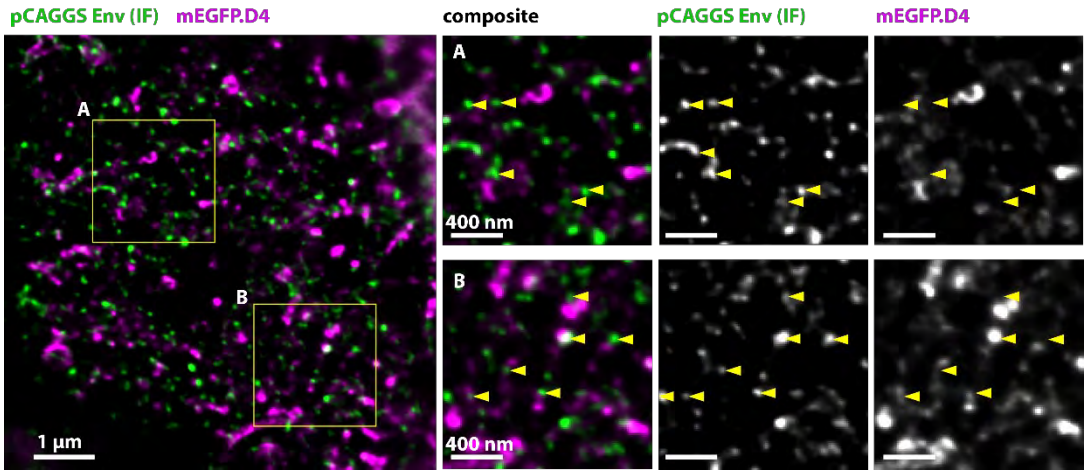

Figure 20. Env localizes to the periphery of mEGFP.D4 labeled Cholesterol domains. HeLa cells were transfected with pCAGGS.NL4-3 Env^{WT}. At 14h post transfection Cholesterol was labeled using mEGFP.D4 supplemented to the growth medium for 10 min at room temperature after which cells were washed and fixed with PFA. Subsequently, mEGFP.D4 was labeled with GFP Booster ATTO594 and Env was labeled using a primary human anti-gp120 (2G12) IgG and a secondary goat anti-human Fab fragment conjugated to Abberior STAR RED. Two-color STED imaging was performed on the apical membrane (left panel). Yellow bounding boxes A and B are enlarged on the right where punctate Env signals that localize close to the border of mEGFP.D4 signals are denoted with yellow arrows. STED images were deconvolved using the Richardson-Lucy algorithm as described in the Methods section.

3.9. The lipid ring domain largely colocalizes with the extended Env region in the periphery of the Gag assembly site

While the radial analysis indicated that Env localizes in the same region as Cholesterol and SM at the periphery of the Gag assembly site, a direct colocalization analysis would provide a more precise spatial relationship between Env and the lipid domain. To this end, STED microscopy was performed in cells transfected with equimolar amounts of pCHIV/pCHIV Gag.iCLIP plasmids where either Cholesterol or SM were stained using mEGFP.D4 or mEGFP.NT-Lys respectively, while Gag was left unlabeled in this case. Due to the limitations of the used system, imaging of only two channels in STED mode was possible, which necessitated the identification of HIV-1 assembly sites via the Env signal in contrast to previous experiments that used Gag.

Env is recruited to Gag assembly sites by laterally diffusing through the PM until it reaches the periphery of the Gag site where its mobility reduces and it forms larger circular domains. Therefore, not all membrane Env signals originate from HIV-1 assembly sites, and some represent Gag-free Env clusters. However,

ring-shaped Env signals with a diameter up to ~250 nm can only be observed at the periphery of Gag assembly sites, when Env is co-expressed with Gag such as in the pCHIV transfection (**Figure 21 A** and **B**). This characteristic ring-shaped, Gag-specific Env pattern allows for reliable identification of HIV-1 assembly sites in the absence of Gag staining based only on the Env signal (**Figure 21 B**). When Env is expressed alone by transfecting cells with the pCAGGS plasmid carrying NL4-3 Env^{WT} without other HIV-1 proteins, a distribution of punctate Env signals on the PM, 70-150 nm in diameter, that sometimes coalesce into larger, irregular domains can be observed, but no ring-shaped domains can be discerned (**Figure 21 C**).

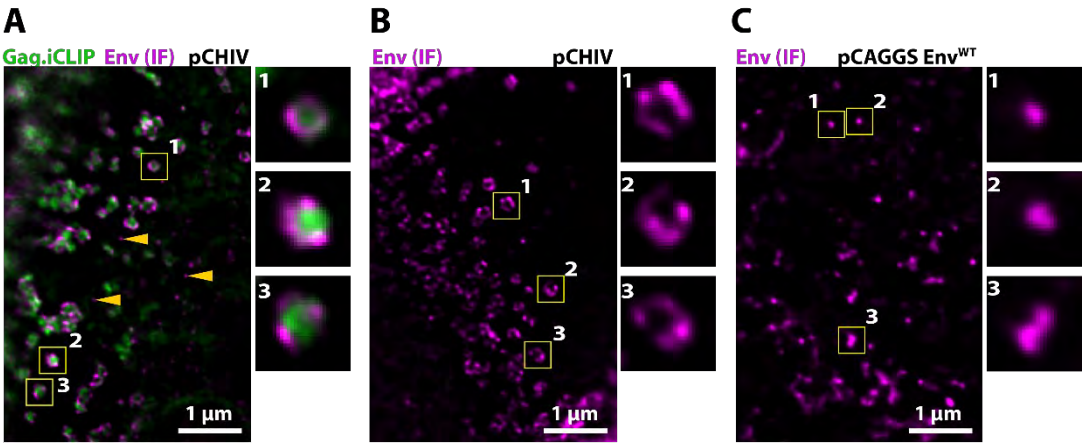

Figure 21. Ring-shaped Env signal is only seen associated with Gag. HeLa cells were transfected with an equimolar mixture of pCHIV/pCHIV Gag.iCLIP **(A and B)** or with pCAGGS.NL4-3 Env^{WT}**(C)**. At 14h post transfection, Gag.iCLIP was labeled with ATTO590-BC **(A)** or left unlabeled **(B and C)**. After PFA fixation, Env was detected via indirect immunofluorescence using a primary human anti-gp120 (2G12) IgG and secondary STAR RED-tagged anti-human Fab fragment. A segment of the apical membrane imaged in dual-color 2D STED mode is shown in **(A)**. Boxed regions containing representative Gag assembly sites with ring-shaped Env domains are shown enlarged in the side panel. Gag-free, punctate Env signals are highlighted with an arrow. A segment of apical the PM imaged in single-color 2D STED mode is shown in **(B and C)**. Boxed regions containing representative examples of **(B)** characteristic ring-shaped Env signals that identify HIV-1 assemblies and **(C)** punctate Env signals in the absence of Gag are shown enlarged in the side panels. Size of all enlargements is 400x400 nm.

Therefore, in contrast to previous experiments where Gag signal was used to identify HIV-1 assembly sites and determine the centroid, in the following experiments only ring-shaped Env signals could be used, enabling direct comparison of D4/NT-Lys domains with Env domains. In particular, after segmenting the image based on the Env signal, all segmentations that did not include fully formed ring-shaped Env signals were discarded. The segmentation was then further modified to fill all the segmentation holes and make all segments continuous ellipses

instead of donut-shaped, which is necessary for the calculation of the assembly centroid. The centroid is determined as the intersection of the minor and major axes of the resulting segmentation ellipse, and represents the 0 nm distance from the center of the assembly.

After pCHIV transfection, D4/NT-Lys labeling, washing and fixation, Env was immunolabeled using a primary human anti-Env IgG and a secondary anti-human Fab fragment directly coupled to ATTO590.

Two-color STED imaging of the apical PM revealed punctate and ring-shaped Env signals that partially co-localized with the mEGFP.D4 (**Figure 22 A**) and mEGFP.NT-Lys (**Figure 22 D**) ring-shaped and punctate signals respectively. Punctate signals of both Env and D4/NT-Lys were observed independently of each other at relatively low frequency, while ring-shaped Env signals were almost always accompanied by matching ring-shaped lipid probe signals and vice versa. At HIV-1 assemblies identified by the characteristic full-ring Env signals, the overlap between the Env signal and the lipid probe signal was high for both mEGFP.D4 (**Figure 22 B**) and mEGFP.NT-Lys (**Figure 22 E**). Additionally, closer inspection of individual assemblies indicated that D4/NT-Lys ring domains on average had a slightly smaller diameter than the Env ring. Radial profile analysis of 130 HIV-1 assemblies, revealed that Env signal peaked at 60 nm while mEGFP.D4 peaked at 45 nm from the center of the assembly (**Figure 22 C**). Analysis of additional 205 assemblies showed an Env signal peak at 75 nm while mEGFP.NT-Lys peaked at 60 nm (**Figure 22 F**). These data suggested that Env and lipid domains intimately interact at the borders of Gag assembly sites, which may play a role in Env incorporation or recruitment.

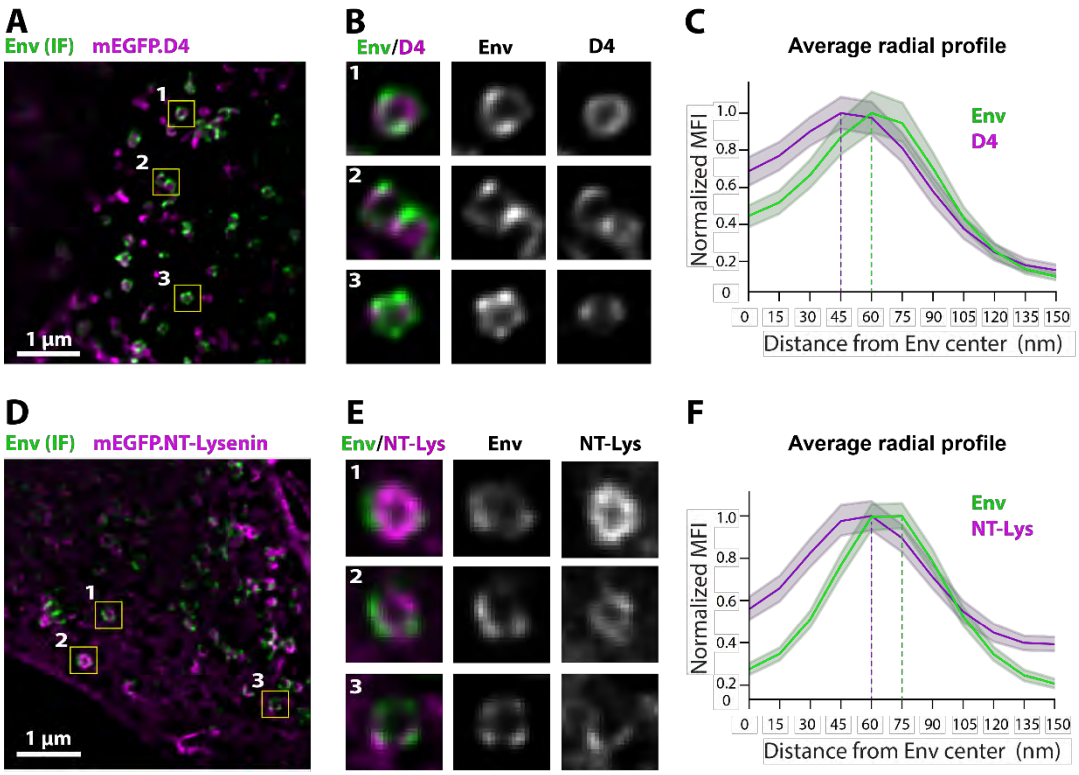

Figure 22. Cholesterol- and SM-rich ring domains overlap with the Env domain. HeLa cells were transfected with an equimolar mixture of pCHIV/pCHIV Gag.iCLIP. At 14h post transfection Cholesterol was labeled with mEGFP.D4 **(A, B, C)** or SM with mEGFP.NT-Lys **(D, E, F)** while Gag was left unlabeled. After PFA fixation, cells were labeled with ATTO647N-coupled anti-GFP nanobody to enable STED imaging of mEGFP.D4/NT-Lys. Envelope glycoprotein was detected via indirect immunofluorescence using a primary human anti-gp120 antibody and secondary STAR RED-labeled anti-human Fab fragment. A segment of the apical membrane imaged in dual-color STED mode is shown in **(A)** for D4 and **(D)** for NT-Lys. Boxed regions containing representative assembly domains with complete lipid and Env ring domains are shown enlarged in **(B)** for D4 and **(E)** for NT-Lys. The respective average radial profile analysis for D4 **(C)** and NT-Lys **(F)** stained, full-ring domains was obtained from N=130 and N=205 assemblies across three cells and two individual experiments performed as described in the Methods section. MFI was normalized to the maximum mean of all the assemblies in a set. Shaded areas depict the 95% confidence interval of the mean.

3.10. Lipid domain morphologies at HIV-1 assembly domains

The observed full-ring lipid domains, presumably composed of both Cholesterol and SM, were present at the border of many, but by far not all Gag assembly sites. Additionally, punctate and half-ring domains were observed. Initial visual inspection of multiple fields of view indicated a possible relationship between Gag domain size/intensity and the size/shape/intensity of the lipid domain associated with it. In order to explore this relationship and the distribution of lipid domain morphologies, a more detailed analysis of all observed Gag domains was

performed. Firstly, all Gag domains were automatically segmented from all fields of view. While in the previous experiments only Gag domains with a full-ring lipid domain were selected, this analysis included all individual punctate Gag domains with no respect to mEGFP.D4 signal. The segmentation was manually refined to all Gag domains that could be identified as single domains, sufficiently separated from any clusters and in the focal plane of imaging, while the lipid domain channel was kept hidden during the entire segmentation and refinement process to prevent any selection bias. Three distinct mEGFP.D4 signal morphologies were observed in this population of Gag sites: punctate, half-ring and full-ring. Gag sites without any D4 signal were rarely observed but were also included in the analysis. This manual categorization revealed for 415 observed Gag assembly sites that 27% had a full ring lipid signal, 28% a half ring domain, 40% a punctate signal and 5% exhibited no apparent D4 signal associated (**Figure 23 A**). Interestingly, the smaller, punctate mEGFP.D4 signals were usually associated with smaller and less intense Gag sites then those associated with full-ring mEGFP.D4 signals. Since Gag domain size and fluorescence intensity both increase over time as assembly progresses towards the late stages, this indicated that different assembly stages may be associated with different lipid domain morphologies. To test this hypothesis, Gag integrated density (IntDen) was measured for assembly sites categorized in the different lipid signal categories described above.

Gag fluorescence intensity is a measure of the relative concentration of Gag molecules at a certain site, while the area of the site gives information about the physical space occupied by the Gag lattice. Both of these parameters can individually be used to compare the relative stage of assembly sites, however a more accurate variable that better approximates the assembly stage is their product – integrated density (IntDen). By multiplying fluorescence intensity with the size of the assembly site, a more descriptive parameter is calculated which corresponds to the relative amount (concentration x area) of Gag molecules. Thus, IntDen of Gag was used to compare the relative stage of assembly in the following experiment.

IntDen of each assembly site was calculated from Gag segmentation area and Gag intensity and normalized to the highest Gag IntDen value from all assemblies. Lowest median (M) of Gag IntDen was obtained for the group with no apparent D4 signal (N=21, M=0.046), then for the assemblies with punctate D4 signal (N=167, M=0.168,), followed by those with a half-ring D4 signal (N=117, M=0.321) while the highest median IntDen of Gag was observed for the assemblies with full-ring D4 morphology (N=110, M=0.537) (**Figure 23 B**). These data suggested that in the

initial stages of assembly, punctate lipid domain recruitment to the periphery of the Gag assembly site occurs, which increases in size in parallel with the growth of the Gag lattice until a large lipid domain is formed which fully encircles Gag. This concept is further explored on fully-encircled Gag domains in the next chapter, directly comparing the size and intensity of lipid domains with Gag.

Interestingly, some of the Gag sites fully encircled by the lipid domain displayed similar IntDen values as the sites from the “punctate” and “half-ring” groups (**Figure 23 B**), indicating that full encirclement of Gag may occur even at the early stages of assembly. It is possible therefore that in some cases Gag oligomerization and lipid recruitment may not be fully synchronized, such that lipid recruitment sometimes outpaces Gag oligomerization.

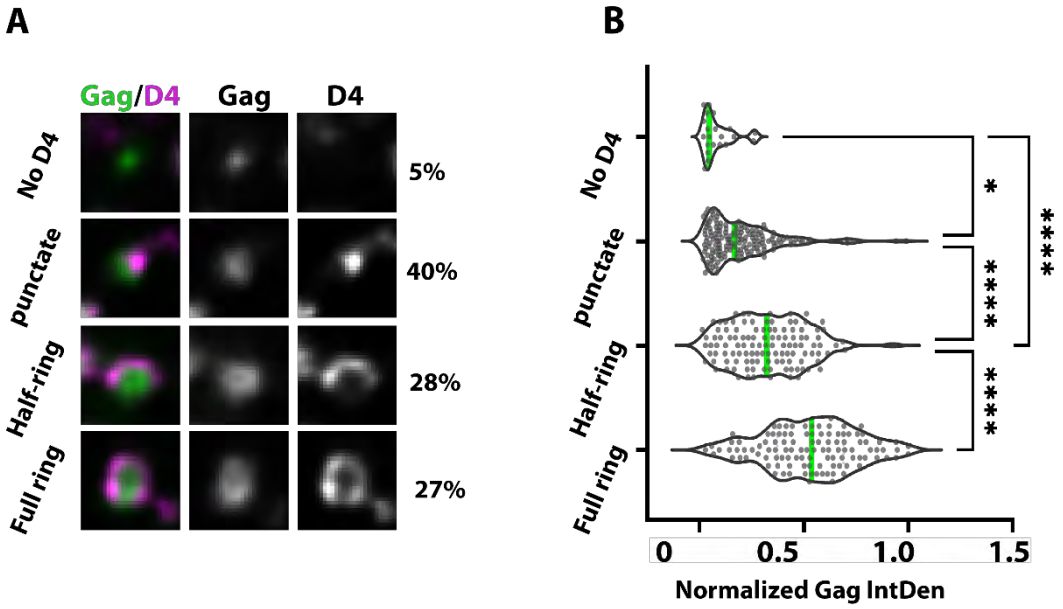

Figure 23. Gag domains are more frequently fully encircled by lipid domains in late stages than in initial stages of HIV-1 assembly. HeLa cells transfected with an equimolar ratio of pCHIV pCHIV Gag.iCLIP were labeled for Gag with ATTO590-BC and Cholesterol with mEGFP.D4 and fixed 14h post transfection. mEGFP.D4 was immunolabeled with GFP Booster ATTO647N and cells were imaged at the apical PM using STED microscopy. After automatic segmentation based on the Gag signal, a manual refinement was performed to exclude out-of-focus and clustered domains from further analysis while the D4 channel was kept hidden. **(A)** Four distinct observed Gag-associated Cholesterol domain morphologies were manually counted and represented as a fraction of the total number of counted Gag domains. Size of cutouts is 400 x 400 nm. **(B)** Median Gag integrated density (green line) was compared between the observed morphologies using a nonparametric one-way ANOVA with a Kruskall-Wallis post-hoc test for significance (* $P \leq 0.05$,**** $P \leq 0.0001$). Frequency of the respective morphologies and Gag integrated density was calculated from N=415 assemblies from 20 fields of view originating from three cells and two independent experiments. Gag integrated density was normalized to the highest value of all the whole set.

3.11. Lipid ring diameter and lipid signal intensity increase as HIV-1 Gag assembly progresses

Building on the hypothesis from the previous chapter, which suggests a direct link between Gag oligomerization and the progressive recruitment of lipid domains, it seemed plausible that the expansion of the Gag lattice would be accompanied by a corresponding increase in lipid domain size. This increase in ring size would accommodate the growing lattice while maintaining the full-ring morphology which would necessitate further recruitment of punctate domains or Cholesterol recruitment from the disordered phase. To compare the lipid ring diameter and intensity at different stages of assembly, Gag assembly sites were divided into 10 groups based on Gag integrated density, with each group representing a range from the lowest 10% to the highest 10% (**Figure 24 A**). To ensure the groups are representative of a linear distribution of Gag sizes and intensities and enable unbiased comparison between groups, the binning was done so that the median Gag integrated density of each group was evenly spaced across the range (**Figure *24* A**). Next, radial intensity analysis was performed for each group individually and the distance of mEGFP.D4 signal peak from the center of Gag was compared between the groups. In the group with the lowest 10% Gag integrated density the peak D4 signal was located at ~ 30 nm from the center of the Gag signal, which gradually increased in the next groups and was at its maximum (~ 60 nm) in the group with the highest 10% Gag integrated density (**Figure 24 B**). Furthermore, the increase of D4 ring size in this dataset was accompanied by an increase in mean D4 fluorescence intensity of the peak, as the intensity of the lowest 10% Gag group peak (Rel.D4 Mean intensity=0.56; 30 nm column; bottom row in **Figure 24 C**) had lower average mean intensity than the highest Gag group (Rel.D4 Mean intensity=1.0; 60 nm column, top row in **Figure 24 C**). Together, this suggested that the progression of budding, judged by the increase of Gag IntDen, is correlated with the increase in diameter of the associated lipid domain and in the amount of Cholesterol at the periphery of the Gag site further fortifying the hypothesis of continuous lipid recruitment to the site as it grows.

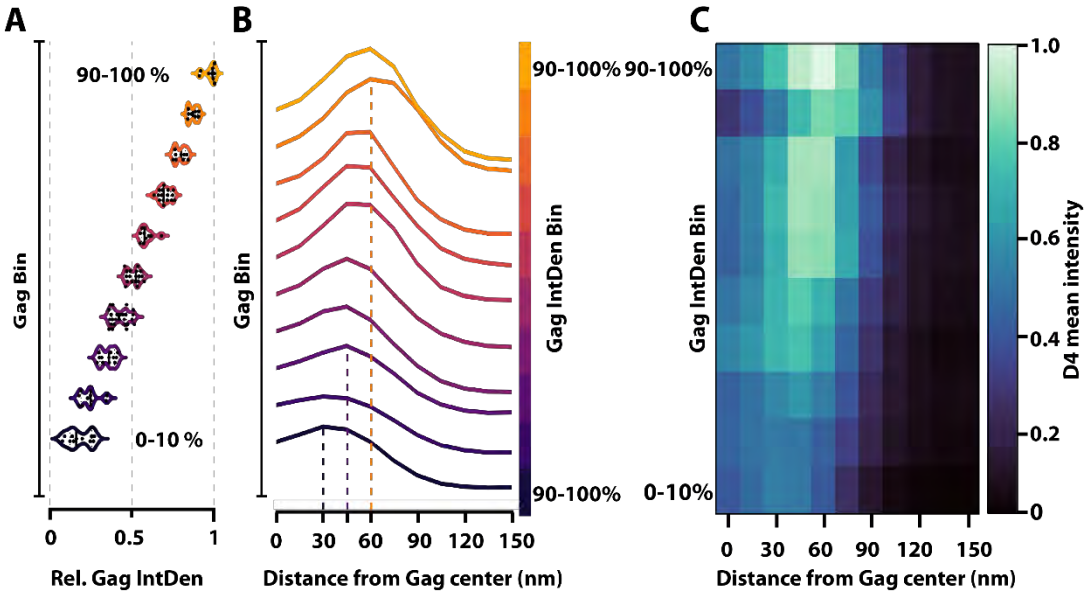

Figure 24. Cholesterol domain size and intensity increases with Gag domain size. Data acquired from the experiment presented in Figure 23. HeLa cells were transfected with an equimolar mix of pCHIV and pCHIV Gag.iCLIP.14h post transfection cells were stained for Gag (ATTO590-BC), Cholesterol (mEGFP.D4) and fixed. Immunostaining of mEGFP.D4 with GFP Booster ATTO647 was performed before STED microscopy of the apical membrane of cells. After automatic Gag segmentation a manual selection of Gag domains that were fully encircled by the Cholesterol domain was performed. **(A)** Based on Gag integrated density, these domains were binned into 10 groups with equidistant median values. **(B)** The average radial mEGFP.D4 profile was plotted for each Gag bin based on the distance from the Gag centroid with the group comprised of the lowest 10% Gag integrated density domains placed at the bottom (dark purple line) and the highest 10% at the top (yellow line) for comparison of peak mEGFP.D4 signal positioning between the groups. The y-axis is arbitrary, but relative height of peaks between bins is maintained. **(C)** A heatmap representation of the same data shown in **(B)** allowing for the comparison of mEGFP.D4 relative mean intensity between the bins for each distance. Columns define the position from the center of the Gag centroid in increments of 15 nm. Rows define the different Gag bins in increments of 10% Gag integrated density. Data was obtained from N=153 assemblies from three cells and two individual experiments.

3.12. Membrane curvature as a potential mechanism of lipid recruitment

HIV-1 budding necessitates the induction and continuous increase of membrane curvature throughout the assembly and budding process. Positive curvature is generated across most of the Gag lattice surface and negative at the borders of the lattice and the bud neck. Given that membrane curvature has been implicated in lipid rearrangement, and the observations in this thesis show specific progressive lipid accumulation at the Gag site borders as the assembly progresses,

it seemed plausible that negative membrane curvature, located at borders of the Gag assembly site may play a role in driving lipid recruitment to these regions.

To test this hypothesis, I employed a previously described Gag^{CA3} mutant that lacks the SP1 region located between CA and NC (Kräusslich et al. 1995). This Gag^{CA3} mutant targets to and anchors at the PM, but does not induce normal sized assembly sites, and leads to an electron-dense lattice of variable size, growing to many times the size of a single Gag^{WT} assembly lattice. Notably, the lattice of this Gag^{CA3} mutant carrying the SP1 deletion is unable to bend the membrane (**Figure *25* A**) and successfully proceed with budding, often forming a flat sheet-like domain parallel to the PM, likely due to altered CA-CA interactions and lattice organization. Occasional VLPs are formed by membrane blebbing rather than the usual budding process. I compared assembly sites of this variant with Gag^{WT} to examine how the absence of negative curvature reflects on the recruitment of Cholesterol and SM.

Co-staining of Gag^{CA3}.iCLIP and mEGFP.D4 in HeLa cells and imaging of the apical PM in 2D STED mode revealed small punctate Gag^{CA3} signals ~100-200 nm in diameter as well as large, elongated and irregularly shaped Gag^{CA3} signals reaching ~400-800 nm in length (**Figure 23 B**). mEGFP.D4 staining revealed punctate Cholesterol domains of a similar size range as punctate Gag^{CA3} as well as slightly larger elongated domains (**Figure *25* B**). Co-localization between Gag^{CA3} and mEGFP.D4 signals appeared low on first inspection of PM sections from multiple cells, both for punctate Gag^{CA} signals (**Figure 25 B and C**) and for large Gag^{CA3} signals (**Figure *25* B and D**). Furthermore, no ring-shaped mEGFP.D4 signals were observed in the samples, either associated to a Gag^{CA3} signal nor Gag^{CA3}-free. In order to quantitatively asses this observation, both types of Gag^{CA3} signals were separately analyzed using the previously described radial intensity analysis protocol and manually inspected after the selection and segmentation process. The analysis was performed separately on two observed groups of Gag^{CA3} signals (small and large) in order to differentiate between a potential effect of lattice size and an effect on curvature. Semi-automated segmentation of Gag signals was performed using the Otsu thresholding algorithm followed by a manual segmentation correction to exclude out-of-focus signals while the mEGFP.D4 channel was kept hidden throughout the entire process. Punctate Gag^{CA3} signals were selected separately and classified as “small” and all non-punctate shaped Gag^{CA3} signals larger than 200 nm were classified as “large” in the segmentation process preceding the intensity profile analysis. The segmentation included 406 small and 148 large Gag^{CA3} signals from two cells and two individual experiments. The median radius of

punctate small Gag^{CA3} signals was 44 nm (width from x=0 nm to x at signal half maximum), from which a median diameter of selected signals was calculated to be 88 nm (**Figure *25* E**). Average signal-to-background ratio (SBR) of 6.7 for the Gag^{CA3} sites was measured by dividing the median Gag^{CA3} signal value at its maximum (x=0 nm) by the background signal level at x=150 nm. The median mEGFP.D4 signal at these sites was at background levels (SBR of 2.1) (**Figure *25* E**), indicating a low level of co-localization between Gag^{CA3} and mEGFP.D4. Manual inspection of all 406 punctate Gag^{CA3} signals revealed that indeed only a very small number of selected Gag^{CA3} signals was associated with punctate mEGFP.D4 signals on their periphery or directly overlapping with Gag^{CA3} signal and typically no D4 signal could be observed at these sites (examples in **Figure *25* C)**. The analysis of large Gag^{CA3} signals also revealed only background mEGFP.D4 levels at those sites (**Figure *25* F**), while visual inspection revealed only occasional punctate mEGFP.D4 signals at the periphery of Gag^{CA3} (examples in **Figure *25* D)**.Together, these data indicated that negative membrane curvature might be necessary for Cholesterol recruitment and retainment at HIV-1 assembly site borders.

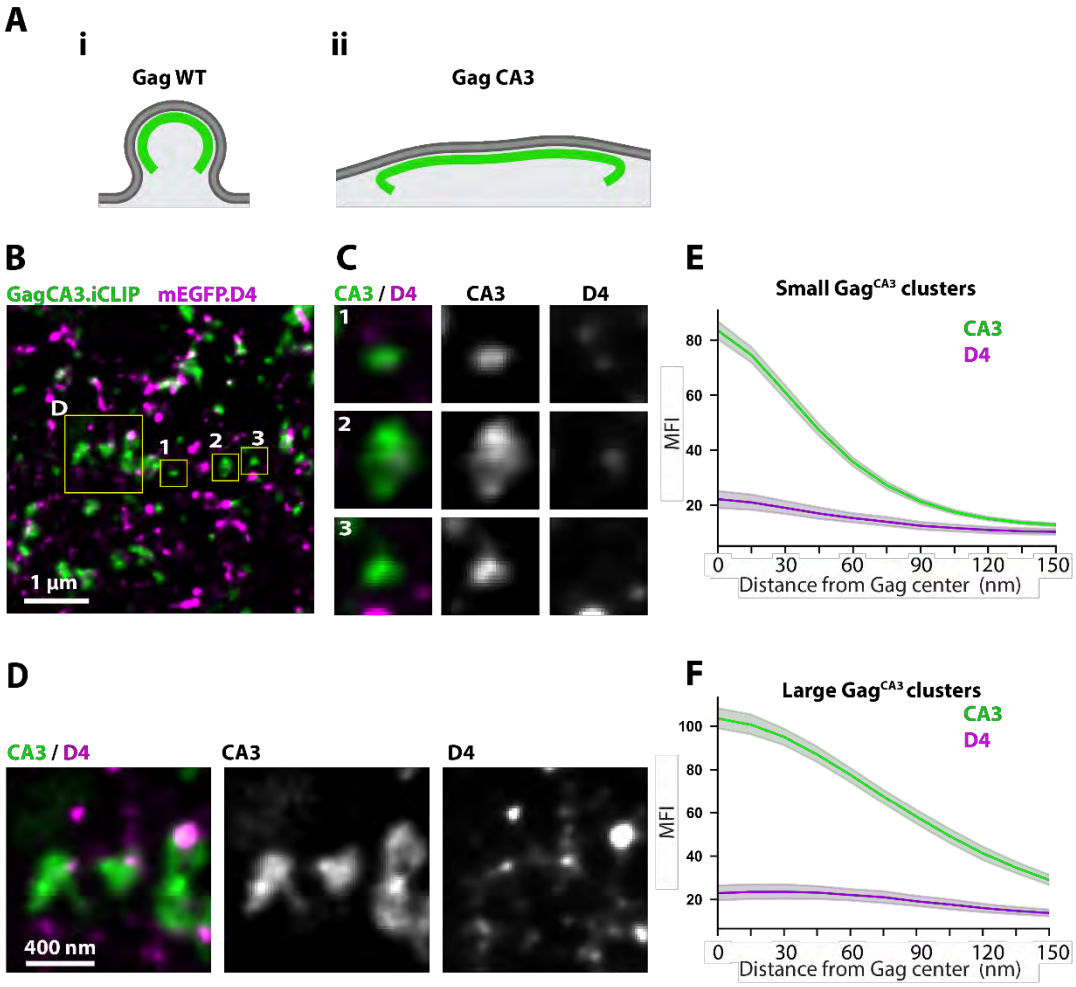

Figure 25. Membrane curvature is a key aspect of lipid recruitment and enrichment at HIV-1 assembly sites. (A) Schematic cross-section representation of typical Gag^{WT} **(i)** and Gag^{CA3} **(ii)** assembly domains in late stages illustrating the inability of Gag^{CA3} to induce membrane curvature. **(B-F)** HeLa cells were transfected with an equimolar ratio of pCHIV plasmids encoding Gag^{CA3} and Gag^{CA3}.iCLIP. At 14h post transfection, Gag^{CA3}.iCLIP was stained with ATTO590-BC, Cholesterol with mEGFP.D4 and cells were fixed with 4% PFA. After mEGFP.D4 immunolabeling with GFP Booster ATTO647N, cells were imaged using STED microscopy. **(B)** Dual-color STED segment of the apical membrane with boxed regions of representative small punctate assemblies enlarged in **(C)** and large irregular Gag^{CA3} assemblies enlarged in **(D)**. Size of cutouts in **(C)** is 400 x 400 nm. Radial fluorescence intensity profiles for small **(E)** and large **(F)** assemblies were acquired from N=406 an N=148 individual assemblies respectively from two cells. Shaded areas represent 95% confidence interval of the mean.

3.13. Neither curvature nor Cholesterol recruitment is necessary for Env recruitment

Since Env and D4 both localize to the periphery of Gag sites, presumably at the highly negatively curved region in the neck of the bud, a link between Env recruitment and lipid recruitment seemed possible. Thus, to explore a potential effect that lack of curvature and lipid domain recruitment has on Env recruitment and domain morphology, I analyzed the appearance and distribution of Env domains in Gag^{CA3} expressing cells.

To this end, STED microscopy of cells transfected with pCHIV containing the curvature mutant Gag^{CA3} was performed and localization of Gag^{CA3} and Env was observed.

Gag^{CA3} formed punctate and large irregular elongated assembly sites on the apical PM of transfected cells which were frequently highly overlapping with Env signals of similar size (**Figure *26* A-C**). Env signals were predominantly punctate and didn't exceed 200 nm in diameter, even when associated with larger irregular Gag^{CA3} sites. Env signals that were not associated with Gag^{CA3} were readily observed and appeared no different in size distribution or shape from Env signals associated with Gag^{CA3}. No ring-shaped Env domains were observed in any sample. To assess the co-localization of Gag^{CA3} and Env in a quantitative manner, radial profile analysis was performed on small and large Gag^{CA3} sites separately as described in the Methods and section **3.12** (page 67). Selection and segmentation of Gag^{CA3} sites for analysis was done with the Env channel hidden to prevent selection bias. Final segmentation included 314 small punctate Gag^{CA3} sites which had a median radius of 35.5 nm (width from x=0 to x at signal half maximum) thus calculating the median diameter of these sites to be 71 nm and an SBR of 11.9 (**Figure *26* D**). Env median signal profile was the same shape as that of Gag^{CA3} with a maximum at x=0 and SBR of 3.9 while the median radius was 37.5 nm (diameter 75 nm) (**Figure *26* D**), indicating a significant level of signal overlap and intensity correlation with Gag^{CA3}. Visual inspection of all selected Gag^{CA3} sites revealed that nearly all of them overlapped with a punctate Env signal to a high degree. Profile analysis of large Gag^{CA3} sites revealed a mean radius of 68 nm (diameter of 136 nm) for Gag^{CA3} signal (SBR of 6) and 71 nm (diameter of 142 nm) for the Env signal (SBR of 4.5).

Since Cholesterol domain formation depended on Gag-induced membrane curvature (**Figure *25***) but Env recruitment did not (**Figure *26***), it logically follows that the observed lipid microdomain recruitment at the periphery of Gag sites is not essential for Env recruitment. However its role in potentially enhancing Env recruitment or modulating its distribution cannot be discounted. Additionally, these data show that negative curvature induced by the Gag lattice formation is not essential in Env recruitment either, and that Env trapping occurs by a lattice organization likely quite different from that of Gag^{WT}.

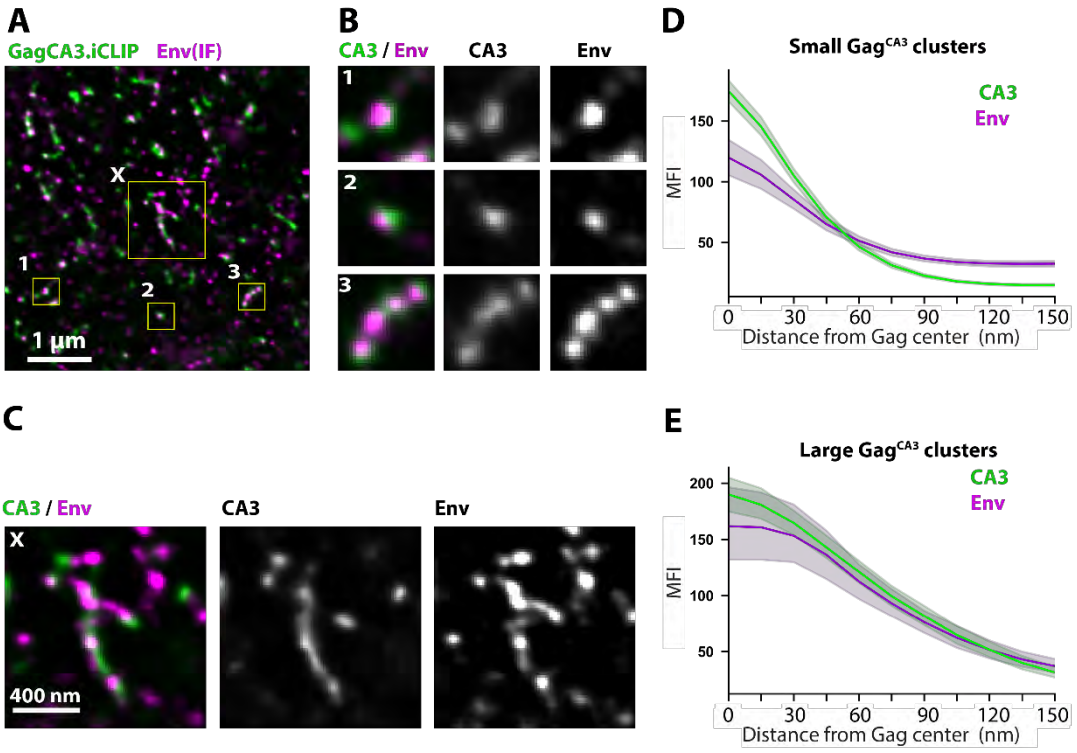

Figure 26. Env recruitment to Gag domains is retained irrespective of membrane curvature. HeLa cells were transfected with an equimolar ratio of pCHIV plasmids encoding Gag^{CA3} and Gag^{CA3}.iCLIP. At 14h post transfection, Gag^{CA3}.iCLIP was stained with ATTO590-BC and cells were fixed with 4% PFA. Env glycoprotein was immunolabeled with a primary human anti-gp120 antibody and secondary anti-human Fab coupled to Abberior STAR RED. STED microscopy was performed on the apical membrane of transfected cells. **(A)** Segment of the apical membrane in dual-color 2D STED microscopy with boxed regions of small punctate domains enlarged in **(B)** and large irregular Gag^{CA3} domains enlarged in **(C)**. Size of cutouts in **(B)** is 400 x 400 nm. Radial fluorescence intensity profiles for small **(D)** and large **(E)** assemblies were acquired from N=314 an N=62 individual assemblies respectively from two cells. Shaded areas represent 95% confidence interval of the mean.

4. Discussion

Despite the advances in microscopy techniques and chemical biology tools the lipid composition and dynamics at assembly sites of HIV-1 still remain a poorly understood subject. This work aimed to gain further insight into the organization of lipids during HIV-1 biogenesis in relation to viral Gag and Env proteins using super-resolution STED microscopy. By utilizing well characterized lipid probes, super-resolution imaging of native Cholesterol and SM domains on the PM of cells revealed a striking colocalization with HIV-1 assembly sites and allowed for spatial characterization of the newly discovered lipid-ring phenotype which led to the formulation of a model of lipid coalescence that depends on Gag oligomerization and local membrane curvature.

4.1. STED super-resolution imaging of Pac-Cholesterol

In this thesis I tested the applicability of a commercially available bifunctional Cholesterol derivative Pac-Cholesterol (PhotoClick Cholesterol, Sigma)(Hulce et al. 2013) to study native cellular Cholesterol localization via super-resolution STED imaging at HIV-1 assembly sites. This minimally modified Cholesterol contains an ester-linked alkyne group, enabling click-labeling, and a diazirine group for UV-induced fixation and lipid immobilization via protein cross-linking. Bifunctional lipids with the same chemical groups have been made for: PC (Gubbens et al. 2009; Gubbens and Kroon 2010) – to study PC in mitochondrial function, palmitic acid (Haberkant et al. 2013) – for protein-lipid profiling and microscopy in cells as well as *C. elegans*, sphingosine (Haberkant et al. 2016; Gerl et al. 2016) – for sphingolipid-protein interaction studies and PIP2 (Mücksch 2017) – used in confocal microscopy and HIV-1 Gag co-precipitation study.

An analogue lacking the alkyne group, 6-photocholesterol, has been previously shown to faithfully mimic Cholesterol in retaining the ability to facilitate fusion of two different alpha viruses with liposomes and to condense phospholipid (POPC) films to the same extent as native Cholesterol (Mintzer et al. 2002). Tritiated 6-photocholesterol was used to identify synaptophysin binding to Cholesterol (Thiele et al. 2000), where authors proposed additional evidence that photocholesterol acts like native Cholesterol because it incorporated into detergent insoluble complexes (DICs) and specifically labeled apolipoproteins and caveolin/VIP21. Alkyne cholesterol mimicked Cholesterol well in enzymatic reactions and in cell distribution

using confocal microscopy (Hofmann et al. 2014). More recently, Hu et al. used a bifunctional analogue closer in structure to native Cholesterol then Pac-Cholesterol (**Figure 27**) to show that influenza hemagglutinin A (HA) binds to Cholesterol which is essential for viral replication efficiency with pleiotropic effects on virus assembly and fusion (Hu et al. 2019). In this thesis however Pac-Cholesterol did not mimic the distribution of native Cholesterol stained by Filipin, displaying high intracellular staining and an almost undetectable PM signal (

Figure 6). Furthermore, Pac-Cholesterol extraction with MβCD was very inefficient and internal membrane staining resulted in high background signal that hampered efficient STED imaging in whole cells. I tried to overcome this problem by imaging Pac-Cholesterol in PLL-attached membrane sheets however due to the lack of depletion with MβCD and colocalization with the raft marker CTxB this compound was deemed unsuitable to study Cholesterol localization at HIV-1 assembly sites using STED microscopy. Considering that Pac-Cholesterol feeding to cells first leads to its release into the cell PM and subsequently to distribution throughout the cell, it remains unclear why Pac-Cholesterol predominantly localized to endomembrane compartments while very low PM concentrations were achieved. However, a discovery by Naito et al. suggests that ER-anchored GRAMD1 proteins rapidly direct acute increase of the accessible PM Cholesterol pool toward the ER (Naito et al. 2019), which may provide a possible explanation. Such rapid Cholesterol translocation from the PM would explain the results of poor MβCD extractability of Pac-Cholesterol (**Figure 6**) and its high endomembrane staining, since most of the PM fraction would likely be rapidly internalized. Testing if a reduction of GRAMD1 activity or the kinetics of inducing PM contacts provide better PM retention of the Pac-Cholesterol may therefore be worthwhile for future PM microscopy studies of Cholesterol.

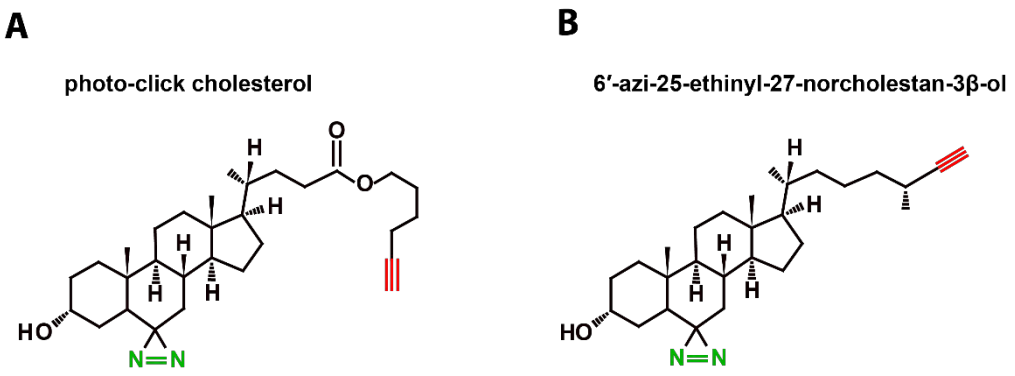

Figure 27. Structure of the commercially available bifunctional Cholesterol (A) used in this study (Pac-Cholesterol) and the minimally modified analogue (B) used in the study of Hu et al.(Hu et al. 2019)

4.2. Cholesterol and SM cluster into a ring-domain that encircles Gag

The use of recombinant mEGFP fusions of D4 and NT-Lys proteins allowed for an intense and specific staining of native Cholesterol and SM in the outer leaflet of the PM of cultured cells. One of the advantages of using such probes instead of the synthetic lipid analogues is the selective staining of domains which contain Cholesterol or SM above a certain threshold (~40 mol% Cholesterol for D4) and specifically only in the outer leaflet of the PM. This allows for a more focused approach compared to the synthetic lipids which would distribute into both leaflets while allowing very low concentrations of analogues to be detected, potentially masking an underlying event occurring in a single leaflet. In addition, results from our lab and from others have previously shown that lipids retain approximately 60-80% of their mobility after PFA fixation (Mücksch 2017; Tanaka et al. 2010), which can greatly impede super-resolution imaging in fixed cells. In contrast, protein probes such as D4 may limit the movement of the bound lipid momentarily after recognition, while PFA fixation would permanently constrain the detected domains to the initial place of detection by crosslinking tightly clustered mEGFP.D4 molecules, making this approach favorable over synthetic lipid analogues in that regard. Lipid labeling only takes 5 - 10 minutes at room temperature for sufficient signal to be detected at the PM. The momentary and gradual constraint of lipid domains that are recognized by the probe may, to some extent, affect the assembly process which usually takes ~10 min until ESCRT is recruited, however cellular integrity remains visually intact in this short time. Nevertheless, linkage of a large protein probe (43 kDa for mEGFP.D4) will significantly slow down the metabolism

and mobility of bound lipids which makes these probes only suitable for fixed cell experiments.

A high level of association of D4 with Gag was observed at the PM of pCHIV transfected cells. D4 staining revealed punctate Cholesterol domains associated usually slightly offset from the center of the Gag signal, as well as domains that partly and fully encircled the Gag signal. This finding hinted at a possible gradual process of Cholesterol coalescence from punctate Gag-proximal clusters to domains that fully encircle Gag. Categorizing individual domain morphologies based on size and intensity of Gag signal, as a proxy for relative age of the assembly, revealed a trend where punctate Cholesterol domains were more often found in small and less intense Gag assemblies while those that were fully encircled by Cholesterol were larger and more intense (**Figure 23**). This would be in line with the hypothesis that gradual coalescence of Cholesterol at the periphery of the Gag lattice results in a fully Cholesterol-encircled assembly.

Interestingly, only 5% of the observed assembly domains had no D4 signal associated with them. One of the initial indications which could explain such a distribution is that Gag is predominantly recruited to the inner leaflet PIP2 domains which are already in register with outer leaflet cholesterol. However, PIP2 displays a very high level of co-localization with Gag signal as observed previously (Mücksch 2017) and in line with a large number of studies that characterized direct MA binding to PIP2 as an anchoring mechanism for Gag. In contrast, D4 signal was often offset from the Gag signal and was not fully colocalizing with Gag, indicating that initial Gag anchoring happens likely irrespective of the Cholesterol distribution on the outer leaflet, upon which Cholesterol accumulates at the lattice periphery, likely by lateral association, until it fully encircles it.

Additionally, the ability to stain Cholesterol with D4 in detached particles next to the cell indicates that a large portion of the observed circular domain likely gets incorporated into the particle, perhaps during ESCRT-mediated scission, and is in line with the observed high lipid order of the viral membrane (Lorizate et al. 2009) and increased Cholesterol content compared to the PM in the lipidomic studies (Brügger et al. 2006; Lorizate et al. 2013; Chan et al. 2008).

4.3. Are SM and Cholesterol recruited separately?

Without dual labeling of D4 together with NT-Lys, it cannot be determined whether the observed Cholesterol and SM belong to the same domain, especially in the early stages of assembly when predominantly punctate lipid domains were observed (**Figure 23**). This raises the question if the Cholesterol and SM domains truly co-localize at all times during virion biogenesis (**Figure *28* a.**), or if they are at first separate domains (**Figure *28* b.**) that coalesce into a Cholesterol/SM-rich domain once the assembly site is fully encircled. The heterogeneity of lipid microdomains is an incompletely explored area, but it is known that SM distributes into a high variety of domains with different packing and/or composition based on the co-staining experiments of lysenin with EqtxII, ostreolysin A and D4 (see the Introduction section **1.5.2.2**., page 31). Abe and colleagues discovered that upon MβCD treatment, both D4 (Cholesterol) and lysenin (SM) staining of cellular outer leaflet become undetectable. In contrast, SMase treatment only makes lysenin staining undetectable while D4 is unaffected (Abe et al. 2012). This indicates that the pool of SM stained by Lys likely interacts with Cholesterol domains stained by D4 which is important for SM clustering while SM is not essential for Cholesterol clustering. However, Besenicar et al. found that Cholesterol extraction by MβCD happens slower when SM is present, likely because SM facilitates Cholesterol clustering (Besenicar et al. 2008). This would be supported by the finding that MβCD preferentially extracts cholesterol from the disordered phase – not when it forms highly ordered domains (Sanchez et al. 2011).

Contradicting the results of Abe et al., He et al. found that MβCD depletion does not result in Lys staining abrogation (He et al. 2017). Considering that both approaches used very similar Lys constructs, the discrepancy might come from the different cell lines the experiments were performed in. Namely, Abe et al. employed EGFP.NT-Lys or directly labeled Alexa647-Lysenin in HeLa cells whereas He et al. used N^{15} labeled NT-Lys in a nano-SIMS approach in CHO-K1 cell line. Since a HeLa cell line was also used in this thesis, and taking into account data from Abe et al. which a more similar NT-Lys construct to the one used in this thesis, one could hypothesize that Lys and D4 staining observed at HIV-1 sites originates from the same domain or two very closely interacting domains, suggesting the model shown in (**Figure *28* a.**). Future experiments should include D4 and NT-Lys co-staining to determine if these probes stain the same domain and if not, if separate domains are recruited simultaneously or in a defined order. In addition, Abe et al.

found that SM coalescence into domains is necessary for PIP2 domain formation and inner leaflet PIP2 domains are dissolved upon SM depletion with SMase (Abe et al. 2012). This was supported by their PALM/STORM experiment where they show that outer leaflet SM domains stained by NT-Lys remain in register with inner leaflet PIP2 through possible transbilayer coupling, which might indicate towards an initial SM recruitment to the assembly domains immediately upon Gag anchoring followed by Cholesterol recruitment.

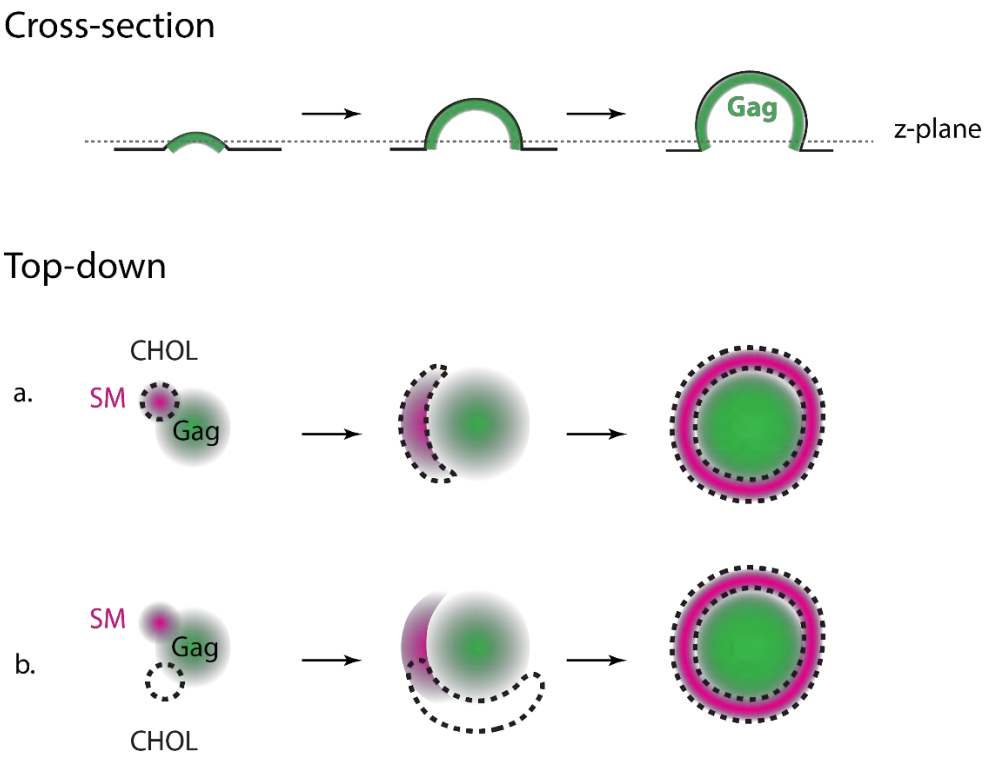

Figure 28. Potential modes of Cholesterol and SM coalescence during HIV-1 assembly. The process of budding is shown in the cross-section representation with the Gag lattice corresponding to the respective stages viewed in the top-down orientation where Gag (green), SM (magenta) and Cholesterol (dashed black line) domains are represented. In the model **(a.)** SM and Cholesterol signals belong to the same domain while in the second **(b.)** they represent two distinct domains that later likely coalesce once the ring domain is formed.

4.4. Is the lipid ring the ground truth 3D object in the sample?

The 2D laser depletion scheme, such as the one used in the STED system in this thesis, results in an excitation beam profile of 60-80 nm in the xy direction and 500-600 nm in the z- direction at the focal plane. Such a large axial depth of excitation in combination with the small diameter of the Gag lattice shell (~100-120 nm) means that the entire volume of a HIV-1 assembly site gets projected onto a single 2D image. This makes the extrapolation of acquired 2D images from this volume into possible 3D objects that are truly present in the sample somewhat ambiguous. Namely, this brings into question if the 2D images showing a ring-shaped signal represent a genuine ring-shaped domain in the periphery of the Gag assembly as described in this thesis. Instead, the lipid domain could be uniformly distributed over the entire Gag shell, constructing a nearly complete sphere in the late stages of assembly, which would potentially result in a similar 2D projection to that of a planar ring domain.

The reason why a fluorescent sphere surface (**Figure 29 1a**) would appear as a ring in a 2D projection under the described conditions is because the fluorescence from a larger surface area at the equator of the sphere than at the pole of the sphere would be contained within a certain constant volume of excitation (**Figure 29 1b, v1 and v2**) as further described in section **6.15** (page 104) in Materials and Methods. This results in a higher number of fluorophores detected by pixel groups at the periphery of the sphere (px2) than in the center (px1), closer to the poles (**Figure 29 1c),** which generates an image of a circle with higher brightness on the borders then in the center (**Figure 29 1d**). The same principle applies for hemi-spheres which should have the same ratio of pole-to-equator signal intensity as full spheres, and therefore the same contrast, but would be half as bright as a sphere of the same radius (**Figure 29 2a-d**). A planar ring-shaped object would have a constant number of fluorophores detected across its surface regardless of the pixel position (**Figure 29 3a and b**), but would likely have the most contrast between its center and periphery out of the three examples since all fluorophores would be located at the periphery and none at the center (**Figure 29 3c and d.**).

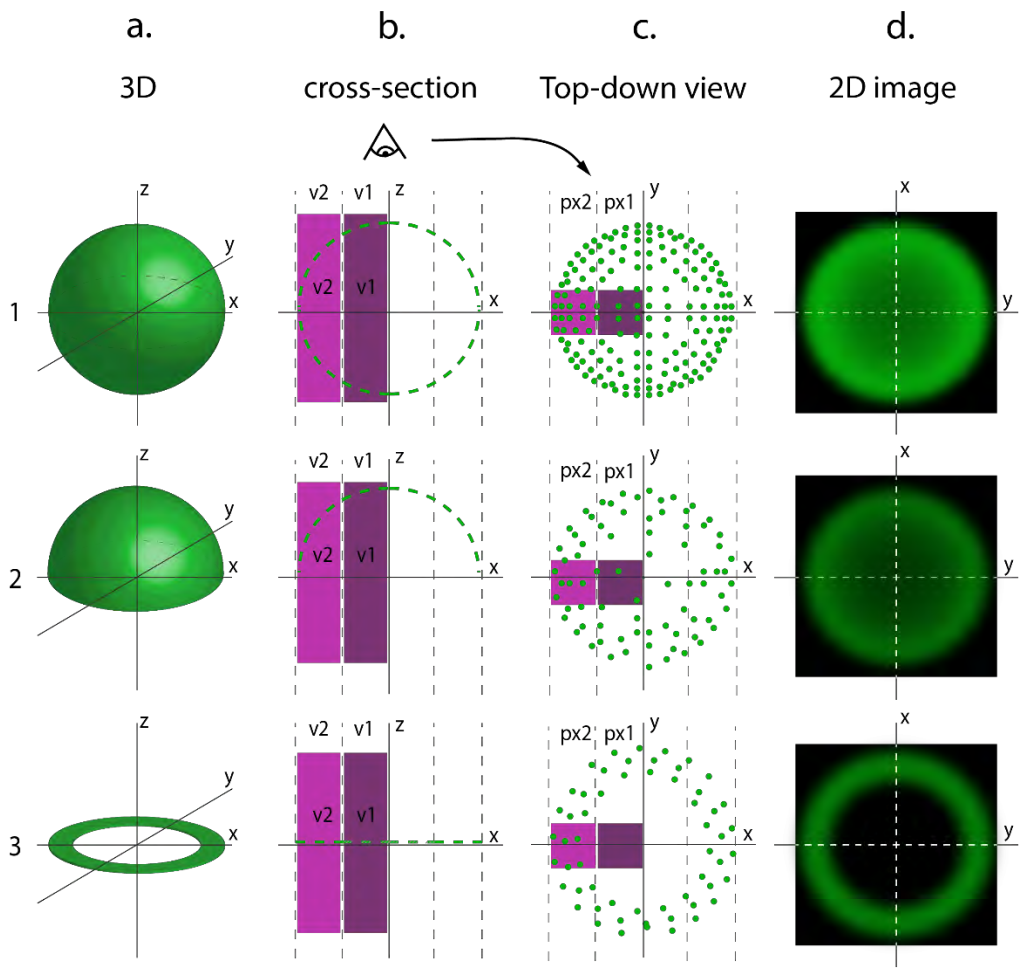

Figure 29. Illustrations of 2D projection predictions from 3D objects imaged by STED microscopy. Shown are schematic representations of a sphere **(row 1)**, hemisphere **(row 2)** and a planar ring **(row 3)** in 3D **(column a.)**, as a cross section **(column b.)**, in a top-down view **(column c.)** and as a corresponding predicted fluorescence image **(column d.)**. In the cross-sectional view **(b.)**, the dashed green line represents individual fluorophores on the surface of each object. The dark and bright purple rectangles (v1 and v2 respectively) represent simplified volumes of excitation (v1=v2) for pixels closer to the center (v1) and closer to the periphery (v2). In the top-down view **(c.)** green dots represent individual fluorophores as observed from the top and mapped onto a 2D surface (detector) with the central and peripheral pixel groups (px1 and px2 respectively) depicted as dark and bright purple squares respectively. 2D image projections are approximated illustrations and the ratio of intensity between the center and periphery may not be fully accurate. The size of pixels as well as volumes is arbitrary for illustration purposes. If the px1 and px2 groups are regarded as areas of 3x3 pixels (at 15nm pixel size), the ratio between pixel size in **(c.)** and excitation beam cross-section dimensions in **(b.)** would be close to a true imaging scenario. This would estimate the radius of the depicted sphere at ~90 nm. All 2D image projections were generated in Adobe Illustrator based on considerations described in section **6.15** (page 104) of Materials and Methods.

The data presented in this thesis however suggests that the lipid domains that appear to encircle the Gag site are planar, ring-shaped domains that are embedded within the PM at the periphery of the Gag domain (**Figure 30 A, 3D object**) rather than shells over the entire Gag lattice (**Figure 30 B, 3D object**). Firstly, I observed lipid ring structures even at small diameters of Gag sites (**Figure 23 B**) and therefore early stages of budding. Hemispherical lipid shells could in theory result in a ring-like appearance, as discussed in the previous paragraph, however curved 3D objects like spherical shells may not resolve clearly as ring-like structures in early budding events because of limitations in the axial (z) resolution. The Gag lattice assumes a hemispherical shape in the early stages of assembly, however ring-shaped Gag signals were observed extremely rarely and only in assembly sites with a diameter larger than ~120-140 nm. Thus it is unlikely that a hemispherical shell overlaying the Gag lattice at these stages could be resolved as a ring. A flat ring domain embedded in the plasma membrane is more likely to appear as a well-defined 2D ring because the contrast between the ring and its center is much larger. Additionally, a fully spherical lipid shell would theoretically only produce a ring-shaped 2D projection in later stages of assembly when the budding is nearly complete (**Figure 30 B4**). Secondly, while the 2D projections in both scenarios might appear similar in the early stages of assembly, when both Gag and the lipid domain are mostly punctate (**Figure 30**; compare stages 1 and 2 in A and B), their projections should diverge significantly as assembly progresses. The signal overlap should be large if the lipid domain matches the shape of the Gag lattice and smaller if it is a planar ring at the periphery of the Gag site (**Figure 30**; compare stages 3 and 4 in **A** and **B**). The observed low signal overlap between Gag and the lipid ring signals (**Figure 17**) therefore suggests that the lipid domain likely does not adopt the same shape as the Gag lattice. Additionally, imaging of released HIV-1 VLPs (average diameter ~120 nm) resulted in a punctate lipid signal (**Figure 21**). If the lipids formed a shell over the Gag lattice in the late stages of budding, which would be retained in the released VLP, the lipid domain that was resolved as a ring in the late bud stages should also be resolved as a ring in the released VLP. The fact that only punctate D4 signals could be observed at the VLP positions indicated that the lipid domain is either smaller, covering only a portion of the VLP surface, or that the lipid shell of that size could not be resolved as a ring under the used imaging conditions. A smaller domain could also be generated post-budding by condensation of the lipid shell into a smaller domain, however that would result in a higher localized D4 intensity at the VLPs compared to the budding sites, which was not observed.

Finally, if the lipid rings were an artifact of a spherical lipid shell, such domains would be lost at the Gag^{CA3} assemblies that are unable to bend the membrane, however the lipid recruitment would still be observed, which was not the case (**Figure 23**). Although this question remains unresolved, new microscopy techniques such as minimal fluorescence photon fluxes (MINFLUX) microscopy that approaches axial and lateral resolution of less than 10 nm could confirm or disprove the planar ring-shaped lipid domain proposed here.

A recent study by Tomishige et al. investigated native Cholesterol and SM distribution upon expression of HIV-1 by PALM/dSTORM microscopy by using directly labeled D4 and NT-Lys proteins with Alexa Fluor 647 (AF647)(Tomishige et al. 2023). They did not report on ring-shaped lipid domain structures but found that ~50% of Gag signal overlapped with D4 or NT-Lys signal and that Gag was frequently associated with the borders of D4 and NT-Lys domains. The level of Gag signal overlap observed in their study is in line with the findings presented here, considering that I saw high association between Gag and D4 or NT-Lys but only partial overlap of those signals and would argue against the full spherical lipid shell hypothesis based on the level of signal overlap as described above. The complete lack of ring-shaped lipid domains in the study by Tomishige et al. may stem from the differences between methods used in their study and this thesis. The most notable difference between is the microscopy approach since both studies were conducted in HeLa transfected cells expressing Gag.iCLIP (this thesis) or Gag.mEOS4b (Tomishige et al.), while lipids were labeled with mEGFP.D4/NT-Lys (this thesis) or AF647-D4/NT-Lys (Tomishige et al.). In this study I used STED, a confocal-based technique, to continuously monitor the imaged objects and reduce the possible artifacts as much as possible. This technique does not require any image reconstruction and relies only on deconvolution, for which artifacts are easily noticed and prevented. PALM/dSTORM has a theoretically lower axial resolution but may be more prone to artifacts due to sample preparation, fluorophore selection, drift correction or during image reconstruction. Alternatively, the ring domain observed in this study may be an artifact due to unspecific mEGFP interactions, however I saw no mEGFP binding to transfected cells in my experiments when it was supplemented to the media instead of mEGFP-D4 (not shown) and dimerization of mEGFP is inhibited by the A206K mutation (Zacharias et al. 2002).

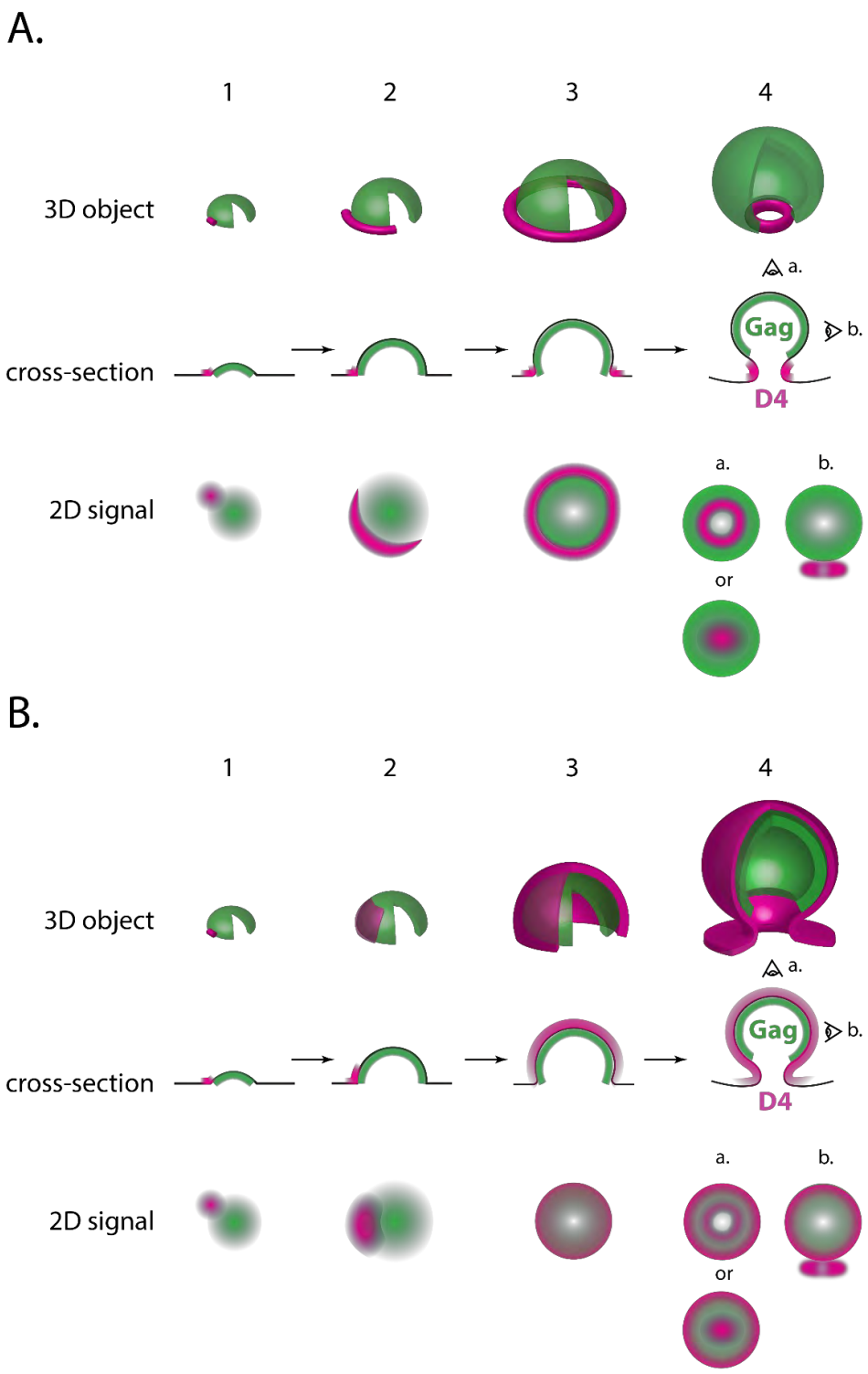

Figure 30. 3D representations of the Gag lattice (green) and lipid domain (purple) during different stages of HIV-1 assembly The hypothetical ring-shaped **(A)** and spherical **(B)** lipid domain distributions are shown as a 3D representation, cross-section and predicted fluorescence projection for early **(columns 1 and 2)** and later stages **(columns 3 and 4)** of HIV-1 assembly. In column 4, fluorescence predictions of perpendicular **(a)** and side-view **(b)** angles of observation are shown. Predictions of fluorescence projections represent only illustrated approximations and are not modelled to consider particle size, system resolution and comparison of intensity distribution between the objects. All 2D projections were illustrated in Adobe Illustrator with considerations from **Figure 29** and as described in section **6.15** (page 104) in Materials and Methods.

4.5. Lipid domains largely overlap with the Env extended domain in the periphery of Gag sites

The findings presented here, of an intensely stained extended ring-shaped Env region at the periphery of Gag sites have been described before (Muranyi et al. 2013; Mücksch et al. 2017; Muecksch et al. 2024) and are in line with the observed reduced mobility of Env at Gag assembly sites compared to Gag-free PM regions (Roy et al. 2013; Chojnacki and Eggeling 2021; Chojnacki et al. 2017). The preference of Env to the neck of the assembly bud, which is where the observed Env ring likely localizes, has also been shown in mobility studies (Buttler et al. 2018; Pezeshkian et al. 2019). As discussed in section **4.4** (page 79), this thesis proposes that the Cholesterol- and SM-rich ring domain also localizes to this region of high negative curvature, raising the question if these two domains interact and to what effect.

A mismatch in overlap between Env and lipid ring signals can be appreciated from the STED data and radial intensity analysis (**Figure 22**) such that lipid domain rings have a smaller radius and are therefore closer to the center of the assembly then Env. However, considering that signal peaks of Env and Cholesterol/SM from radial analysis are only 15 nm apart (1 pixel), this observation may be due to a high linkage error for Env, which is labeled with a primary IgG and secondary Fab fragment compared to a dye-coupled nanobody for D4/NT-Lys. Alternatively, these two domains may be physically separated and not mix with each other. The finding that when expressed alone, Env localizes to the borders of D4 clusters but is not embedded within them (**Figure 20**), would be in line with these two domains remaining separate at the neck of the assembly bud, but interacting attractively at the borders. Furthermore, Env is known to associate with lipid raft domains (Yang et al. 2010) and has a Cholesterol recognition sequence (Nieto-Garai et al. 2021). If Env is restricted from mEGFP.D4 stained domains it would be interesting to explore if such behavior plays a role in Env incorporation into the virion. The incorporation of an uncharacteristically small number of Env trimers (7-14) has been mostly attributed to steric restrictions by the Gag lattice. Since the virion detaches from the cell when the Gag lattice is roughly two thirds of a complete sphere, this would potentially allow for an incorporation of a large number of Env trimers into the virion during last stages of budding, when the highly populated Env domain could distribute over the membrane area in the neck where a hole in the Gag lattice would be located. It would be interesting to explore if and how Env distribution and potentially incorporation changes if the lipid ring at the Gag sites is perturbed and how Env

lacking the Cholesterol recognition sequence would localize in respect to Cholesterol-rich domains at Gag sites.

4.6. Lipid recruitment is induced by negative membrane curvature

Assembly of HIV-1 Gag leads to a positive PM curvature following the shape of the Gag lattice over the majority of the bud but also of a strong negative membrane curvature in the neck of the bud. Based on the observations presented in this thesis and as discussed in section **4.4** (page 79), the data indicates that the Cholesterol/SM-rich ring domain seen at Gag^{WT} sites originates from the accumulation of these lipids in the highly negatively curved region of the bud neck. This is supported by numerous studies demonstrating Cholesterol preference towards negatively curved membrane regions and its effect on lowering the energy necessary to induce negative curvature (Wang et al. 2007; Churchward et al. 2005; Churchward et al. 2008). Cholesterol recruitment to the cleavage furrow during cytokinesis was previously observed while inhibiting its recruitment led to cytokinesis failure (Abe et al. 2012). Caveolae generation was found to be dependent on Cholesterol recruitment which aids in caveolin-1 membrane curvature generation and maintenance (Krishna and Sengupta 2019). These cell invaginations are enriched in Cholesterol (Anderson 1998; Hubert et al. 2020) and its depletion with MβCD results in flattening of the pits (Morén et al. 2012). Cholesterol and its ability to assemble into Lo domains as well as the presence of a 3-OH group in the sterol structure was deemed instrumental for membrane invagination during clathrin-mediated endocytosis (Kim et al. 2017). These findings are also in line with the intrinsic negative curvature of the Cholesterol molecule imposed by its polar head group directing it to negatively curved membrane regions and the spontaneous negative curvature induction of lipid raft domains (Kollmitzer et al. 2013; Hyslop et al. 1990; Domanska and Setny 2024).

In this thesis, the influence of negative membrane curvature on Cholesterol domain recruitment was investigated by utilizing Gag^{CA3} (Kräusslich et al. 1995), a mutant that oligomerizes into flat domains at the PM but does not bend the cell membrane and therefore lacks both negative and positive membrane curvature at assembly sites. Gag^{CA3} did not colocalize with D4 signals which had a seemingly random distribution (**Figure 25**) indicating that the negative membrane curvature is necessary for lipid recruitment and further fortifying the hypothesis that the lipid ring domain is located at the Gag^{WT} bud neck. This finding was in line with the reports of Tomishige et al. of reduced D4/NT-Lys signal colocalization with Gag^{P99} and Gag^{EE}

curvature mutants compared to Gag^{WT} and a reduced propensity for D4 and NT-Lys labeled domains to coalesce (Tomishige et al. 2023). Furthermore, a study by Hogue et al. proposed that Gag-induced tetraspanin domain merging with lipid rafts was reduced in Gag curvature mutants compared to Gag^{WT} (Hogue et al. 2011). Sengupta et al. also described a lipid-based partitioning mechanism for protein inclusion or exclusion from the HIV-1 assembly sites that is amplified by membrane curvature (Sengupta et al. 2019).

Taken together, these studies, together with the data presented here, strongly suggest that outer leaflet PM Cholesterol/SM-rich domain recruitment to Gag assembly sites is highly dependent on negative membrane curvature generated by the budding process at the periphery of the forming Gag lattice i.e. in the neck of the bud. These highly ordered domains cluster to this region where they get trapped and form a mostly continuous, planar ring-shaped domain. These domains also likely aid in the induction of curvature or its maintenance, either via another cellular factor or on its own.

Ono et al. have shown that the reason for reduced particle release upon Cholesterol depletion is due to altered membrane binding and reduced higher order multimerization of Gag. They found that this can be overcame by fusing the Fyn Src kinase domain to the N-terminus of Gag which results in the restoration of particle release (Ono et al. 2007). This may indicate that lipid rafts may be more important for the initial phases of membrane attachment than for stabilization of the bud neck structure in the later phases. However it is uncertain if lipid depletion with MβCD abrogates the formation of the lipid ring-domain in the FynGag construct. Since Gag assembly drives the recruitment of lipids into a highly Cholesterol-enriched domain, the formation of the lipid ring may be occurring even at low PM Cholesterol levels. Testing if lipid recruitment occurs at FynGag sites even when Cholesterol is depleted may show if Cholesterol plays a role in stabilizing the membrane stalk connecting the VLP and the cell.

Additionally, lipid raft domains may aid in recruiting other cellular factors necessary for budding. Recently, one of the membrane bending I-BAR protein domains, insulin receptor substrate protein of 53 kDa (IRSp53), was identified as an important factor for HIV-1 budding completion (Inamdar et al. 2021). It localized to the borders of the Gag assembly sometimes encircling it and its knockdown resulted in virion bud arrest at half completion leading to drastic reduction in particle release. It would be interesting to explore if lipid domain recruitment and localization plays a

role in the function or recruitment of IRSp53 and vice versa and if IRSp53 alone is sufficient to enable virion budding if the lipid ring is destroyed. The utilization of the FynGag chimera might be useful in this regard as it could potentially provide a way to study IRSp53 in the absence of the lipid ring, if its formation is prevented by MβCD depletion.

4.7. Cholesterol- and SM-rich lipid domain formation at Gag sites is not necessary for Env-Gag co-clustering

Despite the loss of Cholesterol recruitment to Gag^{CA3} sites, Env punctate signals were readily detected highly colocalizing with Gag^{CA3} signals, indicating that neither recruitment of mEGFP-D4 labeled domains nor negative membrane curvature are essential for Env recruitment (**Figure 26**). Interestingly, at Gag^{CA3} sites Env did not form the characteristic extended ring-shaped domains at the borders of Gag sites but was overlapping with Gag^{CA3} signal to a much higher extent then with Gag^{WT}. These results are consistent with the findings of Pezeshkian et al., which showed that Gag^{P99} and Gag^{EE} curvature mutants retained the ability to confine Env close to that of Gag^{WT} (Pezeshkian et al. 2019). Additionally, Env localization was found to be closer to the center of the Gag signal in curvature mutants than in Gag^{WT} (Pezeshkian et al. 2019) indicating less prominent exclusion effect of the Gag lattice on Env.

My preliminary data (not shown) indicated a high level of correlation between integrated density of punctate Env and Gag^{CA3} signals measured at Gag^{CA3}-positive Env domains (Pearson correlation coefficient r=0.91 for N=47 assembly sites). Furthermore a mean signal intensity of Gag^{CA3}-associated Env was comparable to that of the Env ring at the border of Gag^{WT}, indicating similar Env concentration in the respective domains. Additionally, more than 80% of Gag^{CA3} sites colocalized with Env while Env colocalization with Gag^{CA3} was slightly lower. Together with the findings from Pezeshkian et al., this suggests that Env might be specifically enriched at Gag^{CA3} sites rather than undergoing free diffusion and stochastically incorporating into the assembly sites. A direct comparison of Gag^{CA3} colocalization with ΔCT-Env, which is known to randomly incorporate into assembly sites, and Env^{WT} might give more definitive results in this matter.

The observed difference of Env localization between Gag^{WT} (ring at Gag periphery) and Gag^{CA3} (punctate signal fully overlapping with Gag), might be

explained by the following considerations. Env is recruited in a Gag-dependent manner and trapped via interactions with Gag. In Gag^{WT}, the tight lattice organization prevents Env from freely diffusing over it and getting indiscriminately trapped by Gag-Env interactions, which leads to accumulation of Env predominantly at the Gag lattice periphery (**Figure 13**) where the lattice is growing and is more disordered. Gag^{CA3} lattice is likely less organized and less tightly packed which may enable Gag-Env interaction without steric hindrance ultimately leading to large amounts of Env localizing on top of the Gag lattice (**Figure 26**). However, despite neither curvature nor Cholesterol domain recruitment are necessary for Env recruitment and retention at the assembly site, either one or both together might act to limit Env mobility and trap it at the borders of the Gag lattice. Furthermore, steric lattice exclusion as well as curvature and/or lipid trapping are not mutually exclusive and might act together to restrict Env out of the Gag^{WT} but not out of the Gag^{CA3} lattice which has no curvature or lipid domains at its periphery but likely has a less dense lattice arrangement. It would be therefore interesting to explore the differences between Env CT localization and interactions with the Gag^{WT} lattice compared to the Gag^{CA3} lattice using cryo-electron microscopy as well as to explore curvature-dependent Env distribution and potential trapping in the absence of Gag as was previously done for ESCRT-III (Lee et al. 2015).

Taken together, these results suggest a model (**Figure 31**) where Gag membrane anchoring occurs at pre-existing lipid domains or where a rapid Cholesterol- and SM-rich punctate domain recruitment to the periphery of the Gag lattice occurs. Subsequently, punctate Cholesterol/SM-rich domains located in the outer leaflet of the PM are progressively recruited to the negatively curved regions at the periphery of the Gag lattice likely due to the specific preference of these lipids towards negatively curved regions. The lipid domains get trapped there and may facilitate further membrane curvature or stabilize it.

Recruitment of Env to the assembly site is governed by Gag oligomerization, and neither Cholesterol domain recruitment nor membrane curvature were shown to be necessary for it. Env exclusion from the majority of the Gag lattice may be a consequence of steric exclusion of the Env CT – as was argued before, however negative curvature and dense lipid domains at the neck of the bud may also act as a trap and a barrier for Env incorporation, despite not playing a role in its recruitment. These effects may act together to limit the incorporation of Env trimers throughout the entire HIV-1 assembly process. A part of the lipid domain is incorporated into the budding virion, likely because ESCRT-mediated scission occurs partly through this

domain, cutting it so that one portion is left in the cell PM and the other gets incorporated into the virion. Such lipid distribution in relation to the ESCRT scission localization may serve as a final barrier for Env incorporation during the last stages of assembly that may be especially important. This is because the Gag lattice is not a complete sphere and does not extend fully to the underside of the budding virion, and therefore is unable to limit Env incorporation from the proximal Env ring domain via steric exclusion alone.

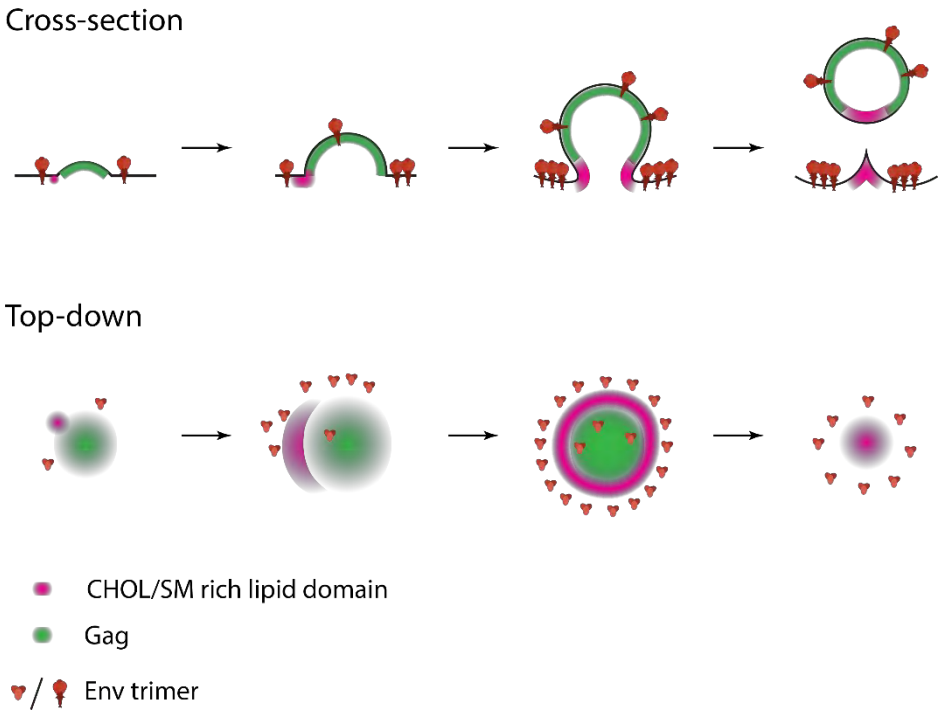

Figure 31. A model proposing Cholesterol- and SM-rich lipid domain distribution during assembly of HIV-1. The cross-section and the top-down view both show a progression of HIV-1 assembly, from left to right. First a recruitment of punctate Cholesterol/SM-rich lipid domains (magenta) to the border of the Gag lattice (green) occurs. Upon recruitment of multiple such domains, a ring-shaped domain at the border of the Gag lattice is formed in the membrane region with high negative curvature and largely overlaps with the extended ring-shaped Env domain. A portion of the lipid domain ultimately gets incorporated into the particle likely mediated by ESCRT membrane scission, possibly limiting Env incorporation by steric exclusion.

5. Conclusion

The goal of this PhD project was to establish a super-resolution lipid imaging approach in the context of HIV-1 assembly and apply it to resolve the lipid environment of individual assembly domains to a level that was previously not achieved in order to better understand the mechanisms of Cholesterol and SM virion enrichment. This work established new understanding of the dynamics of lipid raft recruitment which are in line with HIV-1 membrane composition studies, as well as of the mechanistic basis upon which HIV-1 may interact with lipids at the PM. My thesis highlights the importance of investigating lipids in the biogenesis of HIV-1 and other viruses as despite decades of research, many questions remain open and our understanding of the underlying processes is still incomplete.

Using the established native lipid labeling method in this work, a high level of co-localization between Cholesterol/SM-rich domains and HIV-1 assemblies was discovered. Furthermore, coalescence of Gag-associated, small punctate lipid domains into larger, ring-like domains that encircle Gag as the domain grows was observed. This lipid domain largely colocalized with Env however its influence on Env recruitment to the Gag domain was shown to be non-essential. Finally, Gag was established as the minimal viral component sufficient for lipid domain recruitment and coalescence, while the use of the membrane bending-defective Gag^{CA3} mutant revealed negative membrane curvature to be a defining factor in this process, but not essential for Env recruitment.

The techniques used in this work can be applied to study the budding of other viruses and cellular processes as well, which could answer more general questions regarding membrane organization and the process of budding as well as the role lipid rafts play in regulating membrane processes. With this PhD thesis, my work lays the foundation for new investigations of lipid raft involvement in viral budding and vesicle formation processes that depend on membrane curvature.

6. Materials and Methods

6.1. Materials

Table 1. Equipment and microscopy

Name	Company
C1000 Touch Thermal Cycler	BioRad, USA
Centrifuge 5417C	Eppendorf AG, Germany
Gel iX Imager	INTAS Science Imaging, Germany
LiCor Odyssey Imager	LiCor Bioscience, USA
Mercury Lamp H44GS- 100M; 100 Watt; PAR38	Sylvania, USA
Micro fluidizer LM10	Microfluidics Corporation, USA
NanoPhotometer	Implen, Germany
STED microscope 775 nm	Abberior Instruments GmbH, Germany
UltraView VoX spinning disc confocal microscope	PerkinElmer, USA

Table 2. Laboratory materials

Name	Company
Labtek, 8-well, Nunc	Thermo Fisher Scientific, USA
µ-Slide 15 Well 3D, ibiTreat	Ibidi GmbH, Germany
Wheaton glass vials 1.8 ml brown	neoLab, Germany
Amicon Ultra-15 10k MWCO centrifugal filters	Merck, Germany
Vivaspin 500 Centrifugal Concentrators 5k PES	Sartorius, Germany

Table 3. Kits

Name	Company
Qiagen Plasmid Plus Midi kit	Qiagen, Hilden
NucleoSpin Gel and PCR Clean-up	Macharay-Nagel, Germany
Click-iT Cell Reaction Buffer Kit	Lonza, Basel, Switzerland
Gibbson Assembly Master Mix	New England Biolabs, USA
BCA Protein Assay Kit	Thermo Fisher Scientific, USA
NucleoBond MaxiPrep Kit	Macherey-Nagel, Germany
Thrombin CleanCleave Kit	Sigma-Aldrich, USA

Table 4. Chemicals and reagents

Name	Company
Acrylamide (AA) 30%	AppliChem, GmbH, Germany
Agarose NEEO	Carl Roth, Germany
Ammonium persulfate (APS)	Sigma Aldrich, USA
BSA 100x	NEB, USA
cOmplete, EDTA-free Protease Inhibitor Cocktail	Hoffmann-La Roche, Switzerland
Coomassie brilliant blue G-250	Biomol Feinchemikalien, Germany
DMSO	Merck, Germany
DNA ladder 1 kb Plus	Thermo Scientific, USA
dNTP Set	Thermo Scientific, USA
Ethanol (99%) (EtOH), denatured	Zentralbereich INF, Germany
Fetal Calf Serum (FCS)	Biochrom, Germany
Gel Loading Dye, Purple (6x) for DNA	New England Biolabs, USA
Glycerol	Honeywell, Romania
Imidazole	Sigma-Aldrich, Germany
Isopropyl-b-D-thiogalactopyranoside (IPTG)	Sigma-Aldrich, USA
LI-COR Blocking Buffer (TBS)	LI-COR Bioscience, USA
β-Mercaptoethanol	Sigma-Aldrich, USA
N,N dimethylformamide (DMF), anhydrous	Sigma-Aldrich, USA
Triethylamine	Sigma-Aldrich, USA
TurboFect Transfection Reagent	Thermo Scientific, USA

Table 5. List of plasmids.

Plasmid	Note	Information
pCHIV Gag^{WT}	NL4-3 genome apart from Nef gene and LTRs in pcDNA3.1 backbone	(Lampe et al. 2007)
pCHIV Gag^{WT}.iCLIP	CHIV expression with CLIP-tagged Gag^{WT}	(Hanne et al. 2016)
pCHIV Gag^{WT}.iSNAP	CHIV expression with SNAP-tagged Gag^{WT}	(Eckhardt et al. 2011)
p-synGag	Codon optimized HIV-1 Gag	(Deml et al. 2001), MH*
p-synGag.iSNAP	synGag with SNAP domain	This thesis, MH*
pCHIV Gag^{CA3}	SP1 deletion in Gag	This thesis **
pCHIV Gag^{CA3}.iCLIP	Gag^{CA3} with a CLIP domain	This thesis
pET28b/His6-mEGFP.D4	Bacterial expression vector for mEGFP.D4	This thesis***
pET28b/His6-mEGFP.NT-Lys	Bacterial expression vector for mEGFP.NT-Lys	This thesis***

*Cloned by Moritz Hacke

** originally published in (Kräusslich et al. 1995)

*** Gift from Fabien Alpy (Wilhelm et al. 2019) originally from RIKEN, Japan, RDB13961, modified in this thesis to contain A206K mutation in EGFP

Table 6. Cell Culture media

Name	Medium	Supplements
DMEM	DMEM, high glucose (GIBCO)	10% FCS 20 mM HEPES 100 U/mL penicillin 100 ug/mL streptomycin
DMEM, delipidated	DMEM, high glucose (GIBCO)	10% delipidated FCS 20 mM HEPES 100 U/mL penicillin 100 ug/mL streptomycin
Opti-MEM	OptiMEM (GIBCO)	

Table 7. Bacterial culture media

Name	Component	Concentration
LB	NaCl	5 g/L
	Yeast extract	5 g/L
	Tryptone	10 g/L
	H_2O , adjusted to 7.2 pH	1 L

Table 8. List of antibodies and recombinant proteins

Antibody	Origin	Dilution
Human anti-HIV-1 gp120 (2G12)	Polymun Scientific, Klosterneuburg; Cat#AB002 RRID:AB_2661842	1:100 (IF STED)
Goat Anti-human Fab-STAR RED	This thesis	1:50 (IF STED)
Anti-human IgG (H+L)-unconj., Fab fragment (goat)	Jackson ImmunoResearch, USA; Cat# 109-007-003 RRID:AB_2337555	Used for coupling to STAR RED
anti-GFP VHH/ Nanobody (GFP Booster)-ATTO647N	Chromotech, Germany, Cat# gba647n	1:50 (IF STED)
anti-GFP VHH/ Nanobody (GFP Booster)-ATTO594	Chromotek, Germany, Cat# gba594	1:50 (IF STED)
Cholera Toxin Subunit B(Recombinant), Alexa Fluor 488 Conjugate	Thermo Fisher Scientific, USA; Cat# C34775	1 ug/mL
mEGFP.D4	This thesis	0.5 uM
mEGFP.NT-Lys	This thesis	0.5 uM
Sphingomyelinase from Bacillus cereus	Sigma-Aldrich, USA	2 mU/mL

Table 9. List of dyes and coupling reagents

Name	Origin
BC-NH_2	New England Biolabs, USA; Cat# S9236
ATTO 590-NHS	ATTO-TEC, Germany
ATTO 590-BC	This thesis
ATTO 647N-azide	ATTO-TEC, Germany
Abberior STAR RED-NHS	Abberior GmbH, Germany
SNAP Cell 647-SiR	New England Biolabs, USA; Cat# S9102S
Filipin III ready-made solution	Sigma-Aldrich, USA
Hoechst 33342	Thermo Fisher Scientific, USA

Table 10. List of software

Name	Source
FIJI	(Schindelin et al. 2012); RRID:SCR_002285
GraphPad Prism 8	GraphPad Software, Inc., La Jolla, USA; RRID:SCR_002798
Adobe Illustrator	Adobe Inc., 2021; Retrieved from https://adobe.com/products/illustrator; RRID:SCR_010279
Python	www.python.org; RRID:SCR_008394
Jupyter Notebooks	(Kluyver et al. 2016); RRID:SCR_018315
Volocity	Perkin Elmer, Waltham, USA; RRID:SCR_002668
ImSpector	Abberior Instruments GmbH, Göttingen; RRID:SCR_015249
Microsoft Excel	Microsoft, Redmond, USA
BioRender	Used at BioRender.com; RRID:SCR_018361

6.2. Reagents, plasmids, and cloning

All reagents were purchased from commercial sources unless specified otherwise. Synthesis of BC-ATTO590 was performed as previously described (Bottanelli et al., 2016). Briefly, NHS-ATTO590 (1.0 mg, 1.3 µmol, 1 equivalent) was dissolved in DMF. Subsequently, triethylamine (0.9 µL, 6.5 µmol, 5 equivalents) and benzylcytosine-amine (BC-NH2, 1.19 mg, 5.2 µmol, 4 equivalents) were added and the reaction mixture was stirred for 8h protected from light at room temperature. Subsequently the mixture was purified using RP-HPLC and the identified compound was obtained from reduced-pressure evaporated HPLC fractions. The purified BC-ATTO590 was dissolved in DMSO and titration experiments were performed to determine optimal labeling conditions.

The plasmid pCHIV and its derivatives where iCLIP or iSNAP tags are inserted between the MA and CA domains of Gag were previously described (Lampe et al., 2007; Eckhardt et al., 2011; Hanne et al., 2016). Transfection with pCHIV enables CMV-driven expression of all HIV-1 NL4-3 proteins except for Nef leading to the assembly, budding and egress of HIV-1 virus-like particles. The produced particles are entry competent but due to the lacking LTR sequences in the plasmid, integration is defective and the transfection of the plasmid results in a single replication cycle thus enabling the study of HIV-1 under biosafety level 1 conditions (BSL-1).

The codon optimized synthetic Gag (synGag) construct was also described previously (L Deml; 2000). A SNAP-tagged synGag was generated by Moritz Hacke using PCR amplification of the original construct using the forward primer 5'-TATAgctagc ATGGGCGCCAG-3' and reverse primer 5'-TATAgaattcCTGGCTGCTGGGGTC-3'. The amplified synGag gene was subsequently inserted into the pSNAPf vector (NEB, N9183S) using the NheI and EcoRI restriction sites. The pSNAPf vector was additionally modified by insertion of a DYKDDDK-tag using an annealed oligo (5'-TATAggatccGCCGCCAACGACATCCTGGACTACAAGGACGACGACGACAA GtaatgactcgagTATA-3'; 3'-TATActcgagtcattaCTTGTCGTCGTCGTCCTTGTAGTC CAGGATGTCGTTGGCGGCggatccTATA - 5') which was inserted using XhoI and BamHI restriction sites.

The budding defective HIV-1 variant, pCHIVCA3.iCLIP with the deletion of the entire SP1 region between CA and NC (amino acids AEAMSQVTNPATIM) was prepared by single-step site directed PCR mutagenesis (Liu et al., 2008) of pCHIViCLIP using forward primer 5'-AGAGTTTTGATACAGAAAGGCAATTTTA

GGAACCAAAGAAAG-3’ and reverse primer 5’-TTTCTGTATCAAAACTCTTG CTTTATGGCCGG-3’.

The plasmid pET28b His6-mEGFP.D4 encoding the complete sequence of PFO-D4 N-terminally fused with EGFP was a generous gift from Fabian Alpy (Wilhelm et al., 2021). Using site-directed mutagenesis I introduced a single A206K mutation into EGFP by PCR with forward 5’-CAGTCCAAACTGAGCAAAG ACCCCAACGAG-3’ and reverse 5’-CTCAGTTTGGACTGGGTGCTCAGGTA GTG-3’ primers to eliminate possible EGFP multimerization artifacts (Zacharias et al., 2002).

To generate the mEGFP.NT-Lys probe, the full NT-Lysenin gene (amino acids 167-297 of WT Lysenin) together with necessary overlap segments for later Gibson cloning was synthesized (Integrated DNA Technologies, USA). D4 gene was then excised from the pET28b-mEGFP.D4 construct via PCR using forward 5’-gaagtggttggttaaACTAAAGTAAAAACTGATTTTAGCTAG-3’ and reverse 5’-tttac caaggattatGCTAGCCTTGTACAGCTC-3’ primers. The synthesized NT-Lys gene was inserted into the resulting backbone using Gibson assembly (New England Biolabs, USA). Plasmid sequences were confirmed by sequencing (Microsynth Seqlab GmbH, Germany).

6.3. Transformations

50 µL of chemically competent bacteria were thawed on ice for 10 minutes and gently combined with 2 µL (10-150 ng) of the plasmid, 5 µL of the site-directed mutagenesis PCR product, or 2 µL of the ligation reaction. The mixture was incubated at 4°C for 10 minutes, followed by a 45-second heat shock at 37°C. The cells were immediately cooled on ice for 2 minutes, after which 400 µL of LB medium was added, and the mixture was incubated at 37°C for 45 minutes. Then, 50 µL of the transformed sample, either from the ligation or PCR reaction, or 50 µL of the retransformation sample, were plated onto selective agar and incubated at 37°C for 16 hours.

6.4. PCR reactions

Polymerase chain reaction (PCR) was carried out using specifically designed primers to generate new DNA fragments with flanking restriction sites (standard PCR) or for site-directed mutagenesis (sdm). The protocol followed the manufacturer's instructions for Q5® High-Fidelity DNA Polymerase (NEB, Ipswich, US). After PCR, the samples were treated with 1 µL of DpnI per 50 µL reaction for 1

hour to digest the parental DNA. If needed, the PCR products were purified following the NucleoSpin Gel and PCR Clean-up protocol (Macherey-Nagel, Düren, Germany).

6.5. Agarose gel electrophoresis

Agarose gel electrophoresis was used to separate DNA fragments by size. To prepare gels, 1% (w/v) agarose powder was dissolved in TAE buffer by heating, and 4 µL of Midori Green was added per 40 mL of the agarose solution for DNA staining. The solution was poured into a horizontal gel chamber, and a comb was inserted to create wells for the samples. Once the gel solidified, DNA samples mixed with 6x loading dye were loaded into the gel. A 4 µL sample of the 1 kb Plus DNA ladder was also added as a size standard. The gel was run at 90 V for 45 minutes in 1x TAE buffer. Finally, the gel was documented using the Gel iX Imager (INTAS Science Imaging, Göttingen, Germany).

6.6. Protein expression and purification

Plasmid DNA was transformed into E. coli Rosetta (DE3) (One Shot™ BL21(DE3), Invitrogen) by heat-shock and a single clone was grown in LB containing 50 µg/mL kanamycin. The overnight culture was diluted to OD600 of 0.05 and grown at 37°C until OD600 of 0.7. Cultures were subsequently cooled to 18°C and induced with 0.5mM IPTG for 8h at 18°C for protein expression.

Bacterial pellets from 4-L cultures (~12 g) were resuspended in 70 mL Lysis Buffer (50 mM NaH2PO4/Na2HPO4, pH = 8.0, 300 mM NaCl, 10 mM imidazole) and lysed with two passes on a cell fluidizer (Micro fluidizer LM10, Microfluidics Corporation, Newton, USA) at 15000 psi. The resulting lysate was cleared at 12000 x g for 1.5h at 4°C after which the His-tagged proteins were purified using IMAC Ni-NTA resin (Qiagen, Germany) in batch mode. Specifically, cleared lysate was incubated shaking for 40 min at room temperature with 3 mL Ni-NTA agarose resin that had been equilibrated with Lysis Buffer according to manufacturer's instructions. The resin was washed three times with 15 mL of Lysis Buffer adjusted to 25 mM imidazole and applied to an empty column to drain the wash. The proteins were eluted with 15 mL Elution Buffer (50 mM NaH2PO4/Na2HPO4, pH = 8.0, 300 mM NaCl, 250 mM imidazole). Buffer exchange and protein concentration was done until 1.5 mg/mL final protein concentration into Cleavage Buffer (50 mM NaH2PO4/Na2HPO4, pH = 8.0, 10 mM CaCl2, 200 mM NaCl) using 10 kDa MWCO ultrafiltration units (Amicon® Ultra Centrifugal Filter, Milipore) Cleavage of His6-tag

from purified proteins was performed for 4h at room temperature while shaking with 200 µL thrombin-bound resin (Thrombin CleanCleave Kit, Sigma)/1 mg protein at 1 mg/mL protein concentration. Eluate was collected after transferring the mixture into an empty column along with three subsequent washes with Cleavage Buffer. Another step of ultrafiltration centrifugation was performed as before to concentrate the final purified proteins to 1 mg/mL in Storage Buffer (20 mM NaH_2PO_4/Na_2HPO_4, pH = 7.4) and subsequently adjusted to 20% glycerol (v/v) and stored at -20°C until used.

6.7. Cell culture

HeLa Kyoto cells (RRID:CVCL_1922) were cultured at 37°C and 5% CO_2 in Dulbecco's modified Eagle's medium (DMEM; Invitrogen) supplemented with 10% fetal bovine serum (FBS-11A; Capricorn Scientific) containing 100 µg/mL streptomycin and 100 U/mL penicillin. Cell line identity was confirmed through STR profiling using the Promega PowerPlex 21 Kit by Eurofins Genomics. The cell lines were cultured from liquid nitrogen stocks ensured to be free of mycoplasma. Passaged cells were regularly monitored for mycoplasma contamination, employing the MycoAlert mycoplasma detection kit (Lonza Rockland, USA). Cell lines utilized in this study were confirmed to be free from contamination.

6.8. Cholesterol and Sphingomyelin staining protocol

60-70% confluent HeLa Kyoto cells seeded the previous day were incubated with 0.5 µM mEGFP.D4 (Cholesterol) or mEGFP.NT-Lys (SM) in serum-free DMEM for 10 min at room temperature. Cells were washed three times with PBS, fixed for 12 min with 3.7% PFA and kept at 4°C for up to one day until imaging.

6.9. pCHIV transfection

Cells were seeded in 15-well µ-Slide Angiogenesis dishes (ibidi, Germany) at 3300 cells/50 µL well. The next day, transfection mixture was prepared by mixing 1 µg pCHIViCLIP with 1 µg pCHIV in 200 µL Opti-MEM (Gibco, USA) reduced serum medium after which 4.7 µL of TurboFect (Thermo Fisher Scientific, USA) was added and incubated up to 1h at room temperature. Cells at 50-60% confluency were incubated for 6h with 50 µL mixture comprising of 10 µL DNA-containing transfection mix and 40 µL DMEM (0.1 µg DNA/well final concentration) supplemented with 10% FBS, followed by a medium change to complete growth medium 6 hours post transfection.

6.10. Lipid depletion from the PM of cells

HeLa cells were seeded on µ-Slide Angiogenesis dishes (ibidi, Germany) and the next day treated for 30 min at 37°C with freshly prepared 10 mM MβCD (Sigma-Aldrich, USA) in serum free DMEM. Alternatively, for SM depletion, cells were incubated with 2 mU/mL SM-ase (SM-ase from Bacillus c., Sigma-Aldrich, USA) in 0.5% BSA/PBS for 1h at 37°C. After washing, cells were stained with mEGFP.D4 or mEGFP.NT-Lys and fixed as described above. In addition to mEGFP.D4 staining, Cholesterol depletion was additionally assessed by staining with Filipin III ready-made solution (Sigma-Aldrich, USA) at a final concentration of 0.05 mg/mL in PBS for 2h at room temperature. Filipin was imaged by excitation at 405 nm. Nuclear staining in samples stained with mEGFP.D4 were performed as a last step with SiR-DNA (Spirochrome, Switzerland) (G. Lukinavicius et al.,SiR–Hoechst,2015) at a final concentration of 1 µM for 30 min at room temperature and imaged by excitation at 647 nm. Nuclear staining in samples stained with mEGFP.NT-Lys was performed as a last step with Hoechst nuclear dye (Hoechst 33342, Thermo Fisher Scientific, USA) at final concentration of 0.2 µg/mL for 15 min at room temperature.

6.11. Lipid depletion quantification

HeLa cells stained with Filipin III, mEGFP.D4 or mEGFP.NT-Lys were imaged using a spinning disc confocal microscope as described in the Microscopy section below. For quantification of total cell fluorescence, the first 18 z-slices (0.4 µm step size) starting from the bottom of cells were combined into a sum projection image which was further used in analysis. Average background signal was calculated from 3 random, non-cell areas in each FOV and subtracted from the corresponding image. Cell borders were manually traced and integrated density (product of pixel area and mean gray value of said area) was calculated for each cell. Integrated density was normalized to the mean of untreated samples. The complete analysis was performed using the Fiji software (RRID:SCR_002285) (Schindelin et al., 2012).

6.12. Sample preparation for STED microscopy

Gag.iCLIP in transfected cells was stained 14h post transfection with 3 µM BC-ATTO590 (in house), or SNAP Cell 647-SiR (New England Biolabs, USA) in the case of synGag.iSNAP, in DMEM for 45 min at 37°C. Cells were washed 3 times for 15 min with fresh DMEM and subsequently stained with mEGFP.D4 or mEGFP.NT-Lys as described above. After fixation and washing, cells were blocked with 3% BSA/PBS for 1h at room temperature in the dark. To enable STED detection of D4

and NT-Lys, cells were incubated for 1h at room temperature with 1:100 dilution of an anti-GFP nanobody (GFP-Booster, Chromotek) coupled to either ATTO647N or ATTO594 (in synGag.iSNAP experiments) in 0.5% BSA/PBS and subsequently washed three times for 10 min. Subsequently, Env was stained for 2h at room temperature with 1:100 human anti-2G12 gp120 (Polymun Scientific, RRID:AB_2661842) followed by 1h at room temperature with 1:50 Goat Anti-Human Fab IgG (H+L) (Jackson ImmunoResearch Labs, RRID:AB_2337555) coupled to ATTO594 or STAR RED (Abberior Instruments GmbH, Germany). After washing, cells were stored in 50% (v/v) glycerol/PBS before imaging.

6.13. Microscopy

Confocal microscopy was performed on PerkinElmer UltraVIEW VoX SDC microscope (Perkin Elmer, Waltham, USA) employing a 60x Apo TIRF (NA 1.49) oil immersion objective and a Hamamatsu C9100-23B EM-CCD camera for imaging. Filipin III and Hoechst nuclear dye were excited at 405 nm, mEGFP at 488 nm, and SiR-DNA at 640 nm. STED microscopy was done on a commercial system (Abberior Instruments GmbH, Göttingen, Germany) using a 775 nm depletion laser, 100 x Olympus UPlanSApo (NA 1.4) oil immersion objective with 590 and 640 nm excitation laser lines at room temperature. Nominal STED laser power was set to 10%-60% of the maximal power of 1200 mW with 10-14 µs pixel dwell time and 15 nm pixel size as a sampling rate.

Representative STED images were deconvolved using Richardson-Lucy algorithm in the software Imspector (Abberior Instruments GmbH, Göttingen, Germany) with a regularization parameter of 1 x 10-8 and maximum of thirty iterations using a calculated 50 nm lateral Lorentzian PSF:

$$a = 50 * 10^{-9} \quad ; \quad \frac{(0.5*a)^2}{(x-x_0-\frac{x}{2})^2+(y-y_0-\frac{y}{2})^2+(0.5*a)^2}$$

Images were additionally adjusted for optimal brightness and contrast using Fiji software (RRID:SCR_002285) (Schindelin et al., 2012).

6.14. Average radial intensity profile analysis

To automate line profile analysis, I adapted a Python script, originally developed by Thorsten G. Müller and Svenja Nopper in our lab, to acquire an average radial intensity profile by averaging concentric circle areas of pixels, suited to the radial symmetry of an HIV-1 assembly. Briefly, the script first performed

automated segmentation (based on Otsu's method thresholding (Otsu, 1979) of all Gag signals which were then manually corrected to exclude out of focus signals and signals in close proximity to each other. The centroid of every assembly was determined programmatically. The four nearest pixels represented the first ring area, and subsequent concentric ring layers were defined with an increment of 1 pixel. Intensities for each channel were averaged for each individual ring area to create an average radial profile starting at the center of assembly and ending at its periphery. Since the STED system used here has a pixel size of 15 nm, the 11 areas included in the profile (0 to 10) range from 0 nm (centroid) to 150 nm (assembly periphery). The line in the profile represents the mean of the selected assemblies at specified distance from the Gag center while the shaded area includes the 95% confidence interval of the mean. Data were normalized for both channels individually by the highest mean of the respective set. In case of ring profiling where only assemblies with full D4 or NT-Lys ring domains were of interest, all other assemblies were removed from segmentation manually. Alternatively, when GagCA3 was analyzed for co-occurrence with D4 or Env, the segmentation was corrected to include small (~50-120nm) or large assemblies (> 200nm) separately with no regard for lipid probe channel.

6.15. 2D projection illustrations from 3D objects

All the 2D projections in **Figure 29** were made in Adobe Illustrator. The projection of a sphere object was generated by setting a linear radial gradient from the edge of the circle (100% opacity) to the center (50% opacity). This is based on the difference between the 3D surface area of the sphere and its 2D projection (i.e. shadow) depending on the distance from the pole (pole vs equator), assuming an even distribution of fluorophores over the surface of the sphere. Specifically, the 3D surface area of a region at the equator is roughly two times larger than its 2D projection area, while the same sized 3D region at the pole of the sphere is roughly the same size as its 2D projection area which is defined by the following:

Total surface of a sphere with a radius R:

$$A_{sphere} = 4\pi R^2$$

All coordinates of a sphere can be described with a polar angle θ and azimuthal angle ϕ as depicted in **Figure 32**.

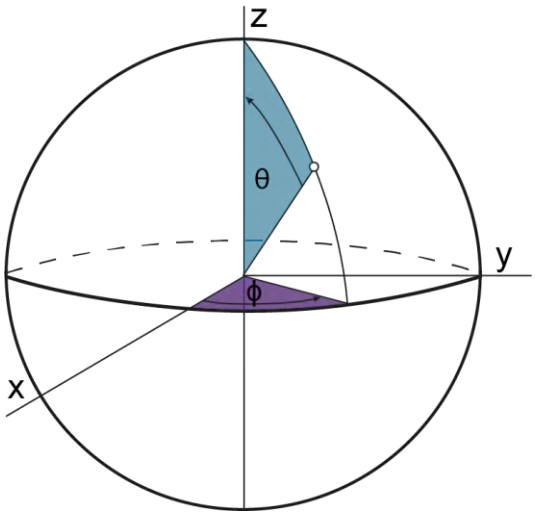

Figure 32. Schematic of a sphere with polar (θ) and azimuthal (ϕ) angles depicted. The x,y and z axis intersect at the origin of the sphere. The white dot is the coordinate on the surface of the sphere defined by the polar angle θ (blue) and azimuthal angle ϕ (purple).

For any region on the surface of the sphere, the infinitely small element in spherical coordinates with a polar angle θ and azimuthal angle ϕ is:

$$dA_{real} = R^2 \sin(\theta) d\theta d\phi$$

where θ = 0 at the pole and θ = π/2 at the equator, and the azimuthal angle ϕ ranges from 0 to 2π.

Total surface area of a sphere cap, from the pole to any angle θ is:

$$dA_{real}(\theta) = 2\pi R^2 (1 - \cos\theta)$$

For an infinitely small element, the projected area $dA_{projected}$ is related to the real area by the cosine of the polar angle:

$$dA_{projected}(\theta) = R^2 \sin(\theta) cos(\theta) d\theta d\phi$$

To find the total projected area from the pole to any angle θ, the infinitely small element can be integrated and for the full azimuthal range (0 to 2π) this becomes:

$$A_{projected}(\theta) = 2\pi R^2 \int_0^{\theta} \sin(\theta')\cos(\theta')d\theta'$$

$$A_{projected}(\theta) = \frac{\pi R^2}{2} sin^2(\theta)$$

From that, the relation between the area of a projected image to the real surface of the sphere can be formulated as:

$$\frac{A_{projected}(\theta)}{A_{real}(\theta)} = \frac{sin^2(\theta)}{2(1-\cos(\theta))}$$

If this ratio is plotted from the pole to the equator, we can see that it is half as large at the equator compared to the pole (**Figure 33**). This means that the 3D surface area at the equator is twice the size of the 2D projected area on the circle periphery, while at the pole this ratio is 1:1. Thus, assuming an even fluorophore distribution and an ideal model, two times more fluorophores would be projected onto a unit of 2D area (detector region) at the equator then at the pole, making it twice as bright.

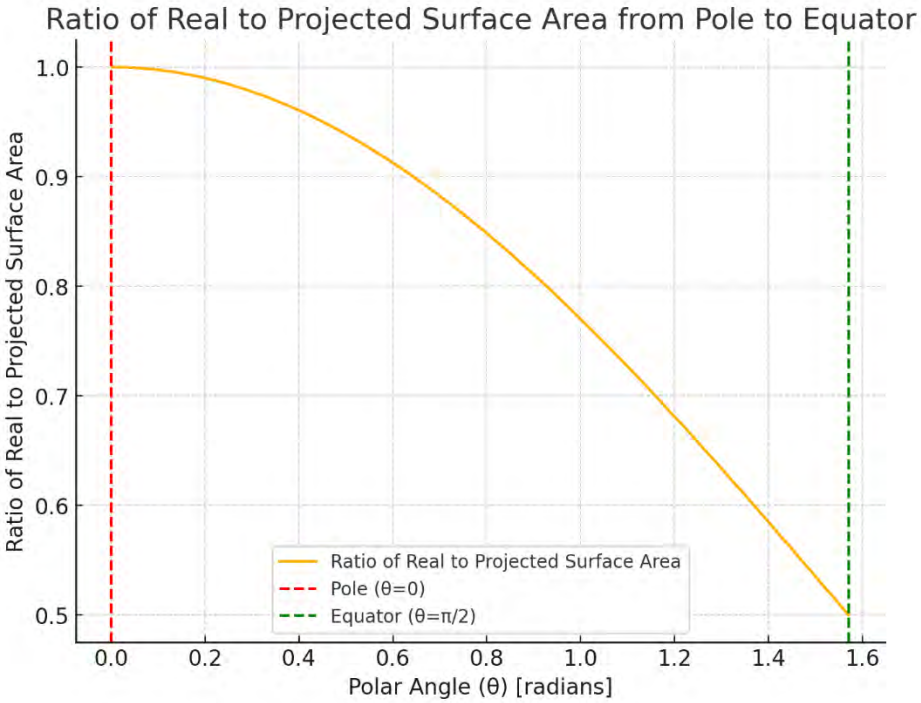

Figure 33. Graph of the ratio of real surface area (3D) vs projected surface area (2D) depending on the position relative to the pole and equator of the sphere. The polar angle of θ=0 represents the sphere pole (red dotted line), while the angle θ=π/2 represents the equator (green dotted line).

The brightness of the hemisphere projection (**Figure 29**, object 2) was set to be 50% of the sphere projection by duplicating the sphere projection object and setting its opacity to 50%. The intensity of the planar ring object projection (**Figure 29**, object 3) was taken arbitrarily (50% opacity) with no consideration what relation in brightness it would have compared to the sphere and hemisphere. To simulate the effects of the PSF-induced image convolution, a Gaussian filter (9px) was applied while the diameter of the sphere/hemisphere was 55 px.

6.16. Statistical analysis

All statistical analysis was done in GraphPad Prism (GraphPad Software, Inc., La Jolla, USA; RRID:SCR_002798). Statistical difference between groups in **Figure 23 B** was assessed by one-way ANOVA with Kruskal-Wallis post hoc test.

7. Acknowledgements

First, I would like to thank Prof. Hans-Georg Kräusslich for entrusting me with this project and for giving me an opportunity to become a scientist. Your guidance, insightful discussions, and patience have been invaluable, and your ability to foster independence while steering me in the right direction has profoundly shaped how I think critically and approach research. My heartfelt thanks to Prof. Barbara Müller for her invaluable lessons in scientific writing and research practice. Your feedback and ideas greatly enhanced this project, and your dedication to reviewing its content is deeply appreciated.

I would like to thank Prof. Britta Brügger, for being a second examiner of this work and for being a wonderful, insightful TAC member that brought knowledge and ideas from a different perspective. I am also grateful to Prof. Friedrich Frischknecht and Marco Binder for their flexibility and for generously agreeing to examine this work.

To Doris Höglinger, thank you for being an uplifting presence in the TAC meetings. Your positivity, fresh ideas, and thoughtful discussions made me feel both understood and encouraged. Great many thanks to Vibor Laketa for joining my TAC and introducing me to the wonderful world of microscopy. Thank you for all your time, ideas and discussions and for a piece of home in an unfamiliar place.

I am especially grateful to Frauke Mücksch for amazing communication from the first day and enormous help in easing my first days of employment. It was a pleasure to learn from you and continue working on your project. Thank you for all the advice and contributions you made to this work

Thank you Anke, Vera and Maria for all the help with experiments, advice and your care– it was always lovely to share a lab with you and to learn from you! Thank you Jian for being an amazing lab-mate, for all the support in the difficult moments and for the companionship!

Robine and Anja, living with you was one of the highlights of this journey! Thank you for your continuous support both in and out of the lab and for enriching my life with yours! Robine, your immeasurable inappropriateness is infinitely funny — thank you for being always so cheerful and for making the most amazing bread and lángos! Anja, thank you for all the wonderful bouldering times, evening discussions, all the advice and endless laughter!

To my dearest rodjas, Tamara, Mia and Sandra, thank you for your amazing friendship, for sharing this road with me and your endless support! Thank you for all the lunches, coffees laughs and adventures, for all the drinks and for the spark you brought to CIID! Tamara, thank you for all the words of encouragement, all the technical help and making sure I didn't forget how to speak Serbian. Uspeli smo rodjo!

Maike, you are one of the coolest and sweetest people I have ever met! Thank you for all the trips, lunches and dinners, all the "hate" and love and for making Heidelberg a better place!

Moritz thank you for all the coffees and lunches, for helping out whenever I asked, for bringing energy and fun when it was sorely lacking, and for the most silly conversations that I've had. Your drive is inspiring and made the last push much easier!

Dear Philippe, your unyielding will to climb and push the boundaries has always inspired me! Thank you for all the amazing adventures we had, that lifted me up when I was down!

Dear bouldering/climbing friends – Zoe and Yannik, Sophie and Dimitris, Terra and Nic, Nils and Hanna, Theo and Lorry – thank you for your uplifting company through the most valuable outlet I've found during my stay in Heidelberg. The moments I spent with all of you have made my life so much richer and more beautiful – I only wish we had met sooner!

Thorsten, thank you for being my second mentor! Thank you for introducing me to climbing and for being the best climbing buddy anyone could wish for! You taught me everything I know and I enjoyed every battle we fought together! Thank you for all the lunches, beers and the parties, all the adventures and all the trust! Thank you for pushing me when I needed it, and for pulling me back when I had too much. Thank you for inspiring me both in and out of the lab and thank you for your undeniably bad humor!

Тамара, Милоше и Вуче – било је задовољство студирати са вама и бити у вашим животима, па макар и из даљине. Хвала вам на подршци и феноменалном другарству кроз све ове године!

Неле, твоја енергија, таленат и доброта су ми били једна од највећих инспирација у животу. Хвала што си ми прави велики брат, што си ми заувек променио живот дајући ми твоју гитару и посветио ми своје време без икакве задршке, са пуно радости, увек и безусловно! Хвала ти на свему!

Марко и Лука, од када знам за себе били смо екипа. Хвала вам на деценијама непроцењивих искустава, подршке и доживљаја које нећу заборавити до краја живота. Хвала вам на небројеним ноћима и данима кроз које смо одрастали и постали као породица. Хвала вам што ми нисте дозволили да заборавим своје корене, на свим саветима, искреном другарству и поузданости — на вас сам увек могао да рачунам и увек ћу моћи.

Владана и Милане, хвала вам на гостопримству, на поверењу и на невероватној прилици да учим од вас. Ви сте били одскочна даска у мом новом животу и заувек сам вам за то захвалан.

Гаго и Владо, хвала вам на свему! Од нових искустава до непрекидне подршке и интереса за мој живот. Без обзира на даљину, увек сте ми били близу!

Мама и тата, не постоје речи које могу да изразе моју захвалност. Без ваше безусловне љубави и подршке ништа од овога не би било могуће. Хвала вам што никада нисте направили грешку, што сте увек били на мојој страни и што сам вам увек био на првом месту. Хвала вам што сте се жртвовали и борили се за моју будућност и срећу. Ви сте увек били и увек ћете бити моји хероји и мој најпоузданији ослонац у свету лудила и несигурности. Хвала вам што сте ми били најбољи пријатељи од како знам за себе — да сам могао да бирам родитеље, изабрао бих вас!

Zina, this PhD brought many findings, but none of them nearly as valuable as you. You made everything easy and gave it purpose. Thank you for your positivity and support, your constant love and kindness. Thank you for the stability and companionship, and all the lovely days we spent in our first home in Heidelberg and many other places. Thank you for trusting me, with your heart and your life. Thank you for lifting me up when I was down and for joining me in marriage and in life!

8. Publication bibliography

Abe, M.; Makino, A.; Hullin-Matsuda, F.; Kamijo, K.; Ohno-Iwashita, Y.; Hanada, K.; Mizuno, H.; Miyawaki, A.; Kobayashi, T. (2012): A role for sphingomyelin-rich lipid domains in the accumulation of phosphatidylinositol-4,5-bisphosphate to the cleavage furrow during cytokinesis. In *Molecular and cellular biology* 32 (8), pp. 1396–1407. DOI: 10.1128/MCB.06113-11.

Ahmed, S. N.; Brown, D. A.; London, E. (1997): On the origin of sphingolipid/cholesterol-rich detergent-insoluble cell membranes: physiological concentrations of cholesterol and sphingolipid induce formation of a detergent-insoluble, liquid-ordered lipid phase in model membranes. In *Biochemistry* 36 (36), pp. 10944–10953. DOI: 10.1021/bi971167g.

Alfadhli, A.; McNett, H.; Tsagli, S.; Bächinger, H. P.; Peyton, D. H.; Barklis, E. (2011): HIV-1 matrix protein binding to RNA. In *Journal of molecular biology* 410 (4), pp. 653–666. DOI: 10.1016/j.jmb.2011.04.063.

Alfadhli, A.; Staubus, A. O.; Tedbury, P. R.; Novikova, M.; Freed, E. O.; Barklis, E. (2019): Analysis of HIV-1 Matrix-Envelope Cytoplasmic Tail Interactions. In *Journal of virology* 93 (21). DOI: 10.1128/JVI.01079-19.

Alfadhli, A.; Still, A.; Barklis, E. (2009): Analysis of human immunodeficiency virus type 1 matrix binding to membranes and nucleic acids. In *Journal of virology* 83 (23), pp. 12196–12203. DOI: 10.1128/JVI.01197-09.

Aloia, R. C.; Jensen, F. C.; Curtain, C. C.; Mobley, P. W.; Gordon, L. M. (1988): Lipid composition and fluidity of the human immunodeficiency virus. In *Proceedings of the National Academy of Sciences of the United States of America* 85 (3), pp. 900–904. DOI: 10.1073/pnas.85.3.900.

Aloia, R. C.; Tian, H.; Jensen, F. C. (1993): Lipid composition and fluidity of the human immunodeficiency virus envelope and host cell plasma membranes. In *Proceedings of the National Academy of Sciences of the United States of America* 90 (11), pp. 5181–5185. DOI: 10.1073/pnas.90.11.5181.

Alpy, F.; Stoeckel, M. E.; Dierich, A.; Escola, J. M.; Wendling, C.; Chenard, M. P.; Vanier, M. T.; Gruenberg, J.; Tomasetto, C.; Rio, M. C. (2001): The steroidogenic acute regulatory protein homolog MLN64, a late endosomal cholesterol-binding protein. In *The Journal of biological chemistry* 276 (6), pp. 4261–4269. DOI: 10.1074/jbc.M006279200.

Anderson, H. A.; Chen, Y.; Norkin, L. C. (1996): Bound simian virus 40 translocates to caveolin-enriched membrane domains, and its entry is inhibited by drugs that selectively disrupt caveolae. In *Molecular biology of the cell* 7 (11), pp. 1825–1834. DOI: 10.1091/mbc.7.11.1825.

Anderson, R. G. (1998): The caveolae membrane system. In *Annual review of biochemistry* 67, pp. 199–225. DOI: 10.1146/annurev.biochem.67.1.199.

Appen, A. von; Kosinski, J.; Sparks, L.; Ori, A.; DiGuilio, A. L.; Vollmer, B.; Mackmull, M.-T.; Banterle, N.; Parca, L.; Kastritis, P.; Buczak, K.; Mosalaganti, S.; Hagen, W. et al. (2015): In situ structural analysis of the human nuclear pore complex. In *Nature* 526 (7571), pp. 140–143. DOI: 10.1038/nature15381.

Arni, S.; Ilangumaran, S.; van Echten-Deckert, G.; Sandhoff, K.; Poincelet, M.; Briol, A.; Rungger-Brändle, E.; Hoessli, D. C. (1996): Differential regulation of Src-family protein tyrosine kinases in GPI domains of T lymphocyte plasma membranes. In *Biochemical and biophysical research communications* 225 (3), pp. 801–807. DOI: 10.1006/bbrc.1996.1254.

Arthur, J. R.; Heinecke, K. A.; Seyfried, T. N. (2011): Filipin recognizes both GM1 and cholesterol in GM1 gangliosidosis mouse brain. In *Journal of lipid research* 52 (7), pp. 1345–1351. DOI: 10.1194/jlr.M012633.

Arthur, L. O.; Bess, J. W.; Sowder, R. C.; Benveniste, R. E.; Mann, D. L.; Chermann, J. C.; Henderson, L. E. (1992): Cellular proteins bound to immunodeficiency viruses: implications for pathogenesis and vaccines. In *Science (New York, N.Y.)* 258 (5090), pp. 1935–1938. DOI: 10.1126/science.1470916.

Awadh, A. A. (2023): The Role of Cytosolic Lipid Droplets in Hepatitis C Virus Replication, Assembly, and Release. In *BioMed research international* 2023, p. 5156601. DOI: 10.1155/2023/5156601.

Balla, T. (2013): Phosphoinositides: tiny lipids with giant impact on cell regulation. In *Physiological reviews* 93 (3), pp. 1019–1137. DOI: 10.1152/physrev.00028.2012.

Baltimore, D. (1971): Expression of animal virus genomes. In *Bacteriological Reviews* 35 (3), pp. 235–241. DOI: 10.1128/br.35.3.235-241.1971.

Barré-Sinoussi, F.; Chermann, J. C.; Rey, F.; Nugeyre, M. T.; Chamaret, S.; Gruest, J.; Dauguet, C.; Axler-Blin, C.; Vézinet-Brun, F.; Rouzioux, C.; Rozenbaum, W.; Montagnier, L. (1983): Isolation of a T-lymphotropic retrovirus

from a patient at risk for acquired immune deficiency syndrome (AIDS). In *Science (New York, N.Y.)* 220 (4599), pp. 868–871. DOI: 10.1126/science.6189183.

Bartenschlager, R.; Penin, F.; Lohmann, V.; André, P. (2011): Assembly of infectious hepatitis C virus particles. In *Trends in microbiology* 19 (2), pp. 95–103. DOI: 10.1016/j.tim.2010.11.005.

Batonick, M.; Favre, M.; Boge, M.; Spearman, P.; Höning, S.; Thali, M. (2005): Interaction of HIV-1 Gag with the clathrin-associated adaptor AP-2. In *Virology* 342 (2), pp. 190–200. DOI: 10.1016/j.virol.2005.08.001.

Baumgart, T.; Hunt, G.; Farkas, E. R.; Webb, W. W.; Feigenson, G. W. (2007): Fluorescence probe partitioning between Lo/Ld phases in lipid membranes. In *Biochimica et biophysica acta* 1768 (9), pp. 2182–2194. DOI: 10.1016/j.bbamem.2007.05.012.

Belov, G. A.; Nair, V.; Hansen, B. T.; Hoyt, F. H.; Fischer, E. R.; Ehrenfeld, E. (2012): Complex dynamic development of poliovirus membranous replication complexes. In *Journal of virology* 86 (1), pp. 302–312. DOI: 10.1128/jvi.05937-11.

Bendjennat, M.; Saffarian, S. (2016): The Race against Protease Activation Defines the Role of ESCRTs in HIV Budding. In *PLoS Pathogens* 12 (6), e1005657. DOI: 10.1371/journal.ppat.1005657.

Beniac, D. R.; Booth, T. F. (2017): Structure of the Ebola virus glycoprotein spike within the virion envelope at 11 Å resolution. In *Scientific reports* 7, p. 46374. DOI: 10.1038/srep46374.

Berlioz-Torrent, C.; Shacklett, B. L.; Erdtmann, L.; Delamarre, L.; Bouchaert, I.; Sonigo, P.; Dokhelar, M. C.; Benarous, R. (1999): Interactions of the cytoplasmic domains of human and simian retroviral transmembrane proteins with components of the clathrin adaptor complexes modulate intracellular and cell surface expression of envelope glycoproteins. In *Journal of virology* 73 (2), pp. 1350–1361. DOI: 10.1128/JVI.73.2.1350-1361.1999.

Besenicar, M. P.; Bavdek, A.; Kladnik, A.; Macek, P.; Anderluh, G. (2008): Kinetics of cholesterol extraction from lipid membranes by methyl-beta-cyclodextrin--a surface plasmon resonance approach. In *Biochimica et biophysica acta* 1778 (1), pp. 175–184. DOI: 10.1016/j.bbamem.2007.09.022.

Bhattacharya, J.; Repik, A.; Clapham, P. R. (2006): Gag regulates association of human immunodeficiency virus type 1 envelope with detergent-resistant

membranes. In *Journal of virology* 80 (11), pp. 5292–5300. DOI: 10.1128/jvi.01469-05.

Bilanges, B.; Posor, Y.; Vanhaesebroeck, B. (2019): PI3K isoforms in cell signalling and vesicle trafficking. In *Nature reviews. Molecular cell biology* 20 (9), pp. 515–534. DOI: 10.1038/s41580-019-0129-z.

Blanchette-Mackie, E. J.; Dwyer, N. K.; Amende, L. M.; Kruth, H. S.; Butler, J. D.; Sokol, J.; Comly, M. E.; Vanier, M. T.; August, J. T.; Brady, R. O. (1988): Type-C Niemann-Pick disease: low density lipoprotein uptake is associated with premature cholesterol accumulation in the Golgi complex and excessive cholesterol storage in lysosomes. In *Proceedings of the National Academy of Sciences of the United States of America* 85 (21), pp. 8022–8026. DOI: 10.1073/pnas.85.21.8022.

Blot, G.; Janvier, K.; Le Panse, S.; Benarous, R.; Berlioz-Torrent, C. (2003): Targeting of the human immunodeficiency virus type 1 envelope to the trans-Golgi network through binding to TIP47 is required for env incorporation into virions and infectivity. In *Journal of virology* 77 (12), pp. 6931–6945. DOI: 10.1128/jvi.77.12.6931-6945.2003.

Blot, V.; Delamarre, L.; Perugi, F.; Pham, D.; Bénichou, S.; Benarous, R.; Hanada, T.; Chishti, A. H.; Dokhélar, M.-C.; Pique, C. (2004): Human Dlg protein binds to the envelope glycoproteins of human T-cell leukemia virus type 1 and regulates envelope mediated cell-cell fusion in T lymphocytes. In *Journal of cell science* 117 (Pt 17), pp. 3983–3993. DOI: 10.1242/jcs.01266.

Boge, M.; Wyss, S.; Bonifacino, J. S.; Thali, M. (1998): A membrane-proximal tyrosine-based signal mediates internalization of the HIV-1 envelope glycoprotein via interaction with the AP-2 clathrin adaptor. In *The Journal of biological chemistry* 273 (25), pp. 15773–15778. DOI: 10.1074/jbc.273.25.15773.

Bou-Nader, C.; Muecksch, F.; Brown, J. B.; Gordon, J. M.; York, A.; Peng, C.; Ghirlando, R.; Summers, M. F.; Bieniasz, P. D.; Zhang, J. (2021): HIV-1 matrix-tRNA complex structure reveals basis for host control of Gag localization. In *Cell host & microbe* 29 (9), 1421-1436.e7. DOI: 10.1016/j.chom.2021.07.006.

Bozek, K.; Eckhardt, M.; Sierra, S.; Anders, M.; Kaiser, R.; Kräusslich, H.-G.; Müller, B.; Lengauer, T. (2012): An expanded model of HIV cell entry phenotype based on multi-parameter single-cell data. In *Retrovirology* 9, p. 60. DOI: 10.1186/1742-4690-9-60.

Brandenberg, O. F.; Magnus, C.; Rusert, P.; Regoes, R. R.; Trkola, A. (2015): Different infectivity of HIV-1 strains is linked to number of envelope trimers required for entry. In *PLoS Pathogens* 11 (1), e1004595. DOI: 10.1371/journal.ppat.1004595.

Briggs, J. A.G.; Kräusslich, H.-G. (2011): The molecular architecture of HIV. In *Journal of molecular biology* 410 (4), pp. 491–500. DOI: 10.1016/j.jmb.2011.04.021.

Briggs, J. A.G.; Riches, J. D.; Glass, B.; Bartonova, V.; Zanetti, G.; Kräusslich, H.-G. (2009): Structure and assembly of immature HIV. In *Proceedings of the National Academy of Sciences of the United States of America* 106 (27), pp. 11090–11095. DOI: 10.1073/pnas.0903535106.

Broder, S.; Gallo, R. C. (1984): A pathogenic retrovirus (HTLV-III) linked to AIDS. In *The New England journal of medicine* 311 (20), pp. 1292–1297. DOI: 10.1056/NEJM198411153112006.

Brown, D. A.; London, E. (1997): Structure of detergent-resistant membrane domains: does phase separation occur in biological membranes? In *Biochemical and biophysical research communications* 240 (1), pp. 1–7. DOI: 10.1006/bbrc.1997.7575.

Brügger, B.; Glass, B.; Haberkant, P.; Leibrecht, I.; Wieland, F. T.; Kräusslich, H.-G. (2006): The HIV lipidome: a raft with an unusual composition. In *Proceedings of the National Academy of Sciences of the United States of America* 103 (8), pp. 2641–2646. DOI: 10.1073/pnas.0511136103.

Bryant, M.; Ratner, L. (1990): Myristoylation-dependent replication and assembly of human immunodeficiency virus 1. In *Proceedings of the National Academy of Sciences of the United States of America* 87 (2), pp. 523–527. DOI: 10.1073/pnas.87.2.523.

Buffalo, C. Z.; Iwamoto, Y.; Hurley, J. H.; Ren, X. (2019): How HIV Nef Proteins Hijack Membrane Traffic To Promote Infection. In *Journal of virology* 93 (24). DOI: 10.1128/JVI.01322-19.

Buttler, C. A.; Pezeshkian, N.; Fernandez, M. V.; Aaron, J.; Norman, S.; Freed, E. O.; van Engelenburg, S. B. (2018): Single molecule fate of HIV-1 envelope reveals late-stage viral lattice incorporation. In *Nature communications* 9 (1), p. 1861. DOI: 10.1038/s41467-018-04220-w.

Camus, G.; Segura-Morales, C.; Molle, D.; Lopez-Vergès, S.; Begon-Pescia, C.; Cazevieille, C.; Schu, P.; Bertrand, E.; Berlioz-Torrent, C.; Basyuk, E. (2007): The clathrin adaptor complex AP-1 binds HIV-1 and MLV Gag and facilitates their budding. In *Molecular biology of the cell* 18 (8), pp. 3193–3203. DOI: 10.1091/mbc.e06-12-1147.

Carlson, C. J.; Gibb, R. J.; Albery, G. F.; Brierley, L.; Connor, R. P.; Dallas, T. A.; Eskew, E. A.; Fagre, A. C.; Farrell, M. J.; Frank, H. K.; Muylaert, R. L.; Poisot, T.; Rasmussen, A. L. et al. (2022): The Global Virome in One Network (VIRION): an Atlas of Vertebrate-Virus Associations. In *mBio* 13 (2), e0298521. DOI: 10.1128/mbio.02985-21.

Carlson, L.-A.; Marco, A. de; Oberwinkler, H.; Habermann, A.; Briggs, J. A.G.; Kräusslich, H.-G.; Grünewald, K. (2010): Cryo electron tomography of native HIV-1 budding sites. In *PLoS Pathogens* 6 (11), e1001173. DOI: 10.1371/journal.ppat.1001173.

Carstea, E. D.; Morris, J. A.; Coleman, K. G.; Loftus, S. K.; Zhang, D.; Cummings, C.; Gu, J.; Rosenfeld, M. A.; Pavan, W. J.; Krizman, D. B.; Nagle, J.; Polymeropoulos, M. H.; Sturley, S. L. et al. (1997): Niemann-Pick C1 disease gene: homology to mediators of cholesterol homeostasis. In *Science (New York, N.Y.)* 277 (5323), pp. 228–231. DOI: 10.1126/science.277.5323.228.

Chan, R.; Uchil, P. D.; Jin, J.; Shui, G.; Ott, D. E.; Mothes, W.; Wenk, M. R. (2008): Retroviruses human immunodeficiency virus and murine leukemia virus are enriched in phosphoinositides. In *Journal of virology* 82 (22), pp. 11228–11238. DOI: 10.1128/jvi.00981-08.

Charlier, L.; Louet, M.; Chaloin, L.; Fuchs, P.; Martinez, J.; Muriaux, D.; Favard, C.; Floquet, N. (2014): Coarse-grained simulations of the HIV-1 matrix protein anchoring: revisiting its assembly on membrane domains. In *Biophysical journal* 106 (3), pp. 577–585. DOI: 10.1016/j.bpj.2013.12.019.

Charrin, S.; Manié, S.; Thiele, C.; Billard, M.; Gerlier, D.; Boucheix, C.; Rubinstein, E. (2003): A physical and functional link between cholesterol and tetraspanins. In *European journal of immunology* 33 (9), pp. 2479–2489. DOI: 10.1002/eji.200323884.

Checkley, M. A.; Luttge, B. G.; Freed, E. O. (2011): HIV-1 envelope glycoprotein biosynthesis, trafficking, and incorporation. In *Journal of molecular biology* 410 (4), pp. 582–608. DOI: 10.1016/j.jmb.2011.04.042.

Chertova, E.; Bess, J. W.; Crise, B. J.; Sowder II, R. C.; Schaden, T. M.; Hilburn, J. M.; Hoxie, J. A.; Benveniste, R. E.; Lifson, J. D.; Henderson, L. E.; Arthur, L. O. (2002): Envelope glycoprotein incorporation, not shedding of surface envelope glycoprotein (gp120/SU), Is the primary determinant of SU content of purified human immunodeficiency virus type 1 and simian immunodeficiency virus. In *Journal of virology* 76 (11), pp. 5315–5325. DOI: 10.1128/jvi.76.11.5315-5325.2002.

Chlanda, P.; Carbajal, M. A.; Cyrklaff, M.; Griffiths, G.; Krijnse-Locker, J. (2009): Membrane rupture generates single open membrane sheets during vaccinia virus assembly. In *Cell host & microbe* 6 (1), pp. 81–90. DOI: 10.1016/j.chom.2009.05.021.

Chojnacki, J.; Eggeling, C. (2021): Super-Resolution STED Microscopy-Based Mobility Studies of the Viral Env Protein at HIV-1 Assembly Sites of Fully Infected T-Cells. In *Viruses* 13 (4). DOI: 10.3390/v13040608.

Chojnacki, J.; Staudt, T.; Glass, B.; Bingen, P.; Engelhardt, J.; Anders, M.; Schneider, J.; Müller, B.; Hell, S. W.; Kräusslich, H.-G. (2012): Maturation-dependent HIV-1 surface protein redistribution revealed by fluorescence nanoscopy. In *Science (New York, N.Y.)* 338 (6106), pp. 524–528. DOI: 10.1126/science.1226359.

Chojnacki, J.; Waithe, D.; Carravilla, P.; Huarte, N.; Galiani, S.; Enderlein, J.; Eggeling, C. (2017): Envelope glycoprotein mobility on HIV-1 particles depends on the virus maturation state. In *Nature communications* 8 (1), p. 545. DOI: 10.1038/s41467-017-00515-6.

Choubey, A.; Kalia, R. K.; Malmstadt, N.; Nakano, A.; Vashishta, P. (2013): Cholesterol translocation in a phospholipid membrane. In *Biophysical journal* 104 (11), pp. 2429–2436. DOI: 10.1016/j.bpj.2013.04.036.

Christensen, D. E.; Ganser-Pornillos, B. K.; Johnson, J. S.; Pornillos, O.; Sundquist, W. I. (2020): Reconstitution and visualization of HIV-1 capsid-dependent replication and integration in vitro. In *Science (New York, N.Y.)* 370 (6513). DOI: 10.1126/science.abc8420.

Chukkapalli, V.; Hogue, I. B.; Boyko, V.; Hu, W.-S.; Ono, A. (2008): Interaction between the human immunodeficiency virus type 1 Gag matrix domain and phosphatidylinositol-(4,5)-bisphosphate is essential for efficient gag membrane binding. In *Journal of virology* 82 (5), pp. 2405–2417. DOI: 10.1128/JVI.01614-07.

Chukkapalli, V.; Inlora, J.; Todd, G. C.; Ono, A. (2013): Evidence in support of RNA-mediated inhibition of phosphatidylserine-dependent HIV-1 Gag membrane binding in cells. In *Journal of virology* 87 (12), pp. 7155–7159. DOI: 10.1128/JVI.00075-13.

Chukkapalli, V.; Oh, S. J.; Ono, A. (2010): Opposing mechanisms involving RNA and lipids regulate HIV-1 Gag membrane binding through the highly basic region of the matrix domain. In *Proceedings of the National Academy of Sciences of the United States of America* 107 (4), pp. 1600–1605. DOI: 10.1073/pnas.0908661107.

Churchward, M. A.; Rogasevskaia, T.; Brandman, D. M.; Khosravani, H.; Nava, P.; Atkinson, J. K.; Coorssen, J. R. (2008): Specific lipids supply critical negative spontaneous curvature--an essential component of native Ca2+-triggered membrane fusion. In *Biophysical journal* 94 (10), pp. 3976–3986. DOI: 10.1529/biophysj.107.123984.

Churchward, M. A.; Rogasevskaia, T.; Höfgen, J.; Bau, J.; Coorssen, J. R. (2005): Cholesterol facilitates the native mechanism of Ca2+-triggered membrane fusion. In *Journal of cell science* 118 (Pt 20), pp. 4833–4848. DOI: 10.1242/jcs.02601.

Colibus, L. de; Sonnen, A. F.-P.; Morris, K. J.; Siebert, C. A.; Abrusci, P.; Plitzko, J.; Hodnik, V.; Leippe, M.; Volpi, E.; Anderluh, G.; Gilbert, R. J.C. (2012): Structures of lysenin reveal a shared evolutionary origin for pore-forming proteins and its mode of sphingomyelin recognition. In *Structure (London, England : 1993)* 20 (9), pp. 1498–1507. DOI: 10.1016/j.str.2012.06.011.

Collins, M. D.; Keller, S. L. (2008): Tuning lipid mixtures to induce or suppress domain formation across leaflets of unsupported asymmetric bilayers. In *Proceedings of the National Academy of Sciences of the United States of America* 105 (1), pp. 124–128. DOI: 10.1073/pnas.0702970105.

Cornell, C. E.; Mileant, A.; Thakkar, N.; Lee, K. K.; Keller, S. L. (2020): Direct imaging of liquid domains in membranes by cryo-electron tomography. In *Proceedings of the National Academy of Sciences of the United States of America* 117 (33), pp. 19713–19719. DOI: 10.1073/pnas.2002245117.

Courtney, K. C.; Fung, K. Y.; Maxfield, F. R.; Fairn, G. D.; Zha, X. (2018): Comment on 'Orthogonal lipid sensors identify transbilayer asymmetry of plasma membrane cholesterol'. In *eLife* 7. DOI: 10.7554/eLife.38493.

Das, A.; Goldstein, J. L.; Anderson, D. D.; Brown, M. S.; Radhakrishnan, A. (2013): Use of mutant 125I-perfringolysin O to probe transport and organization of cholesterol in membranes of animal cells. In *Proceedings of the National Academy of Sciences of the United States of America* 110 (26), pp. 10580–10585. DOI: 10.1073/pnas.1309273110.

Deacon, N. J.; Tsykin, A.; Solomon, A.; Smith, K.; Ludford-Menting, M.; Hooker, D. J.; McPhee, D. A.; Greenway, A. L.; Ellett, A.; Chatfield, C.; Lawson, V. A.; Crowe, S.; Maerz, A. et al. (1995): Genomic structure of an attenuated quasi species of HIV-1 from a blood transfusion donor and recipients. In *Science (New York, N.Y.)* 270 (5238), pp. 988–991. DOI: 10.1126/science.270.5238.988.

Demirov, D. G.; Orenstein, J. M.; Freed, E. O. (2002): The late domain of human immunodeficiency virus type 1 p6 promotes virus release in a cell type-dependent manner. In *Journal of virology* 76 (1), pp. 105–117. DOI: 10.1128/jvi.76.1.105-117.2002.

Deml, L.; Bojak, A.; Steck, S.; Graf, M.; Wild, J.; Schirmbeck, R.; Wolf, H.; Wagner, R. (2001): Multiple effects of codon usage optimization on expression and immunogenicity of DNA candidate vaccines encoding the human immunodeficiency virus type 1 Gag protein. In *Journal of virology* 75 (22), pp. 10991–11001. DOI: 10.1128/jvi.75.22.10991-11001.2001.

Di Paolo, G.; Camilli, P. de (2006): Phosphoinositides in cell regulation and membrane dynamics. In *Nature* 443 (7112), pp. 651–657. DOI: 10.1038/nature05185.

Dick, R. A.; Zadrozny, K. K.; Xu, C.; Schur, F. K.M.; Lyddon, T. D.; Ricana, C. L.; Wagner, J. M.; Perilla, J. R.; Ganser-Pornillos, B. K.; Johnson, M. C.; Pornillos, O.; Vogt, V. M. (2018): Inositol phosphates are assembly co-factors for HIV-1. In *Nature* 560 (7719), pp. 509–512. DOI: 10.1038/s41586-018-0396-4.

Domanska, M.; Setny, P. (2024): Exploring the Properties of Curved Lipid Membranes: Comparative Analysis of Atomistic and Coarse-Grained Force Fields. In *The journal of physical chemistry. B* 128 (29), pp. 7160–7171. DOI: 10.1021/acs.jpcb.4c02310.

Dorfman, T.; Mammano, F.; Haseltine, W. A.; Göttlinger, H. G. (1994): Role of the matrix protein in the virion association of the human immunodeficiency virus type 1 envelope glycoprotein. In *Journal of virology* 68 (3), pp. 1689–1696. DOI: 10.1128/JVI.68.3.1689-1696.1994.

D'Souza, V.; Summers, M. F. (2005): How retroviruses select their genomes. In *Nature reviews. Microbiology* 3 (8), pp. 643–655. DOI: 10.1038/nrmicro1210.

Eckhardt, M.; Anders, M.; Muranyi, W.; Heilemann, M.; Krijnse-Locker, J.; Müller, B. (2011): A SNAP-tagged derivative of HIV-1--a versatile tool to study virus-cell interactions. In *PloS one* 6 (7), e22007. DOI: 10.1371/journal.pone.0022007.

Einav, T.; Gentles, L. E.; Bloom, J. D. (2020): SnapShot: Influenza by the Numbers. In *Cell* 182 (2), 532-532.e1. DOI: 10.1016/j.cell.2020.05.004.

Elalouf, A.; Maoz, H.; Rosenfeld, A. Y. (2024): Comprehensive Insights into the Molecular Basis of HIV Glycoproteins. In *Applied Sciences* 14 (18), p. 8271. DOI: 10.3390/app14188271.

Emerson, V.; Haller, C.; Pfeiffer, T.; Fackler, O. T.; Bosch, V. (2010): Role of the C-terminal domain of the HIV-1 glycoprotein in cell-to-cell viral transmission between T lymphocytes. In *Retrovirology* 7, p. 43. DOI: 10.1186/1742-4690-7-43.

Enoki, T. A.; Heberle, F. A. (2023): Experimentally determined leaflet-leaflet phase diagram of an asymmetric lipid bilayer. In *Proceedings of the National Academy of Sciences of the United States of America* 120 (46), e2308723120. DOI: 10.1073/pnas.2308723120.

Fahy, E.; Cotter, D.; Sud, M.; Subramaniam, S. (2011): Lipid classification, structures and tools. In *Biochimica et biophysica acta* 1811 (11), pp. 637–647. DOI: 10.1016/j.bbalip.2011.06.009.

Farrand, A. J.; LaChapelle, S.; Hotze, E. M.; Johnson, A. E.; Tweten, R. K. (2010): Only two amino acids are essential for cytolytic toxin recognition of cholesterol at the membrane surface. In *Proceedings of the National Academy of Sciences of the United States of America* 107 (9), pp. 4341–4346. DOI: 10.1073/pnas.0911581107.

Favard, C.; Chojnacki, J.; Merida, P.; Yandrapalli, N.; Mak, J.; Eggeling, C.; Muriaux, D. (2019): HIV-1 Gag specifically restricts PI(4,5)P2 and cholesterol mobility in living cells creating a nanodomain platform for virus assembly. In *Science advances* 5 (10), eaaw8651. DOI: 10.1126/sciadv.aaw8651.

Fecchi, K.; Anticoli, S.; Peruzzu, D.; Iessi, E.; Gagliardi, M. C.; Matarrese, P.; Ruggieri, A. (2020): Coronavirus Interplay With Lipid Rafts and Autophagy Unveils Promising Therapeutic Targets. In *Frontiers in microbiology* 11, p. 1821. DOI: 10.3389/fmicb.2020.01821.

Francis, A. C.; Marin, M.; Singh, P. K.; Achuthan, V.; Prellberg, M. J.; Palermino-Rowland, K.; Lan, S.; Tedbury, P. R.; Sarafianos, S. G.; Engelman, A. N.; Melikyan, G. B. (2020): HIV-1 replication complexes accumulate in nuclear speckles and integrate into speckle-associated genomic domains. In *Nature communications* 11 (1), p. 3505. DOI: 10.1038/s41467-020-17256-8.

Freed, E. O. (2015): HIV-1 assembly, release and maturation. In *Nature reviews. Microbiology* 13 (8), pp. 484–496. DOI: 10.1038/nrmicro3490.

Freed, E. O.; Martin, M. A. (1995): Virion incorporation of envelope glycoproteins with long but not short cytoplasmic tails is blocked by specific, single amino acid substitutions in the human immunodeficiency virus type 1 matrix. In *Journal of virology* 69 (3), pp. 1984–1989. DOI: 10.1128/JVI.69.3.1984-1989.1995.

Freed, E. O.; Martin, M. A. (1996): Domains of the human immunodeficiency virus type 1 matrix and gp41 cytoplasmic tail required for envelope incorporation into virions. In *Journal of virology* 70 (1), pp. 341–351. DOI: 10.1128/JVI.70.1.341-351.1996.

Freed, E. O.; Orenstein, J. M.; Buckler-White, A. J.; Martin, M. A. (1994): Single amino acid changes in the human immunodeficiency virus type 1 matrix protein block virus particle production. In *Journal of virology* 68 (8), pp. 5311–5320. DOI: 10.1128/JVI.68.8.5311-5320.1994.

Gaines, C. R.; Tkacik, E.; Rivera-Oven, A.; Somani, P.; Achimovich, A.; Alabi, T.; Zhu, A.; Getachew, N.; Yang, A. L.; McDonough, M.; Hawkins, T.; Spadaro, Z.; Summers, M. F. (2018): HIV-1 Matrix Protein Interactions with tRNA: Implications for Membrane Targeting. In *Journal of molecular biology* 430 (14), pp. 2113–2127. DOI: 10.1016/j.jmb.2018.04.042.

Gautier, A.; Juillerat, A.; Heinis, C.; Corrêa, I. R.; Kindermann, M.; Beaufils, F.; Johnsson, K. (2008): An engineered protein tag for multiprotein labeling in living cells. In *Chemistry & biology* 15 (2), pp. 128–136. DOI: 10.1016/j.chembiol.2008.01.007.

Gerl, M. J.; Bittl, V.; Kirchner, S.; Sachsenheimer, T.; Brunner, H. L.; Lüchtenborg, C.; Özbalci, C.; Wiedemann, H.; Wegehingel, S.; Nickel, W.; Haberkant, P.; Schultz, C.; Krüger, M.; Brügger, B. (2016): Sphingosine-1-Phosphate Lyase Deficient Cells as a Tool to Study Protein Lipid Interactions. In *PloS one* 11 (4), e0153009. DOI: 10.1371/journal.pone.0153009.

Gerl, M. J.; Sampaio, J. L.; Urban, S.; Kalvodova, L.; Verbavatz, J.-M.; Binnington, B.; Lindemann, D.; Lingwood, C. A.; Shevchenko, A.; Schroeder, C.; Simons, K. (2012): Quantitative analysis of the lipidomes of the influenza virus envelope and MDCK cell apical membrane. In *The Journal of cell biology* 196 (2), pp. 213–221. DOI: 10.1083/jcb.201108175.

Giang, H.; Schick, M. (2014): How cholesterol could be drawn to the cytoplasmic leaf of the plasma membrane by phosphatidylethanolamine. In *Biophysical journal* 107 (10), pp. 2337–2344. DOI: 10.1016/j.bpj.2014.10.012.

Glatz, J. F.C.; Luiken, J. J.F.P.; Bonen, A. (2010): Membrane fatty acid transporters as regulators of lipid metabolism: implications for metabolic disease. In *Physiological reviews* 90 (1), pp. 367–417. DOI: 10.1152/physrev.00003.2009.

Glende, J.; Schwegmann-Wessels, C.; Al-Falah, M.; Pfefferle, S.; Qu, X.; Deng, H.; Drosten, C.; Naim, H. Y.; Herrler, G. (2008): Importance of cholesterol-rich membrane microdomains in the interaction of the S protein of SARS-coronavirus with the cellular receptor angiotensin-converting enzyme 2. In *Virology* 381 (2), pp. 215–221. DOI: 10.1016/j.virol.2008.08.026.

Gorry, P. R.; McPhee, D. A.; Verity, E.; Dyer, W. B.; Wesselingh, S. L.; Learmont, J.; Sullivan, J. S.; Roche, M.; Zaunders, J. J.; Gabuzda, D.; Crowe, S. M.; Mills, J.; Lewin, S. R. et al. (2007): Pathogenicity and immunogenicity of attenuated, nef-deleted HIV-1 strains in vivo. In *Retrovirology* 4, p. 66. DOI: 10.1186/1742-4690-4-66.

Gorter, E.; Grendel, F. (1925): ON BIMOLECULAR LAYERS OF LIPOIDS ON THE CHROMOCYTES OF THE BLOOD. In *The Journal of experimental medicine* 41 (4), pp. 439–443. DOI: 10.1084/jem.41.4.439.

Gosert, R.; Egger, D.; Lohmann, V.; Bartenschlager, R.; Blum, H. E.; Bienz, K.; Moradpour, D. (2003): Identification of the hepatitis C virus RNA replication complex in Huh-7 cells harboring subgenomic replicons. In *Journal of virology* 77 (9), pp. 5487–5492. DOI: 10.1128/jvi.77.9.5487-5492.2003.

Göttlinger, H. G.; Dorfman, T.; Sodroski, J. G.; Haseltine, W. A. (1991): Effect of mutations affecting the p6 gag protein on human immunodeficiency virus particle release. In *Proceedings of the National Academy of Sciences of the United States of America* 88 (8), pp. 3195–3199. DOI: 10.1073/pnas.88.8.3195.

Göttlinger, H. G.; Sodroski, J. G.; Haseltine, W. A. (1989): Role of capsid precursor processing and myristoylation in morphogenesis and infectivity of human

immunodeficiency virus type 1. In *Proceedings of the National Academy of Sciences of the United States of America* 86 (15), pp. 5781–5785. DOI: 10.1073/pnas.86.15.5781.

Gousset, K.; Ablan, S. D.; Coren, L. V.; Ono, A.; Soheilian, F.; Nagashima, K.; Ott, D. E.; Freed, E. O. (2008): Real-time visualization of HIV-1 GAG trafficking in infected macrophages. In *PLoS Pathogens* 4 (3), e1000015. DOI: 10.1371/journal.ppat.1000015.

Grigorov, B.; Décimo, D.; Smagulova, F.; Péchoux, C.; Mougel, M.; Muriaux, D.; Darlix, J.-L. (2007): Intracellular HIV-1 Gag localization is impaired by mutations in the nucleocapsid zinc fingers. In *Retrovirology* 4, p. 54. DOI: 10.1186/1742-4690-4-54.

Gubbens, J.; Kroon, A. I.P.M. de (2010): Proteome-wide detection of phospholipid-protein interactions in mitochondria by photocrosslinking and click chemistry. In *Molecular bioSystems* 6 (10), pp. 1751–1759. DOI: 10.1039/C003064N.

Gubbens, J.; Ruijter, E.; Fays, L. E.V. de; Damen, J. M.A.; Kruijff, B. de; Slijper, M.; Rijkers, D. T.S.; Liskamp, R. M.J.; Kroon, A. I.P.M. de (2009): Photocrosslinking and click chemistry enable the specific detection of proteins interacting with phospholipids at the membrane interface. In *Chemistry & biology* 16 (1), pp. 3–14. DOI: 10.1016/j.chembiol.2008.11.009.

Haberkant, P.; Raijmakers, R.; Wildwater, M.; Sachsenheimer, T.; Brügger, B.; Maeda, K.; Houweling, M.; Gavin, A.-C.; Schultz, C.; van Meer, G.; Heck, A. J.R.; Holthuis, J. C.M. (2013): In vivo profiling and visualization of cellular protein-lipid interactions using bifunctional fatty acids. In *Angewandte Chemie (International ed. in English)* 52 (14), pp. 4033–4038. DOI: 10.1002/anie.201210178.

Haberkant, P.; Stein, F.; Höglinger, D.; Gerl, M. J.; Brügger, B.; van Veldhoven, P. P.; Krijgsveld, J.; Gavin, A.-C.; Schultz, C. (2016): Bifunctional Sphingosine for Cell-Based Analysis of Protein-Sphingolipid Interactions. In *ACS chemical biology* 11 (1), pp. 222–230. DOI: 10.1021/acschembio.5b00810.

Haller, C.; Fackler, O. T. (2008): HIV-1 at the immunological and T-lymphocytic virological synapse. In *Biological chemistry* 389 (10), pp. 1253–1260. DOI: 10.1515/BC.2008.143.

Hammonds, J.; Wang, J.-J.; Spearman, P. (2012): Restriction of Retroviral Replication by Tetherin/BST-2. In *Molecular biology international* 2012, p. 424768. DOI: 10.1155/2012/424768.

Hammonds, J.; Wang, J.-J.; Yi, H.; Spearman, P. (2010): Immunoelectron microscopic evidence for Tetherin/BST2 as the physical bridge between HIV-1 virions and the plasma membrane. In *PLoS Pathogens* 6 (2), e1000749. DOI: 10.1371/journal.ppat.1000749.

Hanne, J.; Göttfert, F.; Schimer, J.; Anders-Össwein, M.; Konvalinka, J.; Engelhardt, J.; Müller, B.; Hell, S. W.; Kräusslich, H.-G. (2016): Stimulated Emission Depletion Nanoscopy Reveals Time-Course of Human Immunodeficiency Virus Proteolytic Maturation. In *ACS nano* 10 (9), pp. 8215–8222. DOI: 10.1021/acsnano.6b03850.

Haque, M.; Hirai, Y.; Yokota, K.; Oguma, K. (1995): Steryl glycosides: a characteristic feature of the Helicobacter spp.? In *Journal of bacteriology* 177 (18), pp. 5334–5337. DOI: 10.1128/jb.177.18.5334-5337.1995.

Harayama, T.; Riezman, H. (2018): Understanding the diversity of membrane lipid composition. In *Nature reviews. Molecular cell biology* 19 (5), pp. 281–296. DOI: 10.1038/nrm.2017.138.

Harikumar, K. G.; Puri, V.; Singh, R. D.; Hanada, K.; Pagano, R. E.; Miller, L. J. (2005): Differential effects of modification of membrane cholesterol and sphingolipids on the conformation, function, and trafficking of the G protein-coupled cholecystokinin receptor. In *The Journal of biological chemistry* 280 (3), pp. 2176–2185. DOI: 10.1074/jbc.M410385200.

Hartley, O.; Klasse, P. J.; Sattentau, Q. J.; Moore, J. P. (2005): V3: HIV's switch-hitter. In *AIDS research and human retroviruses* 21 (2), pp. 171–189. DOI: 10.1089/aid.2005.21.171.

Hauser, H.; Lopez, L. A.; Yang, S. J.; Oldenburg, J. E.; Exline, C. M.; Guatelli, J. C.; Cannon, P. M. (2010): HIV-1 Vpu and HIV-2 Env counteract BST-2/tetherin by sequestration in a perinuclear compartment. In *Retrovirology* 7, p. 51. DOI: 10.1186/1742-4690-7-51.

He, C.; Hu, X.; Jung, R. S.; Weston, T. A.; Sandoval, N. P.; Tontonoz, P.; Kilburn, M. R.; Fong, L. G.; Young, S. G.; Jiang, H. (2017): High-resolution imaging and quantification of plasma membrane cholesterol by NanoSIMS. In *Proceedings of the National Academy of Sciences of the United States of America* 114 (8), pp. 2000–2005. DOI: 10.1073/pnas.1621432114.

Heberle, F. A.; Doktorova, M.; Scott, H. L.; Skinkle, A. D.; Waxham, M. N.; Levental, I. (2020): Direct label-free imaging of nanodomains in biomimetic and

biological membranes by cryogenic electron microscopy. In *Proceedings of the National Academy of Sciences of the United States of America* 117 (33), pp. 19943–19952. DOI: 10.1073/pnas.2002200117.

Hemelaar, J.; Elangovan, R.; Yun, J.; Dickson-Tetteh, L.; Fleminger, I.; Kirtley, S.; Williams, B.; Gouws-Williams, E.; Ghys, P. D. (2019): Global and regional molecular epidemiology of HIV-1, 1990-2015: a systematic review, global survey, and trend analysis. In *The Lancet. Infectious diseases* 19 (2), pp. 143–155. DOI: 10.1016/s1473-3099(18)30647-9.

Hendrix, J.; Baumgärtel, V.; Schrimpf, W.; Ivanchenko, S.; Digman, M. A.; Gratton, E.; Kräusslich, H.-G.; Müller, B.; Lamb, D. C. (2015): Live-cell observation of cytosolic HIV-1 assembly onset reveals RNA-interacting Gag oligomers. In *The Journal of cell biology* 210 (4), pp. 629–646. DOI: 10.1083/jcb.201504006.

Hofmann, K.; Thiele, C.; Schött, H.-F.; Gaebler, A.; Schoene, M.; Kiver, Y.; Friedrichs, S.; Lütjohann, D.; Kuerschner, L. (2014): A novel alkyne cholesterol to trace cellular cholesterol metabolism and localization. In *Journal of lipid research* 55 (3), pp. 583–591. DOI: 10.1194/jlr.D044727.

Hogue, I. B.; Grover, J. R.; Soheilian, F.; Nagashima, K.; Ono, A. (2011): Gag induces the coalescence of clustered lipid rafts and tetraspanin-enriched microdomains at HIV-1 assembly sites on the plasma membrane. In *Journal of virology* 85 (19), pp. 9749–9766. DOI: 10.1128/JVI.00743-11.

Holm, K.; Weclewicz, K.; Hewson, R.; Suomalainen, M. (2003): Human immunodeficiency virus type 1 assembly and lipid rafts: Pr55(gag) associates with membrane domains that are largely resistant to Brij98 but sensitive to Triton X-100. In *Journal of virology* 77 (8), pp. 4805–4817. DOI: 10.1128/jvi.77.8.4805-4817.2003.

Hölttä-Vuori, M.; Uronen, R.-L.; Repakova, J.; Salonen, E.; Vattulainen, I.; Panula, P.; Li, Z.; Bittman, R.; Ikonen, E. (2008): BODIPY-cholesterol: a new tool to visualize sterol trafficking in living cells and organisms. In *Traffic (Copenhagen, Denmark)* 9 (11), pp. 1839–1849. DOI: 10.1111/j.1600-0854.2008.00801.x.

Hu, B.; Höfer, C. T.; Thiele, C.; Veit, M. (2019): Cholesterol Binding to the Transmembrane Region of a Group 2 Hemagglutinin (HA) of Influenza Virus Is Essential for Virus Replication, Affecting both Virus Assembly and HA Fusion Activity. In *Journal of virology* 93 (15). DOI: 10.1128/jvi.00555-19.

Huang, M.; Orenstein, J. M.; Martin, M. A.; Freed, E. O. (1995): p6Gag is required for particle production from full-length human immunodeficiency virus type 1 molecular clones expressing protease. In *Journal of virology* 69 (11), pp. 6810–6818. DOI: 10.1128/JVI.69.11.6810-6818.1995.

Hubert, M.; Larsson, E.; Lundmark, R. (2020): Keeping in touch with the membrane; protein- and lipid-mediated confinement of caveolae to the cell surface. In *Biochemical Society transactions* 48 (1), pp. 155–163. DOI: 10.1042/BST20190386.

Hulce, J. J.; Cognetta, A. B.; Niphakis, M. J.; Tully, S. E.; Cravatt, B. F. (2013): Proteome-wide mapping of cholesterol-interacting proteins in mammalian cells. In *Nature methods* 10 (3), pp. 259–264. DOI: 10.1038/nmeth.2368.

Hymes, K. B.; Cheung, T.; Greene, J. B.; Prose, N. S.; Marcus, A.; Ballard, H.; William, D. C.; Laubenstein, L. J. (1981): Kaposi's sarcoma in homosexual men-a report of eight cases. In *Lancet (London, England)* 2 (8247), pp. 598–600. DOI: 10.1016/s0140-6736(81)92740-9.

Hyslop, P. A.; Morel, B.; Sauerheber, R. D. (1990): Organization and interaction of cholesterol and phosphatidylcholine in model bilayer membranes. In *Biochemistry* 29 (4), pp. 1025–1038. DOI: 10.1021/bi00456a027.

Ichihashi, Y.; Oie, M. (1983): The activation of vaccinia virus infectivity by the transfer of phosphatidylserine from the plasma membrane. In *Virology* 130 (2), pp. 306–317. DOI: 10.1016/0042-6822(83)90085-5.

Inamdar, K.; Tsai, F.-C.; Dibsy, R.; Poret, A. de; Manzi, J.; Merida, P.; Muller, R.; Lappalainen, P.; Roingeard, P.; Mak, J.; Bassereau, P.; Favard, C.; Muriaux, D. (2021): Full assembly of HIV-1 particles requires assistance of the membrane curvature factor IRSp53. In *eLife* 10. DOI: 10.7554/eLife.67321.

Ipsen, J. H.; Karlström, G.; Mouritsen, O. G.; Wennerström, H.; Zuckermann, M. J. (1987): Phase equilibria in the phosphatidylcholine-cholesterol system. In *Biochimica et biophysica acta* 905 (1), pp. 162–172. DOI: 10.1016/0005-2736(87)90020-4.

Ishitsuka, R.; Saito, T.; Osada, H.; Ohno-Iwashita, Y.; Kobayashi, T. (2011): Fluorescence image screening for chemical compounds modifying cholesterol metabolism and distribution. In *Journal of lipid research* 52 (11), pp. 2084–2094. DOI: 10.1194/jlr.D018184.

Ishitsuka, R.; Yamaji-Hasegawa, A.; Makino, A.; Hirabayashi, Y.; Kobayashi, T. (2004): A lipid-specific toxin reveals heterogeneity of sphingomyelin-containing membranes. In *Biophysical journal* 86 (1 Pt 1), pp. 296–307. DOI: 10.1016/S0006-3495(04)74105-3.

Ivanchenko, S.; Godinez, W. J.; Lampe, M.; Kräusslich, H.-G.; Eils, R.; Rohr, K.; Bräuchle, C.; Müller, B.; Lamb, D. C. (2009): Dynamics of HIV-1 assembly and release. In *PLoS Pathogens* 5 (11), e1000652. DOI: 10.1371/journal.ppat.1000652.

Jacks, T.; Power, M. D.; Masiarz, F. R.; Luciw, P. A.; Barr, P. J.; Varmus, H. E. (1988): Characterization of ribosomal frameshifting in HIV-1 gag-pol expression. In *Nature* 331 (6153), pp. 280–283. DOI: 10.1038/331280a0.

Jao, C. Y.; Nedelcu, D.; Lopez, L. V.; Samarakoon, T. N.; Welti, R.; Salic, A. (2015): Bioorthogonal probes for imaging sterols in cells. In *Chembiochem : a European journal of chemical biology* 16 (4), pp. 611–617. DOI: 10.1002/cbic.201402715.

Jiang, J.; Aiken, C. (2007): Maturation-dependent human immunodeficiency virus type 1 particle fusion requires a carboxyl-terminal region of the gp41 cytoplasmic tail. In *Journal of virology* 81 (18), pp. 9999–10008. DOI: 10.1128/JVI.00592-07.

Johnson, B. B.; Moe, P. C.; Wang, D.; Rossi, K.; Trigatti, B. L.; Heuck, A. P. (2012): Modifications in perfringolysin O domain 4 alter the cholesterol concentration threshold required for binding. In *Biochemistry* 51 (16), pp. 3373–3382. DOI: 10.1021/bi3003132.

Jolly, C.; Kashefi, K.; Hollinshead, M.; Sattentau, Q. J. (2004): HIV-1 cell to cell transfer across an Env-induced, actin-dependent synapse. In *The Journal of experimental medicine* 199 (2), pp. 283–293. DOI: 10.1084/jem.20030648.

Jolly, C.; Mitar, I.; Sattentau, Q. J. (2007): Adhesion molecule interactions facilitate human immunodeficiency virus type 1-induced virological synapse formation between T cells. In *Journal of virology* 81 (24), pp. 13916–13921. DOI: 10.1128/JVI.01585-07.

Jolly, C.; Sattentau, Q. J. (2004): Retroviral spread by induction of virological synapses. In *Traffic (Copenhagen, Denmark)* 5 (9), pp. 643–650. DOI: 10.1111/j.1600-0854.2004.00209.x.

Jolly, C.; Sattentau, Q. J. (2005): Human immunodeficiency virus type 1 virological synapse formation in T cells requires lipid raft integrity. In *Journal of virology* 79 (18), pp. 12088–12094. DOI: 10.1128/JVI.79.18.12088-12094.2005.

Joseph, S. B.; Swanstrom, R. (2018): The evolution of HIV-1 entry phenotypes as a guide to changing target cells. In *Journal of leukocyte biology* 103 (3), pp. 421–431. DOI: 10.1002/JLB.2RI0517-200R.

Jouvenet, N.; Bieniasz, P. D.; Simon, S. M. (2008): Imaging the biogenesis of individual HIV-1 virions in live cells. In *Nature* 454 (7201), pp. 236–240. DOI: 10.1038/nature06998.

Jouvenet, N.; Neil, S. J.D.; Bess, C.; Johnson, M. C.; Virgen, C. A.; Simon, S. M.; Bieniasz, P. D. (2006): Plasma membrane is the site of productive HIV-1 particle assembly. In *PLoS biology* 4 (12), e435. DOI: 10.1371/journal.pbio.0040435.

Kafaie, J.; Song, R.; Abrahamyan, L.; Mouland, A. J.; Laughrea, M. (2008): Mapping of nucleocapsid residues important for HIV-1 genomic RNA dimerization and packaging. In *Virology* 375 (2), pp. 592–610. DOI: 10.1016/j.virol.2008.02.001.

Kalvodova, L.; Sampaio, J. L.; Cordo, S.; Ejsing, C. S.; Shevchenko, A.; Simons, K. (2009): The lipidomes of vesicular stomatitis virus, semliki forest virus, and the host plasma membrane analyzed by quantitative shotgun mass spectrometry. In *Journal of virology* 83 (16), pp. 7996–8003. DOI: 10.1128/jvi.00635-09.

Kaposi's sarcoma and Pneumocystis pneumonia among homosexual men--New York City and California (1981). In *MMWR. Morbidity and mortality weekly report* 30 (25), pp. 305–308.

Kim, J. H.; Singh, A.; Del Poeta, M.; Brown, D. A.; London, E. (2017): The effect of sterol structure upon clathrin-mediated and clathrin-independent endocytosis. In *Journal of cell science* 130 (16), pp. 2682–2695. DOI: 10.1242/jcs.201731.

Kirchhoff, F.; Greenough, T. C.; Brettler, D. B.; Sullivan, J. L.; Desrosiers, R. C. (1995): Brief report: absence of intact nef sequences in a long-term survivor with nonprogressive HIV-1 infection. In *The New England journal of medicine* 332 (4), pp. 228–232. DOI: 10.1056/NEJM199501263320405.

Kirschman, J.; Qi, M.; Ding, L.; Hammonds, J.; Dienger-Stambaugh, K.; Wang, J.-J.; Lapierre, L. A.; Goldenring, J. R.; Spearman, P. (2018): HIV-1 Envelope Glycoprotein Trafficking through the Endosomal Recycling Compartment Is Required for Particle Incorporation. In *Journal of virology* 92 (5). DOI: 10.1128/JVI.01893-17.

Kiyokawa, E.; Baba, T.; Otsuka, N.; Makino, A.; Ohno, S.; Kobayashi, T. (2005): Spatial and functional heterogeneity of sphingolipid-rich membrane domains. In *The Journal of biological chemistry* 280 (25), pp. 24072–24084. DOI: 10.1074/jbc.M502244200.

Kluyver, T.; Ragan-Kelley, B.; Pérez, F.; Granger, B.; Bussonnier, M.; Frederic, J.; Kelley, K.; Hamrick, J.; Grout, J.; Corlay, S.; Ivanov, P.; Avila, D.; Abdalla, S. et al. (2016): Jupyter Notebooks - a publishing format for reproducible computational workflows. In : IOS Press, pp. 87–90.

Knoops, K.; Kikkert, M.; van Worm, S. H.E. den; Zevenhoven-Dobbe, J. C.; van der Meer, Y.; Koster, A. J.; Mommaas, A. M.; Snijder, E. J. (2008): SARS-coronavirus replication is supported by a reticulovesicular network of modified endoplasmic reticulum. In *PLoS biology* 6 (9), e226. DOI: 10.1371/journal.pbio.0060226.

Kollmitzer, B.; Heftberger, P.; Rappolt, M.; Pabst, G. (2013): Monolayer spontaneous curvature of raft-forming membrane lipids. In *Soft matter* 9 (45), pp. 10877–10884. DOI: 10.1039/C3SM51829A.

Kräusslich, H. G.; Fäcke, M.; Heuser, A. M.; Konvalinka, J.; Zentgraf, H. (1995): The spacer peptide between human immunodeficiency virus capsid and nucleocapsid proteins is essential for ordered assembly and viral infectivity. In *Journal of virology* 69 (6), pp. 3407–3419. DOI: 10.1128/JVI.69.6.3407-3419.1995.

Krishna, A.; Sengupta, D. (2019): Interplay between Membrane Curvature and Cholesterol: Role of Palmitoylated Caveolin-1. In *Biophysical journal* 116 (1), pp. 69–78. DOI: 10.1016/j.bpj.2018.11.3127.

Kruth, H. S.; Fry, D. L. (1984): Histochemical detection and differentiation of free and esterified cholesterol in swine atherosclerosis using filipin. In *Experimental and molecular pathology* 40 (3), pp. 288–294. DOI: 10.1016/0014-4800(84)90046-7.

Kutluay, S. B.; Bieniasz, P. D. (2010): Analysis of the initiating events in HIV-1 particle assembly and genome packaging. In *PLoS Pathogens* 6 (11), e1001200. DOI: 10.1371/journal.ppat.1001200.

Kutluay, S. B.; Zang, T.; Blanco-Melo, D.; Powell, C.; Jannain, D.; Errando, M.; Bieniasz, P. D. (2014): Global changes in the RNA binding specificity of HIV-1 gag regulate virion genesis. In *Cell* 159 (5), pp. 1096–1109. DOI: 10.1016/j.cell.2014.09.057.

Lampe, M.; Briggs, J. A.G.; Endress, T.; Glass, B.; Riegelsberger, S.; Kräusslich, H.-G.; Lamb, D. C.; Bräuchle, C.; Müller, B. (2007): Double-labelled HIV-1 particles for study of virus-cell interaction. In *Virology* 360 (1), pp. 92–104. DOI: 10.1016/j.virol.2006.10.005.

Lang, T. (2003): Imaging SNAREs at work in 'unroofed' cells--approaches that may be of general interest for functional studies on membrane proteins. In *Biochemical Society transactions* 31 (Pt 4), pp. 861–864. DOI: 10.1042/bst0310861.

Lee, I.-H.; Kai, H.; Carlson, L.-A.; Groves, J. T.; Hurley, J. H. (2015): Negative membrane curvature catalyzes nucleation of endosomal sorting complex required for transport (ESCRT)-III assembly. In *Proceedings of the National Academy of Sciences of the United States of America* 112 (52), pp. 15892–15897. DOI: 10.1073/pnas.1518765113.

Lee, J.; Kreutzberger, A. J.B.; Odongo, L.; Nelson, E. A.; Nyenhuis, D. A.; Kiessling, V.; Liang, B.; Cafiso, D. S.; White, J. M.; Tamm, L. K. (2021): Ebola virus glycoprotein interacts with cholesterol to enhance membrane fusion and cell entry. In *Nature structural & molecular biology* 28 (2), pp. 181–189. DOI: 10.1038/s41594-020-00548-4.

Lefkowitz, E. J.; Dempsey, D. M.; Hendrickson, R. C.; Orton, R. J.; Siddell, S. G.; Smith, D. B. (2018): Virus taxonomy: the database of the International Committee on Taxonomy of Viruses (ICTV). In *Nucleic acids research* 46 (D1), D708-D717. DOI: 10.1093/nar/gkx932.

Lehmann, M.; Rocha, S.; Mangeat, B.; Blanchet, F.; Uji-I, H.; Hofkens, J.; Piguet, V. (2011): Quantitative multicolor super-resolution microscopy reveals tetherin HIV-1 interaction. In *PLoS Pathogens* 7 (12), e1002456. DOI: 10.1371/journal.ppat.1002456.

Lerner, G.; Weaver, N.; Anokhin, B.; Spearman, P. (2022): Advances in HIV-1 Assembly. In *Viruses* 14 (3). DOI: 10.3390/v14030478.

Leung, K.; Kim, J.-O.; Ganesh, L.; Kabat, J.; Schwartz, O.; Nabel, G. J. (2008): HIV-1 assembly: viral glycoproteins segregate quantally to lipid rafts that associate individually with HIV-1 capsids and virions. In *Cell host & microbe* 3 (5), pp. 285–292. DOI: 10.1016/j.chom.2008.04.004.

Levin, J. G.; Guo, J.; Rouzina, I.; Musier-Forsyth, K. (2005): Nucleic acid chaperone activity of HIV-1 nucleocapsid protein: critical role in reverse

transcription and molecular mechanism. In *Progress in nucleic acid research and molecular biology* 80, pp. 217–286. DOI: 10.1016/S0079-6603(05)80006-6.

Li, D.; Ouyang, Z.; Ma, X. (2023a): Mass Spectrometry Imaging for Single-Cell or Subcellular Lipidomics: A Review of Recent Advancements and Future Development. In *Molecules* 28 (6). DOI: 10.3390/molecules28062712.

Li, W.; Qin, Z.; Nand, E.; Grunst, M. W.; Grover, J. R.; Bess, J. W.; Lifson, J. D.; Zwick, M. B.; Tagare, H. D.; Uchil, P. D.; Mothes, W. (2023b): HIV-1 Env trimers asymmetrically engage CD4 receptors in membranes. In *Nature* 623 (7989), pp. 1026–1033. DOI: 10.1038/s41586-023-06762-6.

Li, X.; Zhu, W.; Fan, M.; Zhang, J.; Peng, Y.; Huang, F.; Wang, N.; He, L.; Zhang, L.; Holmdahl, R.; Meng, L.; Lu, S. (2021): Dependence of SARS-CoV-2 infection on cholesterol-rich lipid raft and endosomal acidification. In *Computational and structural biotechnology journal* 19, pp. 1933–1943. DOI: 10.1016/j.csbj.2021.04.001.

Liang, G.; Bushman, F. D. (2021): The human virome: assembly, composition and host interactions. In *Nature reviews. Microbiology* 19 (8), pp. 514–527. DOI: 10.1038/s41579-021-00536-5.

Limpens, R. W.A.L.; van der Schaar, H. M.; Kumar, D.; Koster, A. J.; Snijder, E. J.; van Kuppeveld, F. J.M.; Bárcena, M. (2011): The transformation of enterovirus replication structures: a three-dimensional study of single- and double-membrane compartments. In *mBio* 2 (5). DOI: 10.1128/mbio.00166-11.

Lin, M.; Da, L.-T. (2020): Refolding Dynamics of gp41 from Pre-fusion to Pre-hairpin States during HIV-1 Entry. In *Journal of chemical information and modeling* 60 (1), pp. 162–174. DOI: 10.1021/acs.jcim.9b00746.

Lin, M.; Rikihisa, Y. (2003): Ehrlichia chaffeensis and Anaplasma phagocytophilum lack genes for lipid A biosynthesis and incorporate cholesterol for their survival. In *Infection and immunity* 71 (9), pp. 5324–5331. DOI: 10.1128/IAI.71.9.5324-5331.2003.

Lin, Q.; London, E. (2015): Ordered raft domains induced by outer leaflet sphingomyelin in cholesterol-rich asymmetric vesicles. In *Biophysical journal* 108 (9), pp. 2212–2222. DOI: 10.1016/j.bpj.2015.03.056.

Lingwood, C. A. (2011): Glycosphingolipid functions. In *Cold Spring Harbor perspectives in biology* 3 (7). DOI: 10.1101/cshperspect.a004788.

Liu, S. T.H.; Sharon-Friling, R.; Ivanova, P.; Milne, S. B.; Myers, D. S.; Rabinowitz, J. D.; Brown, H. A.; Shenk, T. (2011): Synaptic vesicle-like lipidome of human cytomegalovirus virions reveals a role for SNARE machinery in virion egress. In *Proceedings of the National Academy of Sciences of the United States of America* 108 (31), pp. 12869–12874. DOI: 10.1073/pnas.1109796108.

Liu, S.-L.; Sheng, R.; Jung, J. H.; Wang, L.; Stec, E.; O'Connor, M. J.; Song, S.; Bikkavilli, R. K.; Winn, R. A.; Lee, D.; Baek, K.; Ueda, K.; Levitan, I. et al. (2017): Orthogonal lipid sensors identify transbilayer asymmetry of plasma membrane cholesterol. In *Nature chemical biology* 13 (3), pp. 268–274. DOI: 10.1038/nchembio.2268.

Llewellyn, G. N.; Hogue, I. B.; Grover, J. R.; Ono, A. (2010): Nucleocapsid promotes localization of HIV-1 gag to uropods that participate in virological synapses between T cells. In *PLoS Pathogens* 6 (10), e1001167. DOI: 10.1371/journal.ppat.1001167.

Lopez-Vergès, S.; Camus, G.; Blot, G.; Beauvoir, R.; Benarous, R.; Berlioz-Torrent, C. (2006): Tail-interacting protein TIP47 is a connector between Gag and Env and is required for Env incorporation into HIV-1 virions. In *Proceedings of the National Academy of Sciences of the United States of America* 103 (40), pp. 14947–14952. DOI: 10.1073/pnas.0602941103.

Lorent, J. H.; Levental, K. R.; Ganesan, L.; Rivera-Longsworth, G.; Sezgin, E.; Doktorova, M.; Lyman, E.; Levental, I. (2020): Plasma membranes are asymmetric in lipid unsaturation, packing and protein shape. In *Nature chemical biology* 16 (6), pp. 644–652. DOI: 10.1038/s41589-020-0529-6.

Lorizate, M.; Brügger, B.; Akiyama, H.; Glass, B.; Müller, B.; Anderluh, G.; Wieland, F. T.; Kräusslich, H.-G. (2009): Probing HIV-1 membrane liquid order by Laurdan staining reveals producer cell-dependent differences. In *The Journal of biological chemistry* 284 (33), pp. 22238–22247. DOI: 10.1074/jbc.M109.029256.

Lorizate, M.; Sachsenheimer, T.; Glass, B.; Habermann, A.; Gerl, M. J.; Kräusslich, H.-G.; Brügger, B. (2013): Comparative lipidomics analysis of HIV-1 particles and their producer cell membrane in different cell lines. In *Cellular microbiology* 15 (2), pp. 292–304. DOI: 10.1111/cmi.12101.

Lorizate, M.; Terrones, O.; Nieto-Garai, J. A.; Rojo-Bartolomé, I.; Ciceri, D.; Morana, O.; Olazar-Intxausti, J.; Arboleya, A.; Martin, A.; Szynkiewicz, M.; Calleja-Felipe, M.; La Bernardino de Serna, J.; Contreras, F.-X. (2021): Super-Resolution

Microscopy Using a Bioorthogonal-Based Cholesterol Probe Provides Unprecedented Capabilities for Imaging Nanoscale Lipid Heterogeneity in Living Cells. In *Small methods* 5 (9), e2100430. DOI: 10.1002/smtd.202100430.

Louten, J. (2016): Virus Structure and Classification. In *Essential Human Virology*, pp. 19–29. DOI: 10.1016/B978-0-12-800947-5.00002-8.

Lusso, P.; Di Marzo Veronese, F.; Ensoli, B.; Franchini, G.; Jemma, C.; DeRocco, S. E.; Kalyanaraman, V. S.; Gallo, R. C. (1990): Expanded HIV-1 cellular tropism by phenotypic mixing with murine endogenous retroviruses. In *Science (New York, N.Y.)* 247 (4944), pp. 848–852. DOI: 10.1126/science.2305256.

Maekawa, M.; Fairn, G. D. (2015): Complementary probes reveal that phosphatidylserine is required for the proper transbilayer distribution of cholesterol. In *Journal of cell science* 128 (7), pp. 1422–1433. DOI: 10.1242/jcs.164715.

Makino, A.; Abe, M.; Murate, M.; Inaba, T.; Yilmaz, N.; Hullin-Matsuda, F.; Kishimoto, T.; Schieber, N. L.; Taguchi, T.; Arai, H.; Anderluh, G.; Parton, R. G.; Kobayashi, T. (2015): Visualization of the heterogeneous membrane distribution of sphingomyelin associated with cytokinesis, cell polarity, and sphingolipidosis. In *FASEB journal : official publication of the Federation of American Societies for Experimental Biology* 29 (2), pp. 477–493. DOI: 10.1096/fj.13-247585.

Mangala Prasad, V.; Leaman, D. P.; Lovendahl, K. N.; Croft, J. T.; Benhaim, M. A.; Hodge, E. A.; Zwick, M. B.; Lee, K. K. (2022): Cryo-ET of Env on intact HIV virions reveals structural variation and positioning on the Gag lattice. In *Cell* 185 (4), 641-653.e17. DOI: 10.1016/j.cell.2022.01.013.

Marco, A. de; Müller, B.; Glass, B.; Riches, J. D.; Kräusslich, H.-G.; Briggs, J. A.G. (2010): Structural analysis of HIV-1 maturation using cryo-electron tomography. In *PLoS Pathogens* 6 (11), e1001215. DOI: 10.1371/journal.ppat.1001215.

Marquardt, D.; Geier, B.; Pabst, G. (2015): Asymmetric lipid membranes: towards more realistic model systems. In *Membranes* 5 (2), pp. 180–196. DOI: 10.3390/membranes5020180.

Marquardt, D.; Kučerka, N.; Wassall, S. R.; Harroun, T. A.; Katsaras, J. (2016): Cholesterol's location in lipid bilayers. In *Chemistry and physics of lipids* 199, pp. 17–25. DOI: 10.1016/j.chemphyslip.2016.04.001.

Marx, J. L. (1984): Strong new candidate for AIDS agent. In *Science (New York, N.Y.)* 224 (4648), pp. 475–477. DOI: 10.1126/science.6324344.

McNatt, M. W.; Zang, T.; Bieniasz, P. D. (2013): Vpu binds directly to tetherin and displaces it from nascent virions. In *PLoS Pathogens* 9 (4), e1003299. DOI: 10.1371/journal.ppat.1003299.

Mercredi, P. Y.; Bucca, N.; Loeliger, B.; Gaines, C. R.; Mehta, M.; Bhargava, P.; Tedbury, P. R.; Charlier, L.; Floquet, N.; Muriaux, D.; Favard, C.; Sanders, C. R.; Freed, E. O. et al. (2016): Structural and Molecular Determinants of Membrane Binding by the HIV-1 Matrix Protein. In *Journal of molecular biology* 428 (8), pp. 1637–1655. DOI: 10.1016/j.jmb.2016.03.005.

Meyvisch, C.; Teuchy, H.; van Montagu, M. (1974): Electron microscopy of the intracellular development of bacteriophage MS2 in Escherichia coli. In *Journal of virology* 13 (6), pp. 1356–1367. DOI: 10.1128/jvi.13.6.1356-1367.1974.

Mintzer, E. A.; Waarts, B.-L.; Wilschut, J.; Bittman, R. (2002): Behavior of a photoactivatable analog of cholesterol, 6-photocholesterol, in model membranes. In *FEBS letters* 510 (3), pp. 181–184. DOI: 10.1016/S0014-5793(01)03271-9.

Mitroi, D. N.; Pereyra-Gómez, G.; Soto-Huelin, B.; Senovilla, F.; Kobayashi, T.; Esteban, J. A.; Ledesma, M. D. (2019): NPC1 enables cholesterol mobilization during long-term potentiation that can be restored in Niemann-Pick disease type C by CYP46A1 activation. In *EMBO reports* 20 (11), e48143. DOI: 10.15252/embr.201948143.

Mizuno, H.; Abe, M.; Dedecker, P.; Makino, A.; Rocha, S.; Ohno-Iwashita, Y.; Hofkens, J.; Kobayashi, T.; Miyawaki, A. (2011): Fluorescent probes for superresolution imaging of lipid domains on the plasma membrane. In *Chem. Sci.* 2 (8), p. 1548. DOI: 10.1039/c1sc00169h.

Moller-Tank, S.; Maury, W. (2014): Phosphatidylserine receptors: enhancers of enveloped virus entry and infection. In *Virology* 468-470, pp. 565–580. DOI: 10.1016/j.virol.2014.09.009.

Montes, L.-R.; Ahyayauch, H.; Ibarguren, M.; Sot, J.; Alonso, A.; Bagatolli, L. A.; Goñi, F. M. (2010): Electroformation of giant unilamellar vesicles from native membranes and organic lipid mixtures for the study of lipid domains under physiological ionic-strength conditions. In *Methods in molecular biology (Clifton, N.J.)* 606, pp. 105–114. DOI: 10.1007/978-1-60761-447-0_9.

Morén, B.; Shah, C.; Howes, M. T.; Schieber, N. L.; McMahon, H. T.; Parton, R. G.; Daumke, O.; Lundmark, R. (2012): EHD2 regulates caveolar dynamics via ATP-

driven targeting and oligomerization. In *Molecular biology of the cell* 23 (7), pp. 1316–1329. DOI: 10.1091/mbc.E11-09-0787.

Mücksch, F. (2017): Lipid-protein interactions at HIV-1 Gag assembly sites. PhD Thesis. Ruperto-Carola University of Heidelberg, Germany. CIID. Available online at https://katalog.ub.uni-heidelberg.de/cgi-bin/titel.cgi?katkey=68219588.

Mücksch, F.; Citir, M.; Lüchtenborg, C.; Glass, B.; Traynor-Kaplan, A.; Schultz, C.; Brügger, B.; Kräusslich, H.-G. (2019): Quantification of phosphoinositides reveals strong enrichment of PIP2 in HIV-1 compared to producer cell membranes. In *Scientific reports* 9 (1), p. 17661. DOI: 10.1038/s41598-019-53939-z.

Mücksch, F.; Laketa, V.; Müller, B.; Schultz, C.; Kräusslich, H.-G. (2017): Synchronized HIV assembly by tunable PIP2 changes reveals PIP2 requirement for stable Gag anchoring. In *eLife* 6. DOI: 10.7554/eLife.25287.

Muecksch, F.; Klaus, S.; Laketa, V.; Müller, B.; Kräusslich, H.-G. (2024): Probing Gag-Env dynamics at HIV-1 assembly sites using live-cell microscopy. In *Journal of virology* 98 (9), e0064924. DOI: 10.1128/jvi.00649-24.

Müller, T. G.; Zila, V.; Peters, K.; Schifferdecker, S.; Stanic, M.; Lucic, B.; Laketa, V.; Lusic, M.; Müller, B.; Kräusslich, H.-G. (2021): HIV-1 uncoating by release of viral cDNA from capsid-like structures in the nucleus of infected cells. In *eLife* 10. DOI: 10.7554/eLife.64776.

Murakami, T.; Ablan, S.; Freed, E. O.; Tanaka, Y. (2004): Regulation of human immunodeficiency virus type 1 Env-mediated membrane fusion by viral protease activity. In *Journal of virology* 78 (2), pp. 1026–1031. DOI: 10.1128/jvi.78.2.1026-1031.2004.

Murakami, T.; Freed, E. O. (2000): The long cytoplasmic tail of gp41 is required in a cell type-dependent manner for HIV-1 envelope glycoprotein incorporation into virions. In *Proceedings of the National Academy of Sciences of the United States of America* 97 (1), pp. 343–348. DOI: 10.1073/pnas.97.1.343.

Murakami, T.; Ono, A. (2021): HIV-1 entry: Duels between Env and host antiviral transmembrane proteins on the surface of virus particles. In *Current opinion in virology* 50, pp. 59–68. DOI: 10.1016/j.coviro.2021.07.005.

Muranyi, W.; Malkusch, S.; Müller, B.; Heilemann, M.; Kräusslich, H.-G. (2013): Super-resolution microscopy reveals specific recruitment of HIV-1 envelope proteins to viral assembly sites dependent on the envelope C-terminal tail. In *PLoS Pathogens* 9 (2), e1003198. DOI: 10.1371/journal.ppat.1003198.

Naito, T.; Ercan, B.; Krshnan, L.; Triebl, A.; Koh, D. H.Z.; Wei, F.-Y.; Tomizawa, K.; Torta, F. T.; Wenk, M. R.; Saheki, Y. (2019): Movement of accessible plasma membrane cholesterol by the GRAMD1 lipid transfer protein complex. In *eLife* 8. DOI: 10.7554/eLife.51401.

Neil, S. J.D.; Zang, T.; Bieniasz, P. D. (2008): Tetherin inhibits retrovirus release and is antagonized by HIV-1 Vpu. In *Nature* 451 (7177), pp. 425–430. DOI: 10.1038/nature06553.

Nguyen, D. H.; Hildreth, J. E. (2000): Evidence for budding of human immunodeficiency virus type 1 selectively from glycolipid-enriched membrane lipid rafts. In *Journal of virology* 74 (7), pp. 3264–3272. DOI: 10.1128/jvi.74.7.3264-3272.2000.

Nicolson, G. L. (2014): The Fluid-Mosaic Model of Membrane Structure: still relevant to understanding the structure, function and dynamics of biological membranes after more than 40 years. In *Biochimica et biophysica acta* 1838 (6), pp. 1451–1466. DOI: 10.1016/j.bbamem.2013.10.019.

Nieto-Garai, J. A.; Arboleya, A.; Otaegi, S.; Chojnacki, J.; Casas, J.; Fabriàs, G.; Contreras, F.-X.; Kräusslich, H.-G.; Lorizate, M. (2021): Cholesterol in the Viral Membrane is a Molecular Switch Governing HIV-1 Env Clustering. In *Advanced science (Weinheim, Baden-Wurttemberg, Germany)* 8 (3), p. 2003468. DOI: 10.1002/advs.202003468.

Ohgami, N.; Ko, D. C.; Thomas, M.; Scott, M. P.; Chang, C. C.Y.; Chang, T.-Y. (2004): Binding between the Niemann-Pick C1 protein and a photoactivatable cholesterol analog requires a functional sterol-sensing domain. In *Proceedings of the National Academy of Sciences of the United States of America* 101 (34), pp. 12473–12478. DOI: 10.1073/pnas.0405255101.

Ohishi, M.; Nakano, T.; Sakuragi, S.; Shioda, T.; Sano, K.; Sakuragi, J. (2011): The relationship between HIV-1 genome RNA dimerization, virion maturation and infectivity. In *Nucleic acids research* 39 (8), pp. 3404–3417. DOI: 10.1093/nar/gkq1314.

Ohno, H.; Aguilar, R. C.; Fournier, M. C.; Hennecke, S.; Cosson, P.; Bonifacino, J. S. (1997): Interaction of endocytic signals from the HIV-1 envelope glycoprotein complex with members of the adaptor medium chain family. In *Virology* 238 (2), pp. 305–315. DOI: 10.1006/viro.1997.8839.

Ohno-Iwashita, Y.; Shimada, Y.; Waheed, A. A.; Hayashi, M.; Inomata, M.; Nakamura, M.; Maruya, M.; Iwashita, S. (2004): Perfringolysin O, a cholesterol-binding cytolysin, as a probe for lipid rafts. In *Anaerobe* 10 (2), pp. 125–134. DOI: 10.1016/j.anaerobe.2003.09.003.

Ono, A.; Ablan, S. D.; Lockett, S. J.; Nagashima, K.; Freed, E. O. (2004): Phosphatidylinositol (4,5) bisphosphate regulates HIV-1 Gag targeting to the plasma membrane. In *Proceedings of the National Academy of Sciences of the United States of America* 101 (41), pp. 14889–14894. DOI: 10.1073/pnas.0405596101.

Ono, A.; Freed, E. O. (2001): Plasma membrane rafts play a critical role in HIV-1 assembly and release. In *Proceedings of the National Academy of Sciences of the United States of America* 98 (24), pp. 13925–13930. DOI: 10.1073/pnas.241320298.

Ono, A.; Freed, E. O. (2004): Cell-type-dependent targeting of human immunodeficiency virus type 1 assembly to the plasma membrane and the multivesicular body. In *Journal of virology* 78 (3), pp. 1552–1563. DOI: 10.1128/jvi.78.3.1552-1563.2004.

Ono, A.; Freed, E. O. (2005): Role of lipid rafts in virus replication. In *Advances in virus research* 64, pp. 311–358. DOI: 10.1016/S0065-3527(05)64010-9.

Ono, A.; Huang, M.; Freed, E. O. (1997): Characterization of human immunodeficiency virus type 1 matrix revertants: effects on virus assembly, Gag processing, and Env incorporation into virions. In *Journal of virology* 71 (6), pp. 4409–4418. DOI: 10.1128/JVI.71.6.4409-4418.1997.

Ono, A.; Orenstein, J. M.; Freed, E. O. (2000): Role of the Gag matrix domain in targeting human immunodeficiency virus type 1 assembly. In *Journal of virology* 74 (6), pp. 2855–2866. DOI: 10.1128/JVI.74.6.2855-2866.2000.

Ono, A.; Waheed, A. A.; Freed, E. O. (2007): Depletion of cellular cholesterol inhibits membrane binding and higher-order multimerization of human immunodeficiency virus type 1 Gag. In *Virology* 360 (1), pp. 27–35. DOI: 10.1016/j.virol.2006.10.011.

Pentchev, P. G.; Comly, M. E.; Kruth, H. S.; Vanier, M. T.; Wenger, D. A.; Patel, S.; Brady, R. O. (1985): A defect in cholesterol esterification in Niemann-Pick disease (type C) patients. In *Proceedings of the National Academy of Sciences of the United States of America* 82 (23), pp. 8247–8251. DOI: 10.1073/pnas.82.23.8247.

Pereira, E. A.; daSilva, L. L.P. (2016): HIV-1 Nef: Taking Control of Protein Trafficking. In *Traffic (Copenhagen, Denmark)* 17 (9), pp. 976–996. DOI: 10.1111/tra.12412.

Pettit, S. C.; Moody, M. D.; Wehbie, R. S.; Kaplan, A. H.; Nantermet, P. V.; Klein, C. A.; Swanstrom, R. (1994): The p2 domain of human immunodeficiency virus type 1 Gag regulates sequential proteolytic processing and is required to produce fully infectious virions. In *Journal of virology* 68 (12), pp. 8017–8027. DOI: 10.1128/jvi.68.12.8017-8027.1994.

Pezeshkian, N.; Groves, N. S.; van Engelenburg, S. B. (2019): Single-molecule imaging of HIV-1 envelope glycoprotein dynamics and Gag lattice association exposes determinants responsible for virus incorporation. In *Proceedings of the National Academy of Sciences of the United States of America* 116 (50), pp. 25269–25277. DOI: 10.1073/pnas.1910008116.

Phillips, D. M.; Bourinbaiar, A. S. (1992): Mechanism of HIV spread from lymphocytes to epithelia. In *Virology* 186 (1), pp. 261–273. DOI: 10.1016/0042-6822(92)90080-9.

Pickl, W. F.; Pimentel-Muiños, F. X.; Seed, B. (2001): Lipid rafts and pseudotyping. In *Journal of virology* 75 (15), pp. 7175–7183. DOI: 10.1128/JVI.75.15.7175-7183.2001.

Piguet, V.; Sattentau, Q. (2004): Dangerous liaisons at the virological synapse. In *The Journal of clinical investigation* 114 (5), pp. 605–610. DOI: 10.1172/JCI22812.

Pike, L. J. (2006): Rafts defined: a report on the Keystone Symposium on Lipid Rafts and Cell Function. In *Journal of lipid research* 47 (7), pp. 1597–1598. DOI: 10.1194/jlr.E600002-JLR200.

Pipalia, N. H.; Huang, A.; Ralph, H.; Rujoi, M.; Maxfield, F. R. (2006): Automated microscopy screening for compounds that partially revert cholesterol accumulation in Niemann-Pick C cells. In *Journal of lipid research* 47 (2), pp. 284–301. DOI: 10.1194/jlr.M500388-JLR200.

Popovic, M.; Sarngadharan, M. G.; Read, E.; Gallo, R. C. (1984): Detection, isolation, and continuous production of cytopathic retroviruses (HTLV-III) from patients with AIDS and pre-AIDS. In *Science (New York, N.Y.)* 224 (4648), pp. 497–500. DOI: 10.1126/science.6200935.

Qu, K.; Ke, Z.; Zila, V.; Anders-Össwein, M.; Glass, B.; Mücksch, F.; Müller, R.; Schultz, C.; Müller, B.; Kräusslich, H.-G.; Briggs, J. A.G. (2021): Maturation of the

matrix and viral membrane of HIV-1. In *Science (New York, N.Y.)* 373 (6555), pp. 700–704. DOI: 10.1126/science.abe6821.

Robertson, J. D. (1959): The ultrastructure of cell membranes and their derivatives. In *Biochemical Society symposium* 16, pp. 3–43.

Robertson, J. D. (1960): The molecular structure and contact relationships of cell membranes. In *Progress in biophysics and molecular biology* 10, pp. 343–418.

Rodgers, W.; Rose, J. K. (1996): Exclusion of CD45 inhibits activity of p56lck associated with glycolipid-enriched membrane domains. In *The Journal of cell biology* 135 (6 Pt 1), pp. 1515–1523. DOI: 10.1083/jcb.135.6.1515.

Roy, N. H.; Chan, J.; Lambelé, M.; Thali, M. (2013): Clustering and mobility of HIV-1 Env at viral assembly sites predict its propensity to induce cell-cell fusion. In *Journal of virology* 87 (13), pp. 7516–7525. DOI: 10.1128/JVI.00790-13.

Rujoi, M.; Pipalia, N. H.; Maxfield, F. R. (2010): Cholesterol pathways affected by small molecules that decrease sterol levels in Niemann-Pick type C mutant cells. In *PloS one* 5 (9), e12788. DOI: 10.1371/journal.pone.0012788.

Saad, J. S.; Miller, J.; Tai, J.; Kim, A.; Ghanam, R. H.; Summers, M. F. (2006): Structural basis for targeting HIV-1 Gag proteins to the plasma membrane for virus assembly. In *Proceedings of the National Academy of Sciences of the United States of America* 103 (30), pp. 11364–11369. DOI: 10.1073/pnas.0602818103.

Saha, I.; Saffarian, S. (2020): Dynamics of the HIV Gag Lattice Detected by Localization Correlation Analysis and Time-Lapse iPALM. In *Biophysical journal* 119 (3), pp. 581–592. DOI: 10.1016/j.bpj.2020.06.023.

Sanchez, S. A.; Gunther, G.; Tricerri, M. A.; Gratton, E. (2011): Methyl-β-cyclodextrins preferentially remove cholesterol from the liquid disordered phase in giant unilamellar vesicles. In *The Journal of membrane biology* 241 (1), pp. 1–10. DOI: 10.1007/s00232-011-9348-8.

Sanders, D. W.; Jumper, C. C.; Ackerman, P. J.; Bracha, D.; Donlic, A.; Kim, H.; Kenney, D.; Castello-Serrano, I.; Suzuki, S.; Tamura, T.; Tavares, A. H.; Saeed, M.; Holehouse, A. S. et al. (2021): SARS-CoV-2 requires cholesterol for viral entry and pathological syncytia formation. In *eLife* 10. DOI: 10.7554/eLife.65962.

Sauter, D.; Schindler, M.; Specht, A.; Landford, W. N.; Münch, J.; Kim, K.-A.; Votteler, J.; Schubert, U.; Bibollet-Ruche, F.; Keele, B. F.; Takehisa, J.; Ogando, Y.; Ochsenbauer, C. et al. (2009): Tetherin-driven adaptation of Vpu and Nef

function and the evolution of pandemic and nonpandemic HIV-1 strains. In *Cell host & microbe* 6 (5), pp. 409–421. DOI: 10.1016/j.chom.2009.10.004.

Schindelin, J.; Arganda-Carreras, I.; Frise, E.; Kaynig, V.; Longair, M.; Pietzsch, T.; Preibisch, S.; Rueden, C.; Saalfeld, S.; Schmid, B.; Tinevez, J.-Y.; White, D. J.; Hartenstein, V. et al. (2012): Fiji: an open-source platform for biological-image analysis. In *Nature methods* 9 (7), pp. 676–682. DOI: 10.1038/nmeth.2019.

Schroeder, F.; Holland, J. F.; Bieber, L. L. (1972): Fluorometric investigations of the interaction of polyene antibiotics with sterols. In *Biochemistry* 11 (16), pp. 3105–3111. DOI: 10.1021/bi00766a026.

Sengupta, P.; Seo, A. Y.; Pasolli, H. A.; Song, Y. E.; Johnson, M. C.; Lippincott-Schwartz, J. (2019): A lipid-based partitioning mechanism for selective incorporation of proteins into membranes of HIV particles. In *Nature cell biology* 21 (4), pp. 452–461. DOI: 10.1038/s41556-019-0300-y.

Sezgin, E.; Can, F. B.; Schneider, F.; Clausen, M. P.; Galiani, S.; Stanly, T. A.; Waithe, D.; Colaco, A.; Honigmann, A.; Wüstner, D.; Platt, F.; Eggeling, C. (2016): A comparative study on fluorescent cholesterol analogs as versatile cellular reporters. In *Journal of lipid research* 57 (2), pp. 299–309. DOI: 10.1194/jlr.M065326.

Sezgin, E.; Kaiser, H.-J.; Baumgart, T.; Schwille, P.; Simons, K.; Levental, I. (2012): Elucidating membrane structure and protein behavior using giant plasma membrane vesicles. In *Nature protocols* 7 (6), pp. 1042–1051. DOI: 10.1038/nprot.2012.059.

Sharp, P. M.; Hahn, B. H. (2011): Origins of HIV and the AIDS pandemic. In *Cold Spring Harbor perspectives in medicine* 1 (1), a006841. DOI: 10.1101/cshperspect.a006841.

Shaw, J. E.; Epand, R. F.; Epand, R. M.; Li, Z.; Bittman, R.; Yip, C. M. (2006): Correlated fluorescence-atomic force microscopy of membrane domains: structure of fluorescence probes determines lipid localization. In *Biophysical journal* 90 (6), pp. 2170–2178. DOI: 10.1529/biophysj.105.073510.

Shimada, Y.; Maruya, M.; Iwashita, S.; Ohno-Iwashita, Y. (2002): The C-terminal domain of perfringolysin O is an essential cholesterol-binding unit targeting to cholesterol-rich microdomains. In *European journal of biochemistry* 269 (24), pp. 6195–6203. DOI: 10.1046/j.1432-1033.2002.03338.x.

Shkriabai, N.; Datta, S. A.K.; Zhao, Z.; Hess, S.; Rein, A.; Kvaratskhelia, M. (2006): Interactions of HIV-1 Gag with assembly cofactors. In *Biochemistry* 45 (13), pp. 4077–4083. DOI: 10.1021/bi052308e.

Simons, K.; Ikonen, E. (1997): Functional rafts in cell membranes. In *Nature* 387 (6633), pp. 569–572. DOI: 10.1038/42408.

Simons, K.; Warren, G. (1984): Semliki Forest virus: a probe for membrane traffic in the animal cell. In *Advances in protein chemistry* 36, pp. 79–132. DOI: 10.1016/S0065-3233(08)60296-X.

Sjostrand, F. S.; ANDERSSON-CEDERGREN, E.; DEWEY, M. M. (1958): The ultrastructure of the intercalated discs of frog, mouse and guinea pig cardiac muscle. In *Journal of ultrastructure research* 1 (3), pp. 271–287. DOI: 10.1016/s0022-5320(58)80008-8.

Skočaj, M.; Resnik, N.; Grundner, M.; Ota, K.; Rojko, N.; Hodnik, V.; Anderluh, G.; Sobota, A.; Maček, P.; Veranič, P.; Sepčić, K. (2014): Tracking cholesterol/sphingomyelin-rich membrane domains with the ostreolysin A-mCherry protein. In *PloS one* 9 (3), e92783. DOI: 10.1371/journal.pone.0092783.

Smith, P. F. (1971): Biosynthesis of cholesteryl glucoside by Mycoplasma gallinarum. In *Journal of bacteriology* 108 (3), pp. 986–991. DOI: 10.1128/jb.108.3.986-991.1971.

Sokolov, A.; Radhakrishnan, A. (2010): Accessibility of cholesterol in endoplasmic reticulum membranes and activation of SREBP-2 switch abruptly at a common cholesterol threshold. In *The Journal of biological chemistry* 285 (38), pp. 29480–29490. DOI: 10.1074/jbc.M110.148254.

Solanko, L. M.; Honigmann, A.; Midtiby, H. S.; Lund, F. W.; Brewer, J. R.; Dekaris, V.; Bittman, R.; Eggeling, C.; Wüstner, D. (2013): Membrane orientation and lateral diffusion of BODIPY-cholesterol as a function of probe structure. In *Biophysical journal* 105 (9), pp. 2082–2092. DOI: 10.1016/j.bpj.2013.09.031.

Spuul, P.; Balistreri, G.; Kääriäinen, L.; Ahola, T. (2010): Phosphatidylinositol 3-kinase-, actin-, and microtubule-dependent transport of Semliki Forest Virus replication complexes from the plasma membrane to modified lysosomes. In *Journal of virology* 84 (15), pp. 7543–7557. DOI: 10.1128/jvi.00477-10.

Steck, T. L.; Lange, Y. (2018): Transverse distribution of plasma membrane bilayer cholesterol: Picking sides. In *Traffic (Copenhagen, Denmark)* 19 (10), pp. 750–760. DOI: 10.1111/tra.12586.

Stevenson, G. W.; Kiupel, M.; Mittal, S. K.; Kanitz, C. L. (1999): Ultrastructure of porcine circovirus in persistently infected PK-15 cells. In *Veterinary pathology* 36 (5), pp. 368–378. DOI: 10.1354/vp.36-5-368.

Suchanek, M.; Hynynen, R.; Wohlfahrt, G.; Lehto, M.; Johansson, M.; Saarinen, H.; Radzikowska, A.; Thiele, C.; Olkkonen, V. M. (2007): The mammalian oxysterol-binding protein-related proteins (ORPs) bind 25-hydroxycholesterol in an evolutionarily conserved pocket. In *The Biochemical journal* 405 (3), pp. 473–480. DOI: 10.1042/BJ20070176.

Sumner, C.; Kotani, O.; Liu, S.; Musier-Forsyth, K.; Sato, H.; Ono, A. (2022): Molecular Determinants in tRNA D-arm Required for Inhibition of HIV-1 Gag Membrane Binding. In *Journal of molecular biology* 434 (2), p. 167390. DOI: 10.1016/j.jmb.2021.167390.

Sumner, C.; Ono, A. (2024): The "basics" of HIV-1 assembly. In *PLoS Pathogens* 20 (2), e1011937. DOI: 10.1371/journal.ppat.1011937.

Sundquist, W. I.; Kräusslich, H.-G. (2012): HIV-1 assembly, budding, and maturation. In *Cold Spring Harbor perspectives in medicine* 2 (7), a006924. DOI: 10.1101/cshperspect.a006924.

Takeda, M.; Leser, G. P.; Russell, C. J.; Lamb, R. A. (2003): Influenza virus hemagglutinin concentrates in lipid raft microdomains for efficient viral fusion. In *Proceedings of the National Academy of Sciences of the United States of America* 100 (25), pp. 14610–14617. DOI: 10.1073/pnas.2235620100.

Tanaka, K. A.K.; Suzuki, K. G.N.; Shirai, Y. M.; Shibutani, S. T.; Miyahara, M. S.H.; Tsuboi, H.; Yahara, M.; Yoshimura, A.; Mayor, S.; Fujiwara, T. K.; Kusumi, A. (2010): Membrane molecules mobile even after chemical fixation. In *Nature methods* 7 (11), pp. 865–866. DOI: 10.1038/nmeth.f.314.

Tang, C.; Loeliger, E.; Luncsford, P.; Kinde, I.; Beckett, D.; Summers, M. F. (2004): Entropic switch regulates myristate exposure in the HIV-1 matrix protein. In *Proceedings of the National Academy of Sciences of the United States of America* 101 (2), pp. 517–522. DOI: 10.1073/pnas.0305665101.

Tedbury, P. R.; Novikova, M.; Ablan, S. D.; Freed, E. O. (2016): Biochemical evidence of a role for matrix trimerization in HIV-1 envelope glycoprotein incorporation. In *Proceedings of the National Academy of Sciences of the United States of America* 113 (2), E182-90. DOI: 10.1073/pnas.1516618113.

Tedbury, P. R.; Novikova, M.; Alfadhli, A.; Hikichi, Y.; Kagiampakis, I.; KewalRamani, V. N.; Barklis, E.; Freed, E. O. (2019): HIV-1 Matrix Trimerization-Impaired Mutants Are Rescued by Matrix Substitutions That Enhance Envelope Glycoprotein Incorporation. In *Journal of virology* 94 (1). DOI: 10.1128/JVI.01526-19.

Thiele, C.; Hannah, M. J.; Fahrenholz, F.; Huttner, W. B. (2000): Cholesterol binds to synaptophysin and is required for biogenesis of synaptic vesicles. In *Nature cell biology* 2 (1), pp. 42–49. DOI: 10.1038/71366.

Todd, G. C.; Duchon, A.; Inlora, J.; Olson, E. D.; Musier-Forsyth, K.; Ono, A. (2017): Inhibition of HIV-1 Gag-membrane interactions by specific RNAs. In *RNA* 23 (3), pp. 395–405. DOI: 10.1261/rna.058453.116.

Tomishige, N.; Bin Nasim, M.; Murate, M.; Pollet, B.; Didier, P.; Godet, J.; Richert, L.; Sako, Y.; Mély, Y.; Kobayashi, T. (2023): HIV-1 Gag targeting to the plasma membrane reorganizes sphingomyelin-rich and cholesterol-rich lipid domains. In *Nature communications* 14 (1), p. 7353. DOI: 10.1038/s41467-023-42994-w.

Tsai, B.; Gilbert, J. M.; Stehle, T.; Lencer, W.; Benjamin, T. L.; Rapoport, T. A. (2003): Gangliosides are receptors for murine polyoma virus and SV40. In *The EMBO journal* 22 (17), pp. 4346–4355. DOI: 10.1093/emboj/cdg439.

Uckeley, Z. M.; Duboeuf, M.; Gu, Y.; Erny, A.; Mazelier, M.; Lüchtenborg, C.; Winter, S. L.; Schad, P.; Mathieu, C.; Koch, J.; Boulant, S.; Chlanda, P.; Maisse, C. et al. (2024): Glucosylceramide in bunyavirus particles is essential for virus binding to host cells. In *Cellular and molecular life sciences : CMLS* 81 (1), p. 71. DOI: 10.1007/s00018-023-05103-0.

UNAIDS (2024): The urgency of now: AIDS at a crossroads. Geneva: Joint United Nations Programme on HIV/AIDS; 2024. Licence: CC BY-NC-SA 3.0 IGO. UNAIDS. Geneva. Available online at https://www.unaids.org/sites/default/files/media_asset/2024-unaids-global-aids-update-summary_en.pdf.

van Damme, N.; Goff, D.; Katsura, C.; Jorgenson, R. L.; Mitchell, R.; Johnson, M. C.; Stephens, E. B.; Guatelli, J. (2008): The interferon-induced protein BST-2 restricts HIV-1 release and is downregulated from the cell surface by the viral Vpu protein. In *Cell host & microbe* 3 (4), pp. 245–252. DOI: 10.1016/j.chom.2008.03.001.

van Meer, G.; Kroon, A. I.P.M. de (2011): Lipid map of the mammalian cell. In *Journal of cell science* 124 (Pt 1), pp. 5–8. DOI: 10.1242/jcs.071233.

van Meer, G.; Voelker, D. R.; Feigenson, G. W. (2008): Membrane lipids: where they are and how they behave. In *Nature reviews. Molecular cell biology* 9 (2), pp. 112–124. DOI: 10.1038/nrm2330.

van Schalkwyk, C.; Mahy, M.; Johnson, L. F.; Imai-Eaton, J. W. (2024): Updated Data and Methods for the 2023 UNAIDS HIV Estimates. In *Journal of acquired immune deficiency syndromes (1999)* 95 (1S), e1-e4. DOI: 10.1097/QAI.0000000000003344.

Vanier, M. T.; Latour, P. (2015): Laboratory diagnosis of Niemann-Pick disease type C: the filipin staining test. In *Methods in cell biology* 126, pp. 357–375. DOI: 10.1016/bs.mcb.2014.10.028.

Varki, A. (2017): Biological roles of glycans. In *Glycobiology* 27 (1), pp. 3–49. DOI: 10.1093/glycob/cww086.

Vasiliver-Shamis, G.; Tuen, M.; Wu, T. W.; Starr, T.; Cameron, T. O.; Thomson, R.; Kaur, G.; Liu, J.; Visciano, M. L.; Li, H.; Kumar, R.; Ansari, R.; Han, D. P. et al. (2008): Human immunodeficiency virus type 1 envelope gp120 induces a stop signal and virological synapse formation in noninfected CD4+ T cells. In *Journal of virology* 82 (19), pp. 9445–9457. DOI: 10.1128/JVI.00835-08.

Veatch, S. L.; Keller, S. L. (2003): Separation of liquid phases in giant vesicles of ternary mixtures of phospholipids and cholesterol. In *Biophysical journal* 85 (5), pp. 3074–3083. DOI: 10.1016/S0006-3495(03)74726-2.

Veatch, S. L.; Keller, S. L. (2005): Miscibility phase diagrams of giant vesicles containing sphingomyelin. In *Physical review letters* 94 (14), p. 148101. DOI: 10.1103/PhysRevLett.94.148101.

Venkatesh, S.; Bieniasz, P. D. (2013): Mechanism of HIV-1 virion entrapment by tetherin. In *PLoS Pathogens* 9 (7), e1003483. DOI: 10.1371/journal.ppat.1003483.

Verma, D. K.; Gupta, D.; Lal, S. K. (2018): Host Lipid Rafts Play a Major Role in Binding and Endocytosis of Influenza A Virus. In *Viruses* 10 (11). DOI: 10.3390/v10110650.

Visco, I.; Chiantia, S.; Schwille, P. (2014): Asymmetric supported lipid bilayer formation via methyl-β-cyclodextrin mediated lipid exchange: influence of

asymmetry on lipid dynamics and phase behavior. In *Langmuir : the ACS journal of surfaces and colloids* 30 (25), pp. 7475–7484. DOI: 10.1021/la500468r.

Wan, C.; Kiessling, V.; Tamm, L. K. (2008): Coupling of cholesterol-rich lipid phases in asymmetric bilayers. In *Biochemistry* 47 (7), pp. 2190–2198. DOI: 10.1021/bi7021552.

Wang, W.; Yang, L.; Huang, H. W. (2007): Evidence of cholesterol accumulated in high curvature regions: implication to the curvature elastic energy for lipid mixtures. In *Biophysical journal* 92 (8), pp. 2819–2830. DOI: 10.1529/biophysj.106.097923.

Watson, H. (2015): Biological membranes. In *Essays in biochemistry* 59, pp. 43–69. DOI: 10.1042/bse0590043.

Welsch, S.; Miller, S.; Romero-Brey, I.; Merz, A.; Bleck, C. K.E.; Walther, P.; Fuller, S. D.; Antony, C.; Krijnse-Locker, J.; Bartenschlager, R. (2009): Composition and three-dimensional architecture of the dengue virus replication and assembly sites. In *Cell host & microbe* 5 (4), pp. 365–375. DOI: 10.1016/j.chom.2009.03.007.

Whitfield, G. B.; Brock, T. D.; Ammann, A.; Gottlieb, D.; Carter, H. E. (1955): Filipin, an Antifungal Antibiotic: Isolation and Properties. In *J. Am. Chem. Soc.* 77 (18), pp. 4799–4801. DOI: 10.1021/ja01623a032.

Wilhelm, L. P.; Voilquin, L.; Kobayashi, T.; Tomasetto, C.; Alpy, F. (2019): Intracellular and Plasma Membrane Cholesterol Labeling and Quantification Using Filipin and GFP-D4. In *Methods in molecular biology (Clifton, N.J.)* 1949, pp. 137–152. DOI: 10.1007/978-1-4939-9136-5_11.

Wilk, T.; Pfeiffer, T.; Bosch, V. (1992): Retained in vitro infectivity and cytopathogenicity of HIV-1 despite truncation of the C-terminal tail of the env gene product. In *Virology* 189 (1), pp. 167–177. DOI: 10.1016/0042-6822(92)90692-i.

Williams, A.; Menon, S.; Crowe, M.; Agarwal, N.; Biccler, J.; Bbosa, N.; Ssemwanga, D.; Adungo, F.; Moecklinghoff, C.; Macartney, M.; Oriol-Mathieu, V. (2023): Geographic and Population Distributions of Human Immunodeficiency Virus (HIV)-1 and HIV-2 Circulating Subtypes: A Systematic Literature Review and Meta-analysis (2010-2021). In *The Journal of infectious diseases* 228 (11), pp. 1583–1591. DOI: 10.1093/infdis/jiad327.

Wit, G. de; Danial, J. S.H.; Kukura, P.; Wallace, M. I. (2015): Dynamic label-free imaging of lipid nanodomains. In *Proceedings of the National Academy of Sciences of the United States of America* 112 (40), pp. 12299–12303. DOI: 10.1073/pnas.1508483112.

Wood, W. G.; Igbavboa, U.; Müller, W. E.; Eckert, G. P. (2011): Cholesterol asymmetry in synaptic plasma membranes. In *Journal of neurochemistry* 116 (5), pp. 684–689. DOI: 10.1111/j.1471-4159.2010.07017.x.

Woolhouse, M.; Scott, F.; Hudson, Z.; Howey, R.; Chase-Topping, M. (2012): Human viruses: discovery and emergence. In *Philosophical transactions of the Royal Society of London. Series B, Biological sciences* 367 (1604), pp. 2864–2871. DOI: 10.1098/rstb.2011.0354.

Wright, E. R.; Schooler, J. B.; Ding, H. J.; Kieffer, C.; Fillmore, C.; Sundquist, W. I.; Jensen, G. J. (2007): Electron cryotomography of immature HIV-1 virions reveals the structure of the CA and SP1 Gag shells. In *The EMBO journal* 26 (8), pp. 2218–2226. DOI: 10.1038/sj.emboj.7601664.

Wüstner, D.; Solanko, K. (2015): How cholesterol interacts with proteins and lipids during its intracellular transport. In *Biochimica et biophysica acta* 1848 (9), pp. 1908–1926. DOI: 10.1016/j.bbamem.2015.05.010.

Wüstner, D.; Solanko, L.; Sokol, E.; Garvik, O.; Li, Z.; Bittman, R.; Korte, T.; Herrmann, A. (2011): Quantitative assessment of sterol traffic in living cells by dual labeling with dehydroergosterol and BODIPY-cholesterol. In *Chemistry and physics of lipids* 164 (3), pp. 221–235. DOI: 10.1016/j.chemphyslip.2011.01.004.

Wyma, D. J.; Jiang, J.; Shi, J.; Zhou, J.; Lineberger, J. E.; Miller, M. D.; Aiken, C. (2004): Coupling of human immunodeficiency virus type 1 fusion to virion maturation: a novel role of the gp41 cytoplasmic tail. In *Journal of virology* 78 (7), pp. 3429–3435. DOI: 10.1128/jvi.78.7.3429-3435.2004.

Wyma, D. J.; Kotov, A.; Aiken, C. (2000): Evidence for a stable interaction of gp41 with Pr55(Gag) in immature human immunodeficiency virus type 1 particles. In *Journal of virology* 74 (20), pp. 9381–9387. DOI: 10.1128/jvi.74.20.9381-9387.2000.

Yachi, R.; Uchida, Y.; Balakrishna, B. H.; Anderluh, G.; Kobayashi, T.; Taguchi, T.; Arai, H. (2012): Subcellular localization of sphingomyelin revealed by two toxin-based probes in mammalian cells. In *Genes to cells : devoted to molecular & cellular mechanisms* 17 (8), pp. 720–727. DOI: 10.1111/j.1365-2443.2012.01621.x.

Yamaji, A.; Sekizawa, Y.; Emoto, K.; Sakuraba, H.; Inoue, K.; Kobayashi, H.; Umeda, M. (1998): Lysenin, a novel sphingomyelin-specific binding protein. In *The Journal of biological chemistry* 273 (9), pp. 5300–5306. DOI: 10.1074/jbc.273.9.5300.

Yandrapalli, N.; Lubart, Q.; Tanwar, H. S.; Picart, C.; Mak, J.; Muriaux, D.; Favard, C. (2016): Self assembly of HIV-1 Gag protein on lipid membranes generates PI(4,5)P2/Cholesterol nanoclusters. In *Scientific reports* 6, p. 39332. DOI: 10.1038/srep39332.

Yang, G.-S.; Wagenknecht-Wiesner, A.; Yin, B.; Suresh, P.; London, E.; Baird, B. A.; Bag, N. (2023): Lipid-driven interleaflet coupling of plasma membrane order regulates FcεRI signaling in mast cells. In *Biophysical journal*. DOI: 10.1016/j.bpj.2023.07.027.

Yang, P.; Ai, L.-S.; Huang, S.-C.; Li, H.-F.; Chan, W.-E.; Chang, C.-W.; Ko, C.-Y.; Chen, S. S.-L. (2010): The cytoplasmic domain of human immunodeficiency virus type 1 transmembrane protein gp41 harbors lipid raft association determinants. In *Journal of virology* 84 (1), pp. 59–75. DOI: 10.1128/jvi.00899-09.

Yesylevskyy, S. O.; Demchenko, A. P. (2012): How cholesterol is distributed between monolayers in asymmetric lipid membranes. In *European biophysics journal : EBJ* 41 (12), pp. 1043–1054. DOI: 10.1007/s00249-012-0863-z.

Yu, X.; Yuan, X.; Matsuda, Z.; Lee, T. H.; Essex, M. (1992): The matrix protein of human immunodeficiency virus type 1 is required for incorporation of viral envelope protein into mature virions. In *Journal of virology* 66 (8), pp. 4966–4971. DOI: 10.1128/JVI.66.8.4966-4971.1992.

Zacharias, D. A.; Violin, J. D.; Newton, A. C.; Tsien, R. Y. (2002): Partitioning of lipid-modified monomeric GFPs into membrane microdomains of live cells. In *Science (New York, N.Y.)* 296 (5569), pp. 913–916. DOI: 10.1126/science.1068539.

Zhou, W.; Parent, L. J.; Wills, J. W.; Resh, M. D. (1994): Identification of a membrane-binding domain within the amino-terminal region of human immunodeficiency virus type 1 Gag protein which interacts with acidic phospholipids. In *Journal of virology* 68 (4), pp. 2556–2569. DOI: 10.1128/JVI.68.4.2556-2569.1994.

Zhou, W.; Resh, M. D. (1996): Differential membrane binding of the human immunodeficiency virus type 1 matrix protein. In *Journal of virology* 70 (12), pp. 8540–8548. DOI: 10.1128/JVI.70.12.8540-8548.1996.

Zhu, P.; Chertova, E.; Bess, J.; Lifson, J. D.; Arthur, L. O.; Liu, J.; Taylor, K. A.; Roux, K. H. (2003): Electron tomography analysis of envelope glycoprotein trimers on HIV and simian immunodeficiency virus virions. In *Proceedings of the National*

Academy of Sciences of the United States of America 100 (26), pp. 15812–15817. DOI: 10.1073/pnas.2634931100.

Zhu, P.; Liu, J.; Bess, J.; Chertova, E.; Lifson, J. D.; Grisé, H.; Ofek, G. A.; Taylor, K. A.; Roux, K. H. (2006): Distribution and three-dimensional structure of AIDS virus envelope spikes. In *Nature* 441 (7095), pp. 847–852. DOI: 10.1038/nature04817.

Zila, V.; Margiotta, E.; Turoňová, B.; Müller, T. G.; Zimmerli, C. E.; Mattei, S.; Allegretti, M.; Börner, K.; Rada, J.; Müller, B.; Lusic, M.; Kräusslich, H.-G.; Beck, M. (2021): Cone-shaped HIV-1 capsids are transported through intact nuclear pores. In *Cell* 184 (4), 1032-1046.e18. DOI: 10.1016/j.cell.2021.01.025.